



Escola Tècnica Superior d'Enginyeria
de Telecomunicació de Barcelona

UNIVERSITAT POLITÈCNICA DE CATALUNYA

UNIVERSITAT POLITÈCNICA DE CATALUNYA
DEPT. OF SIGNAL THEORY AND COMMUNICATIONS

DEGREE IN TELECOMMUNICATIONS ENGINEERING
FINAL THESIS

Efficient SAR MTI simulator of marine scenes

Author:
Francisco Ceba Vega

Supervisor:
Antoni Broquetas Ibars
Rapporteur:
Eduardo Makhoul Varona

June 2014

*“Boundaries are actually the main factor
in space, just as the present, another
boundary, is the main factor in time.”*

Eduardo Chillida

Abstract

Multichannel spaceborne and airborne *synthetic aperture radars* (SAR) offer the opportunity to monitor maritime traffic through specially designed instruments and applying a suitable signal processing in order to reject sea surface clutter. These processing techniques are known as *Moving Target Indication* techniques (MTI) and the choice of the most adequate method depends on the radar system and operating environment. In maritime scenes the seas presents a complicated clutter whose temporal/spatial coherence models and background reflectivity depends on a large number of factors and are still subject of research. Moreover the targets kinematics are influenced by the sea conditions, producing in some situations high alterations in the imaged target. These aspects make difficult the detectability analysis of vessels in maritime scenarios, requiring both theoretical models and numerical simulations.

This thesis looks into the few available MTI techniques and deals experimentally with them in a developed simulator for maritime SAR images. The results are also presented in a image format, giving the sequence for one trial simulation and the asymptotic probability of detection for the simulated conditions.

Acknowledgements

In first place, I would like to express my deepest gratitude to Prof. Antoni Broquetas, who introduced me in the world of radar and remote sensing and gave to me the opportunity to be part of a European Project. I am also grateful for his advices, advisory, dedication and patience during these months.

Secondly, I would like to thank Eduardo Makhoul for his previous works and answers, which helped me to solve my doubts and to develop the code needed for the simulator. But especially for his support developing the required off-line database. Without his help we wouldn't have achieved all the objectives.

I would like to thanks Josep Ruiz for helping us to calculate the diamond diagrams, PRFs and ambiguities for the used instruments throughout this project.

I would like to express my gratitude to my partners Tània Palacín and Xavi Bertomeu for their labour with the sea reflectivity model and the database reading functions.

I would like to express my sincere thanks to my officemate Yu Zhan, who helped me to modify part of the modules of the simulator, to incorporate new functionalities and with the validation and writing of reports.

This work has been carried out in the framework of the SIMTISYS European project supported by EC under FP7-SPACE-2010-1 Contract 263268. The intensive and fruitful cooperation among industrial and academic partners has been crucial in the successful completion and validation of the simulator developed modules. For this reason I also wish to thank the other members of SIMTISYS consortium for their help and support: Marco Maffei, Roberto Venturini, Fulvia Verzegnassi (Thales Alenia Space Italy), Sergio Barbarossa, Paolo DiLorenzo, Paolo Vecchiarelli (Univ. degli Studi di Roma "La Sapienza"), Federico Letterio, Stefania Tonetti (DEIMOS Space), Alasdhair Beaton, Richard Lowe (Telespazio VEGA), Patrizio Nini (Sistematica), and Marco Bonamente (D'Appolonia). Thank you all.

Contents

Abstract	v
Acknowledgements	vi
Contents	vii
1 Introduction	1
2 SAR principles and signal model	3
2.1 Introduction	3
2.2 SAR imaging coordinate system	4
2.2.1 SAR geometry	4
2.2.2 Equivalent flat Earth model	5
2.3 Image resolutions	6
2.3.1 Slant range resolution	7
2.3.2 Azimuth resolution	8
2.4 Ambiguities	9
2.4.1 Time domain ambiguities	9
2.4.2 Doppler domain ambiguities	11
2.5 SAR processor	11
2.6 Radar power equation	13
2.7 Effect of moving targets on SAR images	14
2.7.1 Shifting	14
2.7.2 Defocussing	18
3 Radar analysis of marine scene	23
3.1 Introduction	23
3.2 Sea clutter reflectivity	25
3.3 Statistic model for sea clutter	27
3.4 Correlation of sea clutter	29
3.4.1 Temporal correlation	29
3.4.2 Sea spectra	30
4 MTI techniques and detectors	35
4.1 Introduction	35
4.2 Mission Analysis	35
4.3 MTI Techniques	38

4.3.1	Displaced Phase Center Antenna Technique (DPCA)	38
4.3.2	Along-Track Interferometry (ATI)	39
4.3.3	Space-Time Adaptive Processing (STAP)	42
4.3.3.1	Post-Doppler STAP	44
4.3.3.2	Imaging STAP	44
4.3.3.3	Spatial STAP	45
4.4	CFAR Detectors	45
4.4.1	OS-CFAR	45
4.4.2	2D-CFAR	48
4.5	Off-line evaluation of the probability of detection	53
4.5.1	Scaling the target radial velocity	56
4.5.2	Scaling the clutter correlation time	57
4.5.3	Scaling the range resolution	57
4.6	Case study	58
4.6.1	DRA instrument	60
4.6.2	TANDEM instrument	62
4.6.3	BOOM instrument	65
5	Simulator structure	67
5.1	Introduction	67
5.2	Block diagram and files format	67
5.3	SBR & MTI Stand-Alone applications	69
5.3.1	Requirements	69
5.3.1.1	IDL Virtual Machine	69
5.3.1.2	Folder Structure	70
5.3.2	SBR Module GUI	70
5.3.3	MTI Module GUI	72
6	Conclusions and future work	75
A	Pulse compression signal approach	77
B	RDA processing steps	81
C	TSC Sea Clutter Model	85
D	NRL Sea Clutter Model	87
E	Off-line MTI Database Dimensions	89
	References	91

Chapter 1

Introduction

Oceans covers the 71% of the Earth's surface. The vast maritime area and the difficulties of achieving an effective surveillance result in the scene of many illegal activities. The smuggling, border infractions, piracy, fishery control and environmental hazards are just a few examples of a problem that has begun to arouse the interest of many national and European institutions. The *Automatic Identification System* (AIS) is a ship tracking system for identifying and locating vessels. Its use is mandatory in the whole port areas and crowded marine traffic zones. However, when there is a large quantity of money at stake, the offenders contract skilled people to disable it. In this context *Low Earth Orbit* satellites provide the opportunity to monitor large maritime areas with a prompt response. This thesis has been elaborated under the European Seventh Framework Program, developing part of the SAR maritime simulator *SIMTISYS* (SIMulator of Moving Target Indication SYStem). The project attempts to increase the knowledge in the SAR-MTI paradigm, addressed to detect targets in maritime areas. The tracking, classification, identification and kinematics parameters estimation works are carried out at posteriori of this stage and are not considered hereinafter. SIMTISYS has been the extension of NEWA project (New European WAtcher) which was aimed to analyse the European Space-based reconnaissance and surveillance capabilities and solutions for MTI systems.

The work of this thesis is focussed on the design, development and validation of a SAR imaging simulator from scattering centres distribution over marine scenes and a MTI processing module for multichannel radars, where the main techniques adopted have been *Displaced-Phase Center Antenna* technique (DPCA), the *Along-Track Interferometry* (ATI) and the *Space-Time Adaptive Processing* (STAP).

Chapter 2 briefly describes the SAR principles and presents the effects of moving targets in SAR images. Chapter 3 deals with the sea properties and presents a method to generate SAR images of the sea in an efficient manner. In Chapter 4 different MTI instruments have been proposed and analysed, in combination of MTI techniques and CFAR detectors. A representative case study has been included in order to show the potential of the developed simulator in assessing the future SAR missions including MTI capabilities. The simulator structure is described in Chapter 5 and finally the conclusions and future work are reviewed in Chapter 6.

Chapter 2

SAR principles and signal model

2.1 Introduction

This chapter presents the operational fundamentals of SAR (*Synthetic Aperture Radar*) needed to understand the SAR image generation process in SIMTISYS simulator. There is a large variety of recommended literature addressing the SAR principles and processing subject in depth ([1–3]) and not experienced readers in SAR are encouraged to consult it when required. However, the basic principles are summarized along the following paragraphs.

A SAR is an active coherent all-pass system operating at microwaves spectrum. The name of *Synthetic Aperture* comes from the fact that multiple pulses obtained during the illumination¹ time for a certain point are processed in order to achieve the resolution equivalent to an antenna with larger dimensions. The main advantages of SAR are that they can operate with a high spatial resolution, independently of atmospheric conditions or solar illumination, have a wide amplitude dynamic range and the phase of the coherent images can be exploited for topographic mapping and change detection. The radar waves can penetrate vegetation, snow and even soil in a certain favourable conditions. These characteristics make SAR instruments suitable for a large variety of applications as land environment (topographic mapping, cartography, subsidence, navigation, ...), hydrology (ice and snow monitoring, wetlands, flooding, ...), monitoring renewable resource (land use mapping, forestry, agriculture, ...), oceanography (ocean dynamics, bathymetry, ocean currents, coastal zone mapping, ...), geology (earthquakes, tectonics, volcanoes, landslides, ...), glaciology (ice flow monitoring) and traffic control (terrestrial and maritime traffic monitoring).

¹The term illumination was coined because early investigations of electromagnetic fields comprises the visible spectrum.

2.2 SAR imaging coordinate system

In *Real Aperture Radar* (RAR) applications, like scatterometry and altimetry where the antenna is always pointed to the nadir, the azimuth resolution is proportional to the distance. However SAR operates in a side-looking manner in order to reduce range and Doppler ambiguities. There are three main SAR imaging modes depending on the resolution to be achieved. The *stripmap* maintains fixed the antenna pointing direction and moves the antenna footprint taking advantage of the platform track. The *scansar* mode illuminates several subswaths in a single track by scanning different antenna elevation angles. The *spotlight* keeps the antenna footprint fixed in a certain area for a longer time, increasing the length of the synthetic aperture and the along-track resolution. Hereinafter only the most common *stripmap* mode is going to be considered, which is the mode implemented in the simulator.

2.2.1 SAR geometry

Figure 2.1 exhibits the simple geometric model for a monostatic radar on board of a spacecraft. The platform moves along the orbital path with a speed V_s while transmitting pulses at a certain rate, determined by the *Pulse Repetition Frequency* (PRF). The antenna collects the electromagnetic echoes from the antenna footprint, which is the projection of the antenna 3-dB main beam over the Earth surface. The reference coordinates system is defined by the x -axis, parallel to the sensor path vector and called also *along-track* or *azimuth* dimension, and the z -axis, perpendicular to the sensor path vector and also called *across-track* or *slant range*. The antenna has been considered with no squint angle (i.e. with the antenna pointing vector perpendicular to the sensor path) which is the zero Doppler plane. However the planet surface moves relative to the orbit plane depending on the observed latitude and for this reason SAR on-board satellites points the antenna broadside with a small squint angle in order to cancel out the Doppler introduce by the Earth rotation. It is commonly known as *yaw steering* method [3]. The orbit height, represented by H_0 , is typically between 500-800 Km (LEO orbit) [Cosmo Skymed, TerraSAR-X, Radarsat 1-2]. The slant range distance between the antenna and the center of the footprint is denoted by R_0 . The angle formed by the vector pointing to nadir and the slant range vector is the observation angle (θ_{obs}) or also called off-nadir angle or looking angle. Its value determines the subswath being imaged.

The projection of z coordinate over the Earth surface is called ground range, and is calculated dividing the slant range distance by the $\sin(\theta_{inc})$.

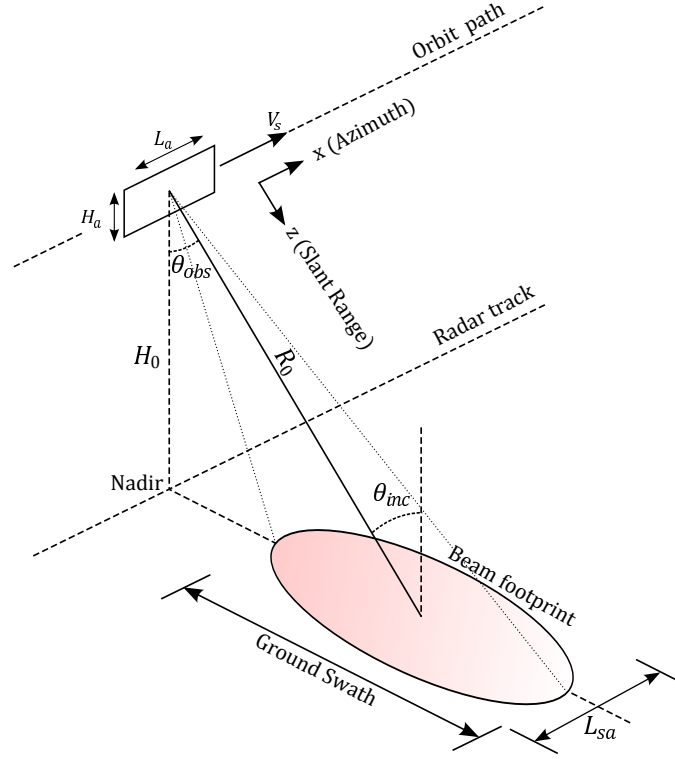


FIGURE 2.1: SAR acquisition geometry operating in Stripmap mode.

2.2.2 Equivalent flat Earth model

Notice that $\sin(\theta_{inc})$ and $\sin(\theta_{obs})$ has not the same value for a real Earth model, where the surface has a radius of curvature² of 6.371 Km. Moreover the spacecraft velocity (V_s) is not equal to the footprint velocity (V_g), being the last always lower (see Figure 2.2). It is possible to work with an equivalent rectilinear model where satellite and footprint moves with the same velocity, calculated by [3]:

$$V_{eff} = \sqrt{V_s V_g}. \quad (2.1)$$

This term is called *effective radar velocity* and does not represent a physical velocity at all. The approximation is accurate enough for geometric analysis but it is not adequate to be used in a production SAR processor [3]. To calculate the Doppler bandwidth V_s is used and when ground distances are concerned V_g is used.

²Mean Earth radius value.

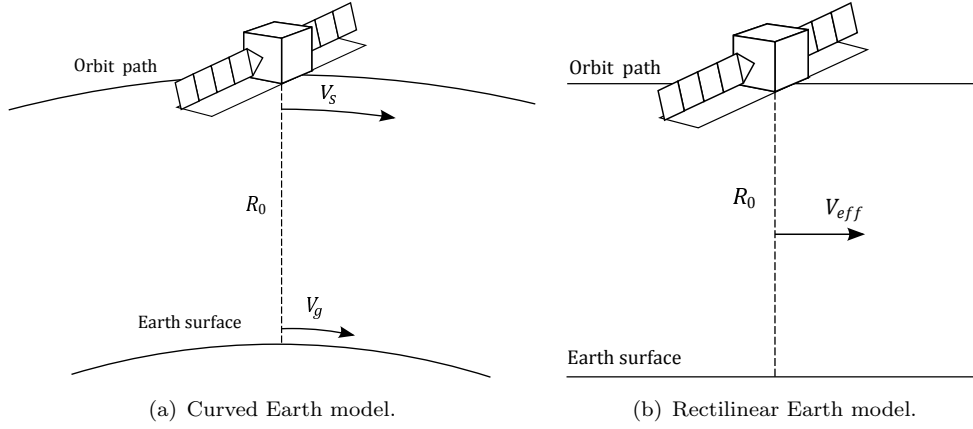


FIGURE 2.2: Approximation from spherical to flat Earth model.

2.3 Image resolutions

The spatial resolution is defined as the minimum distance between two points allowing be distinguished in the image. Without processing the received echoes (*Raw Data*) the system resolution is characterized by the antenna pattern. For a uniformly illuminated rectangular aperture with dimensions $L_a \times H_a$, the radiated field in plane H is ([4])

$$|E_\phi| = \frac{E_0 L_a H_a}{2\lambda r} (1 + \cos \theta) \left| \frac{\sin \left(k \frac{L_a}{2} \sin \theta \right)}{k \frac{L_a}{2} \sin \theta} \right|, \quad |E_\theta| = 0, \quad (2.2)$$

where k represents the wavenumber ($2\pi/\lambda$), θ is the azimuthal angle and ϕ is the elevation angle. A quick representation of Equation 2.2 shows that along the main beam the function can be simplified by a sinc-like function, whose main beam 3-dB width can be roughly calculated by:

$$\begin{aligned} \theta_{3dB} &\approx \frac{\lambda}{L_a} \\ \phi_{3dB} &\approx \frac{\lambda}{H_a}. \end{aligned} \quad (2.3)$$

For small scenarios with a ground range distance in the order of kilometres the elevation angle pattern can be considered uniform.

Putting some numbers in the above expression results in huge antenna lengths in order to get resolutions in the order of tens of meters. In the following subsection is explained the synthetic aperture concepts to obtain higher angular resolution from smaller antennas.

2.3.1 Slant range resolution

In a classical radar system transmitting rectangular unmodulated pulses, the slant range resolution in meters is obtained by:

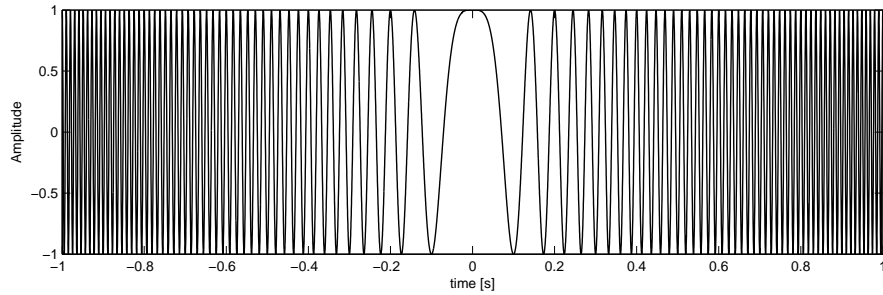
$$\delta_{SR} = \frac{cT}{2} = \frac{c}{2BW}, \quad (2.4)$$

where T is the pulse width in seconds and c is the speed of light in the vacuum. The resolution is inversely proportional to the pulse length, but short pulses constrains the peak power by physical limitations. The solution lies on transmit larger modulated pulses, increasing the time-bandwidth product, and later compress it. This technique is known as *pulse compression* or *matched filtering*.

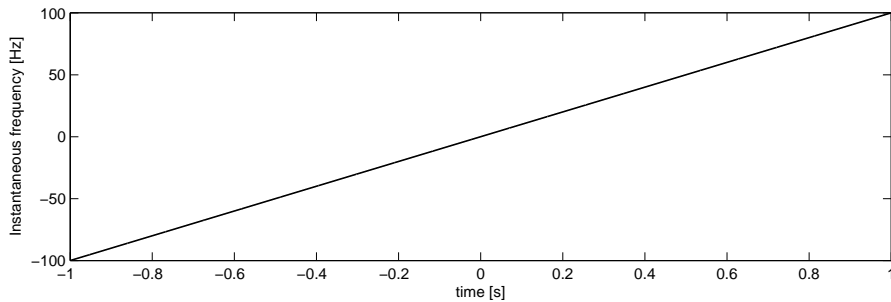
One of the most used compression radar signals is the *chirp* pulse, expressed in baseband as:

$$s_t(t) = \Pi\left(\frac{t}{T}\right) \exp^{j\pi k_r t^2}, \quad (2.5)$$

which is a linear FM modulation. The time domain representation is shown in Figure 2.3(a), whose instantaneous frequency is a linear function of time, characterized by $k_r = BW/T$ (Figure 2.3(b)).



(a) Real part representation of Equation 2.5.



(b) Instantaneous frequency as a function of time. The line inclination sets the chirp slope.

FIGURE 2.3: Chirp signal.

The matched filter is a time-reversed conjugated replica of the transmitted signal $s_t(t)$, i.e:

$$h(t) = s^*(-t). \quad (2.6)$$

The received signal is then convolved with the matched filter

$$s_{out}(t) = s_r(t) \otimes h(t) = \int_{-\infty}^{+\infty} s_r(u) h(t-u) du. \quad (2.7)$$

Correlation and convolution should not be confused. Computational burden of Equation 2.7 can be reduced performing the convolution as a product in frequency domain and making the DFTs of vectors with a power-of-two number of samples to reduce the number of operations.

Finally, the derivation of the matched filter output in time domain results in a sinc-like function (Appendix A)

$$s_{out} \approx \frac{T}{2} \text{sinc}(k_r T(t - t_0)), \quad (2.8)$$

with a 3-dB width of

$$\delta_{SR} = \frac{0.886c}{2|k_r|T} \approx \frac{c}{2BW} \quad (2.9)$$

meters in slant range.

2.3.2 Azimuth resolution

The projected antenna footprint in azimuth or also called *synthetic aperture length* is $L_{sa} = \theta_{3dB} R_o = (\lambda/L_a) R_o$. As the radar advances the antenna collects echoes from the point P during a time $T_{obs} = L_{sa}/V_{eff}$ (Figure 2.4). During this time the echoes from P covers the spectrum region from $f_0 \pm f_D$, where f_0 is the carrier frequency and

$$f_D = \frac{-2V_{eff}}{\lambda} \sin(\theta_{3dB}/2) = V_{eff}\theta_{3dB}/\lambda = V_{eff}/L_a, \quad (2.10)$$

being thus the Doppler bandwidth $B_D = 2f_D$. The PRF must be then equal or higher than the Doppler bandwidth. Usually an oversampling of 10-20% is desirable. If a neighbour point Q is displaced from P the Doppler history of Q will be a time shifted replica of P . Then, the shortest time shift that can be measured is

$$t_{\delta a} = 1/B_D = 1/(2f_D) = L_a/(2V_{eff}). \quad (2.11)$$

Equation 2.10 let us to derive the final achievable azimuthal resolution:

$$\delta_{az} = t_{\delta a} V_{eff} = L_a/2. \quad (2.12)$$

This expressions results contrary as one might think at the beginning. The smaller the antenna the higher the resolution in azimuth. It can be explained if we take into account from Equation 2.3 that the shorter the antenna length, the wider the beamwidth and also the Doppler bandwidth. On the other hand there is a trade-off because decreasing the antenna length impacts on the *Signal to Noise Ratio*, as will be seen in Section 2.6.

2.4 Ambiguities

While visual human system imaging coordinates is composed by angle-angle format, *RAR* is a angle-time delay format and *SAR* is a Doppler-time delay format. If for some reason two different points in SAR image meets in the same Doppler-time bin they cannot be resolved, which means that cannot be separated. This phenomenon is known as *ambiguity*. In this section the sources of ambiguities in both SAR image domains are analysed.

2.4.1 Time domain ambiguities

Successive pulses should be away enough from each other so that, in any instant of time, no more than one pulse coincides over the swath surface, as shown in Figure 2.5.

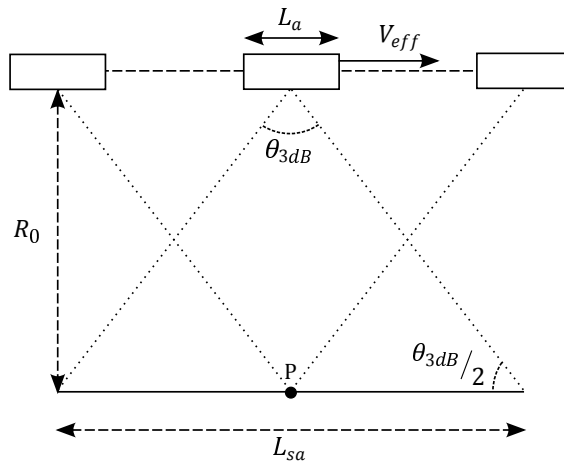


FIGURE 2.4: Geometry of a synthetic aperture for the azimuth-slant range plane. The point P is visible from the locations inside the synthetic aperture, which is equal to the real antenna footprint.

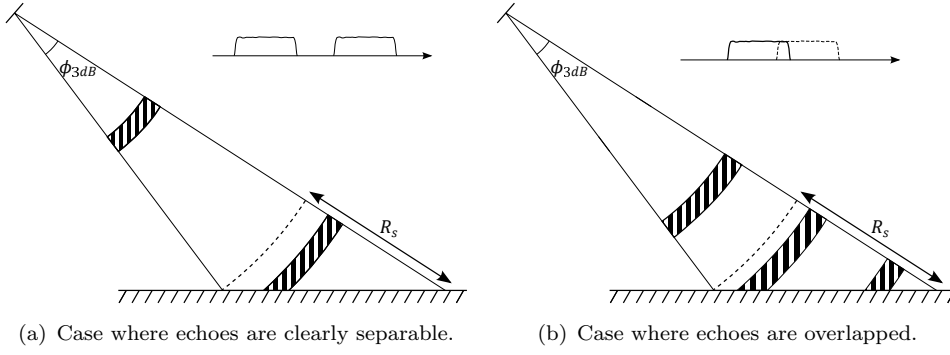


FIGURE 2.5: Zero Doppler plane geometry illustrating the cases with and without range ambiguities.

This restriction imposes a maximum limit for the PRF, which impacts directly on the antenna area. Another limitation for the PRF is that several echoes are in the propagation path at the same time. Therefore the receiver must not transmit while receiving echoes. This produces a set of inadmissible intervals for PRFs, distinguishable in the *Diamond Diagram* representation.

Looking beyond the main lobe of the antenna pattern, the reader can realize that the energy coming from the side lobes can be received at the same time as the energy of the main lobe. This is another source of ambiguity depicted in Figure 2.6, and its magnitude depends on the antenna pattern, the illumination geometry and the surface reflectivity. Specially problematic is the echo coming through the nadir, which is the strongest echo. To avoid it the PRF is selected such that the nadir echo does not overlap in time with the main beam echo or, if possible, put a null in the antenna pattern on the nadir angle.

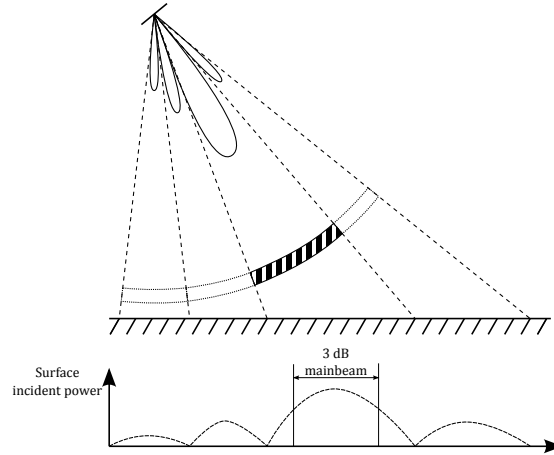


FIGURE 2.6: Antenna radiation pattern projected over the ground surface.

2.4.2 Doppler domain ambiguities

In the azimuthal plane there is also sidelobes that can produce ambiguities. As seen in section 2.3.2, the Doppler bandwidth is sampled with a finite PRF frequency. The spectrum is then repeated every PRF interval (Figure 2.7). The azimuthal sidelobes introduces then an overlapping whose strength depends again on the antenna pattern. The effect can be appreciated when, in the main beam, there is a surface with low reflectivity while high power echoes are received through a sidelobe. An example of this situation is when a coastal city is being imaged with calm sea conditions. In this case a replica of the city image can appear over the sea surface [5].

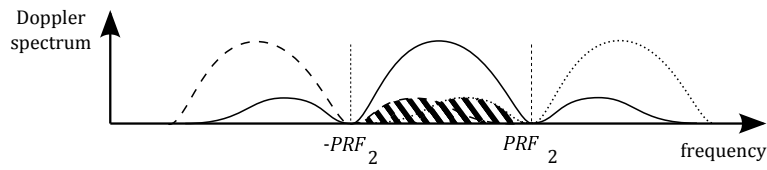


FIGURE 2.7: Doppler spectra sampled. The azimuthal sidelobes add an overlapping to the desired spectral band.

2.5 SAR processor

The signal captured by the radar without processing is referred as *raw data*. Once demodulated to baseband, the signal for one single target can be expressed as [3]:

$$S_{rd}(\tau, \eta) = A_0 w_r \left(\tau - \frac{2R(\eta)}{c} \right) w_a(\eta - \eta_c) e^{-j4\pi f_0 \frac{R(\eta)}{c}} e^{j\pi k_r \left(\tau - \frac{2R(\eta)}{c} \right)^2}, \quad (2.13)$$

where A_0 is a complex constant modelling the target scattering, τ is the range time, η is the azimuth time, η_c is the offset between the zero Doppler time and the beam center instant, w_r is the range window (rectangular), w_a is the azimuth window (sinc-squared function) and $R(\eta)$ is the range equation for a static target, given by:

$$R(\eta) = \sqrt{R_0^2 + V_{eff}^2 \eta^2} \approx R_0 + \frac{V_{eff}^2 \eta^2}{2R_0}. \quad (2.14)$$

The right-hand Equation in 2.14 has been approximated by a parabolic function using Taylor series expansion to separate the *range cell migration* term.

The objective of the SAR processor is to focus the raw data so that the SAR image can be easily interpreted. There are several available algorithms (Backprojection, Chirp Scaling, $\omega - k$ algorithm), but one of the most used for its simplicity is the *Range*

Doppler Algorithm (RDA). Its efficiency relies on using spectral domain operations in both dimensions, applying two one-domain compressions operations separately. The functional implementation is shown in Figure 2.8.

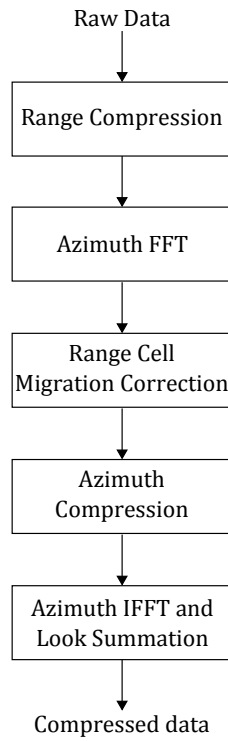
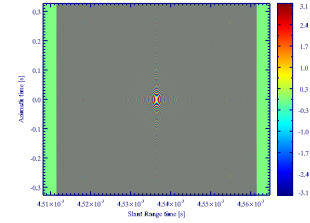
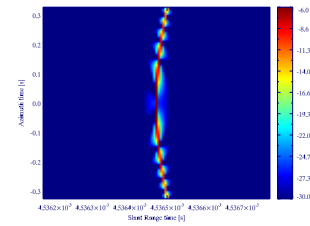


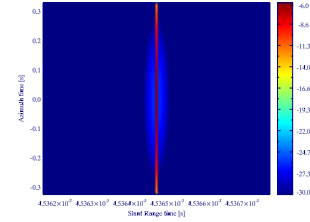
FIGURE 2.8: Block diagram implementation for the basic RDA for relatively small squinted angles.



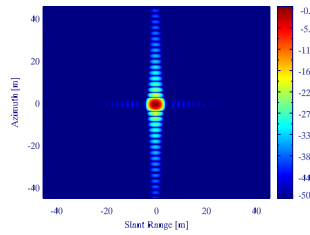
(a) Angle of captured raw data.



(b) Amplitude of range compressed signal.



(c) Amplitude of range-cell migration corrected signal.



(d) Point-spread function after azimuth compression.

FIGURE 2.9: SAR image steps along the RDA processing.

Once processed the expression 2.13, the output signal of RDA can be written as [3]:

$$S_{ac}(\tau, \eta) = A_0 \rho_r \left(\tau - \frac{2R_0}{c} \right) \rho_a(\eta) e^{-j\frac{4\pi f_0 R_0}{c}} e^{j2\pi f_{\eta} \tau}, \quad (2.15)$$

where ρ_r and ρ_a represents the range and azimuth compressed pulse envelope respectively. The development of expression 2.15 can be found in Appendix B.

2.6 Radar power equation

The *signal-to-noise ratio* (SNR) is one of the most important parameters that determines the quality of an image. Let us consider a simple radar transmitting a pulse with power P_t and using an antenna with a gain $G = 4\pi A_{eff}/\lambda^2$. The incident power density per unit area over a target at a distance r is:

$$P_i = \frac{P_t G}{4\pi r^2}. \quad (2.16)$$

The backscattered power is equal to

$$P_s = P_i \sigma = \frac{P_t G \sigma}{4\pi r^2}, \quad (2.17)$$

where σ is the radar cross section (RCS) of the target (expressed in square meters), obtained by $\sigma = \sigma^0 S_{illum}$, being S_{illum} the target illuminated area and σ^0 the surface density of RCS. The σ^0 depends on the material electrical properties, roughness, polarization, frequency and angle and is mainly used for surface distributed targets. The reflected power density per unit area at the antenna is:

$$P_r = \frac{A_{eff}}{4\pi r^2} P_s = \frac{P_t G^2 \lambda^2 \sigma}{(4\pi)^3 r^4}. \quad (2.18)$$

The thermal noise power in the receiver is given by $P_N = k_B T B$, where k_B is the Boltzmann constant, T is the system noise temperature (including both receiver thermal temperature and the illuminated surface temperature) and B is the system bandwidth. Taking into account the system and atmospheric signal losses in L , the SNR after data processing is expressed as [2]:

$$SNR_{SAR} = \frac{P_t G^2 \lambda^2 \sigma}{(4\pi)^3 r^4 k_B T B L} \rho = \frac{P_t G^2 \lambda^2 \sigma^0}{(4\pi)^3 r^4 k_B T B L} (r \Delta \theta_H) \frac{c_0 \tau_0}{2 \sin(\theta_{inc})} \left(\frac{PRF}{B_{dopp}} \right), \quad (2.19)$$

where ρ represents the SNR improvement factor after azimuth and range pulse compression.

One way to characterize the noise performance of the receiver with a single parameter is to determine its *noise equivalent sigma zero* (NESZ) [6]. The NESZ depends on several factors (e.g: antenna pattern, power transmitted, quantization, ...) and is obtained equating the SNR to 0 dB. Therefore it can be expressed as:

$$NESZ = \frac{(4\pi)^3 r^4 k_B T B L}{P_t G^2 \lambda^2 \rho}, \quad (2.20)$$

but in SAR is usually to express this parameter in slant range instead of ground range, which is called *noise equivalent beta naught* (NEBN). The relationship between both parameters is $NEBN = NESZ / \sin(\theta_{inc})$.

2.7 Effect of moving targets on SAR images

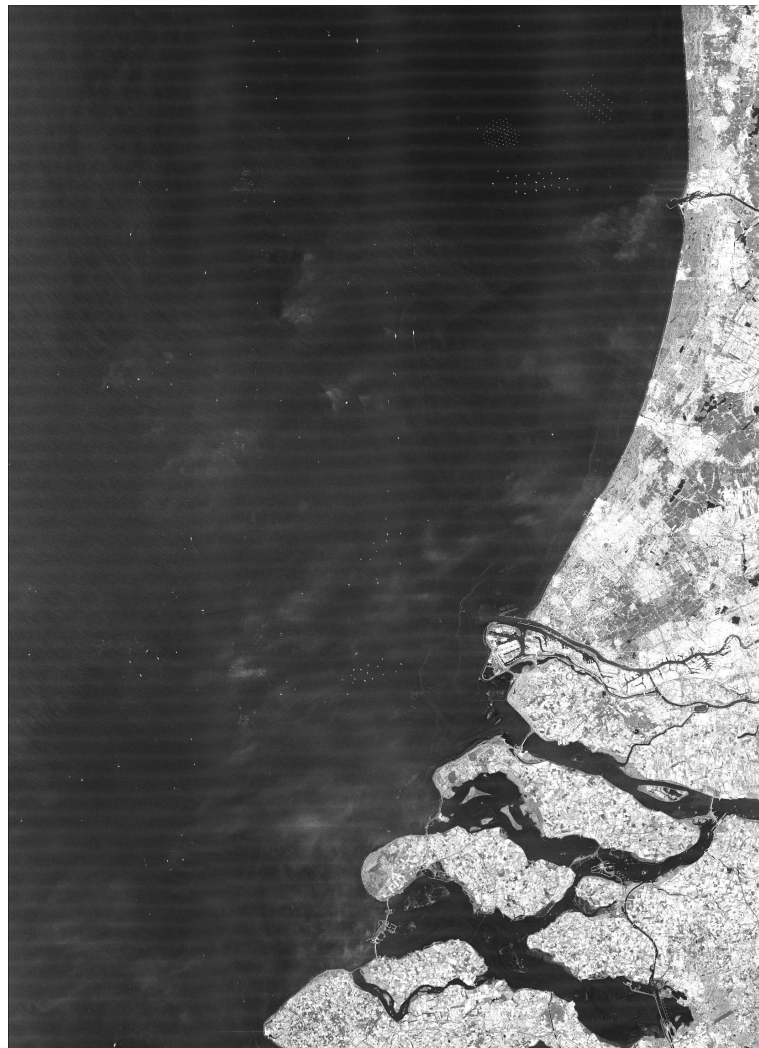
A SAR processor, as seen in section 2.5, takes advantage from the a priori knowledge of the target position at each instant to compress the image in azimuth. When the target moves during the one half second of illumination time the range equation becomes unknown, producing a shifting in the SAR image and/or the defocussing of the target along several azimuth cells.

The same phenomenon occurs when, in the case of airborne radars, the platform suffers displacements and attitude errors. In this case the objective is to correct the position errors with *motion compensation* techniques (MOCO), like *Prominent Point Processing*, *Reflecivity Displacement Method* or *Phase Gradient Autofocus* [7, 8]. However our interest is to characterize the impact of moving targets besides to correct their effects.

2.7.1 Shifting

Imaging radars uses large bandwidths in range, which do not allows to perceive the Doppler shift in across-track. Nevertheless the phase-induced error is noticeable when comparing the sequence of pulses in along-track dimension. When considering a target with only radial velocity (parallel to z axis) a phase perturbation occurs which produces a shift in target position, as it can be seen in Figure 2.10(b).

The target is relocated to the point of zero Doppler, i.e. the time of closest approach, when the raw data is processed to form the image. The most common analysis to predict the shift position of the target consist in equate the range equation to zero and solve



(a) The image shows several offshore ships with different kinematics. On the top-right of the image is possible to identify some bright points arranged that belongs to the Zuid-Holland wind farm.



(b) Zoom in over the image 2.10(a). The scene shows a vessel imaged in a wrong azimuth position regarding to its wake pattern caused by the radial speed.

FIGURE 2.10: TerraSAR-X image of Rotterdam coast acquired in April of 2008.

then the equation isolating the time variable (using McLaurin series [9] or Cardano's method). But there is a simplest way: finding the cross between the velocity vector and the line perpendicular to the velocity vector that passes through the antenna phase center, as sketched in Figure 2.11.

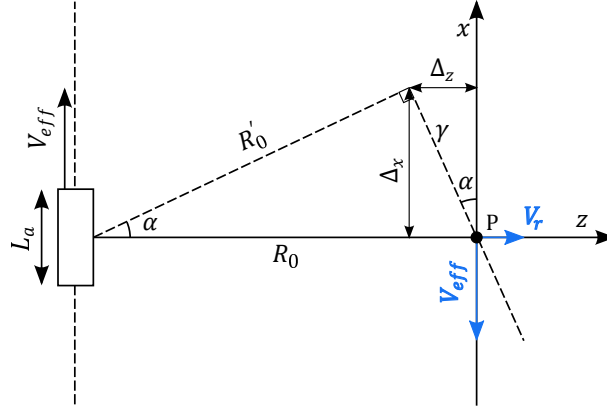


FIGURE 2.11: Slant range geometry for moving targets considering only radial velocity.

Easily we can find the angle α and the modulus γ of the vector that sets the shift w.r.t. the real position of the target:

$$\begin{aligned}\alpha &= \arctan \frac{\Delta_z}{\Delta_x} = \arctan \frac{V_r}{V_{eff}} \approx \frac{V_r}{V_{eff}} \\ \gamma &= R_0 \sin \alpha,\end{aligned}\tag{2.21}$$

and the shifts in along-track and across-track coordinates in meters results as:

$$\begin{aligned}\Delta_x &= -\gamma \cos \alpha = -R_0 \sin \alpha \cos \alpha \approx -R_0 \frac{V_r}{V_{eff}} \\ \Delta_z &= \gamma \sin \alpha = R_0 \sin^2 \alpha = R_0 \left(\frac{V_r}{V_{eff}} \right)^2.\end{aligned}\tag{2.22}$$

Both expressions in 2.22 are the same except for the negative sign and the square, which makes the across-track shift negligible for small velocity values. It is important to remark that for the flat Earth assumption the effective velocity V_{eff} has been used, which is not a physical parameter. For real SAR images where the orbits experiences a curved trajectory the satellite velocity V_s must be used in Equation 2.22 [10]. Otherwise the expected shift will be lower than the measured offset in the image.

Besides of the annoying high along-track shifting, the other problem is a loss of amplitude

caused by the decreasing overlap time between the target signal and the azimuthal matched filter when the zero Doppler point moves away from the pulse center, as shown in Figure 2.12. The azimuth shift in time is obtained dividing the shift in meters by the spacecraft effective velocity:

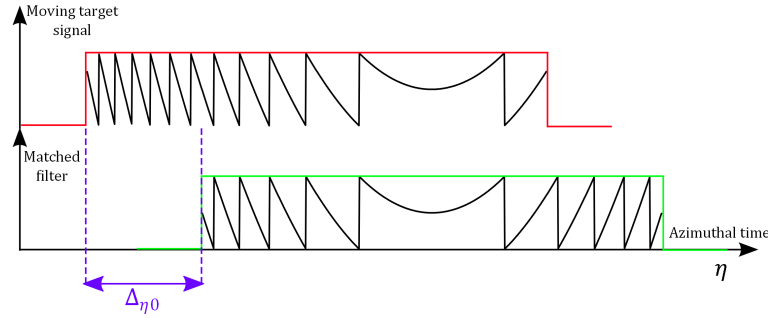


FIGURE 2.12: Azimuth representation of the received echo aligned with the matched filter Doppler centroid. Note that the overlapping time is reduced $\Delta\eta_0$.

$$\Delta\eta_0 = \frac{\Delta x}{V_{eff}} = -R_0 \frac{V_r}{V_{eff}^2}. \quad (2.23)$$

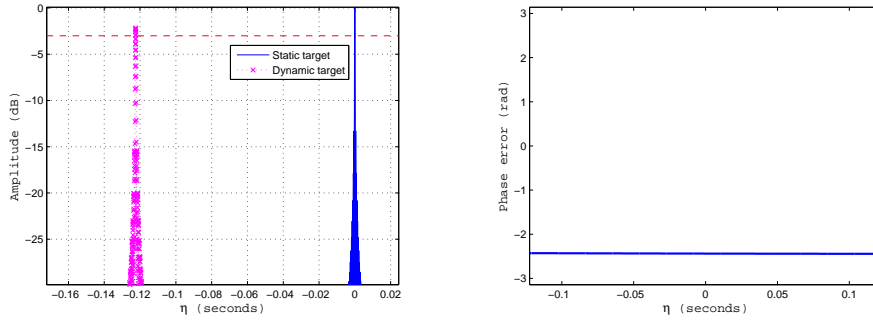
The loss in amplitude can be calculated as the ratio between the overlapping when the azimuthal pulse and the matched filter are both centred at zero Doppler and the total pulse length. Writing it mathematically, the -3dB threshold gives:

$$A (T_{obs} - \Delta\eta_{3dB}) = A \left(\frac{T_{obs}}{\sqrt{2}} \right), \quad (2.24)$$

with A representing an arbitrary amplitude. Rearranging terms and substituting $\Delta\eta_{3dB}$ by the expression 2.23 :

$$V_{sr3dB} = \frac{-T_{obs}V_{eff}^2}{R_0} \left(1 - \frac{1}{\sqrt{2}} \right). \quad (2.25)$$

Substituting Equation 2.25 by typical satellite values gives a required velocity in the order of 40 Km/h for experience a power loss of 3dB. Figure 2.13 shows the azimuth amplitude profile for a moving target compared with the static target case and the phase error between the azimuth received signal and the matched filter. Figure 2.13(a) shows the loss in the moving target signal whilst Figure 2.13(b) depicts a constant phase error that entail a correct chirp slope for the azimuth filter.



(a) Azimuthal amplitude profile for a moving and static target. (b) Phase error between the received signal and the azimuth matched filter. For an accurate comparison the azimuth shift has been corrected.

FIGURE 2.13: Simulated results for a target moving with slant range velocity of 10 m/s, a satellite effective velocity of 7 Km/s and a slant range distance of 600 Km.

2.7.2 Defocussing

The other drawback of moving targets comes when higher order terms in range equation impacts on the azimuthal frequency rate. The mismatch produces a smearing of target signal over several azimuth cells, proportional to the amplitude loss. For an accurate analysis we can rewrite the range equation, for a moving target in the slant range-azimuth plane, with the explicit Taylor approximation:

$$\begin{aligned}
 R(\eta, v_{sr}, v_{az}, a_{sr}, a_{az}) &= \sqrt{\left(R_0 + v_{sr}\eta + \frac{a_{sr}}{2}\eta^2\right)^2 + \left((V_{eff} - v_{az})\eta + \frac{a_{sr}}{2}\eta^2\right)^2} \\
 &\approx R_0 + v_{sr}\eta + \frac{1}{2} \left[\frac{(V_{eff} - v_{az})^2}{R_0} + a_{sr} \right] \eta^2,
 \end{aligned} \tag{2.26}$$

where v and a represents the target velocity and acceleration and the subscripts sr and az denotes the slant range and azimuth domain respectively. A uniformly accelerated motion has been assumed. Expanding Equation B.1, the range compressed received signal in temporal domain for moving targets can be roughly expressed as

$$\begin{aligned}
 S_{rc}(\tau, \eta) &= A_0 \rho_r \left(\tau - \frac{2R(\eta)}{c} \right) w_a(\eta - \eta_c) e^{-j\frac{4\pi f_0 R_0}{c}} \\
 &\quad e^{-j\frac{4\pi f_0 V_{sr}}{c}\eta} e^{-j\frac{2\pi f_0}{c} \left(\frac{(V_{eff} - v_{az})^2}{R_0} + a_{sr} \right) \eta^2}.
 \end{aligned} \tag{2.27}$$

The second exponential term highlights the azimuth shifting in Doppler domain, which endorses the approach accomplished in section 2.7.1. The equivalence can be demonstrated using the relationships $\Delta_\eta = \Delta_x/V_{eff}$ and $\Delta f_\eta = K_a \cdot \Delta_\eta$, jointly with expression 2.22. Even though the azimuth bandwidth is not changed, the Doppler shift may cause a backfolding of the spectrum due to the use of a finite PRF. In such a case the PRF needs to be increased considering the expected radial speeds margin as follows:

$$PRF \geq BW_{Dop} + 2\Delta f_\eta = \frac{2V_{eff}}{L_a} + \frac{4f_0 v_{sr}}{c}. \quad (2.28)$$

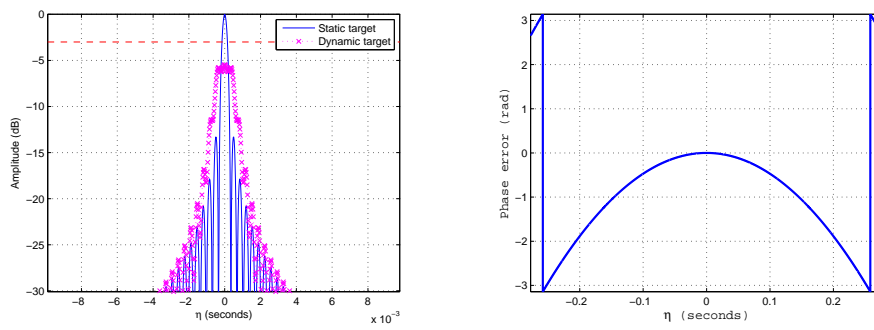
The last exponential in 2.27 is weighted by the term η^2 , which means a variation in the chirp slope value. Specifically the chirp slope for dynamic targets is

$$k'_a = \frac{2}{\lambda} \left(\frac{(V_{eff} - v_{az})^2}{R_0} + a_{sr} \right), \quad (2.29)$$

which can be decomposed into two terms: $k'_a = k_a + k_\epsilon$. The first is the nominal frequency rate and the second is the error rate, expressed as:

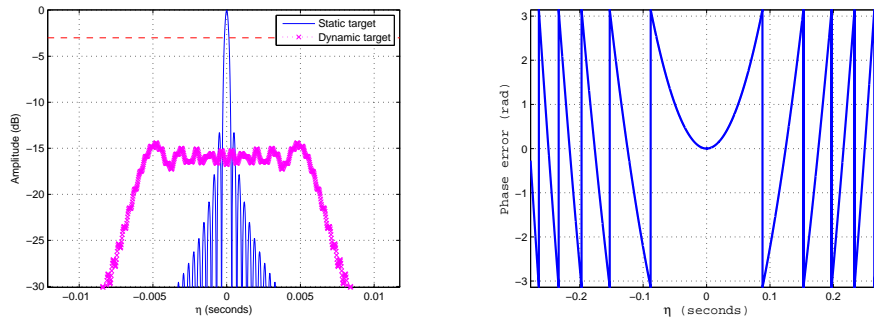
$$k_\epsilon = \frac{2}{\lambda} \left(\frac{v_{az}^2 - 2V_{eff}v_{az}}{R_0} + a_{sr} \right). \quad (2.30)$$

From the above expression we can observe that frequency rate error is caused by the along-track velocity and the across-track acceleration. The along-track accelerations can be neglected as shown in Figure 2.16, where a simulation trial has been performed owing to the difficulty of deriving an analytical expression. However in an airborne case the cubic terms need to be considered, which creates sidelobe asymmetries [11]. Moreover in [12] is developed the same analysis but considering the target moving on ground coordinates. In this case appears in the frequency error rate equation a term depending on the across-track velocity, which is caused by the relative change of the incidence angle during the illumination time. This effect varies the radial velocity for each azimuthal time instant when projected on slant range plane (can be considered an acceleration). But its contribution can be neglected and is only appreciated for very fast targets moving perpendicular to the platform direction during high illumination times.



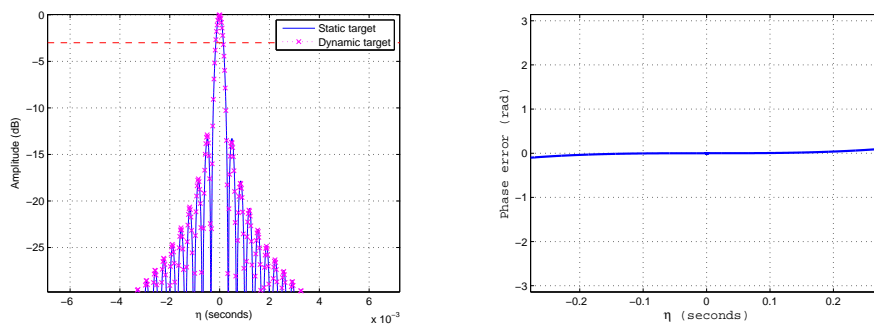
(a) Azimuthal amplitude profile of a moving and (b) Phase error between the received signal and static target.

FIGURE 2.14: Simulated results for a target moving with azimuth velocity of 10 m/s, a satellite effective velocity of 7 Km/s and a slant range distance of 600 Km.



(a) Azimuthal amplitude profile of a moving and (b) Phase error between the received signal and static target.

FIGURE 2.15: Simulated results for a target moving with slant range acceleration of 2 m/s/s, a satellite effective velocity of 7 Km/s and a slant range distance of 600 Km.



(a) Azimuthal amplitude profile of a moving and (b) Phase error between the received signal and static target.

FIGURE 2.16: Simulated results for a target moving with azimuth acceleration of 2 m/s/s, a satellite effective velocity of 7 Km/s and a slant range distance of 600 Km.

The point of interest lies on foresee the impact of moving targets in amplitude losses and the signal broadening factor. To predict the target amplitude losses we can hypothesize that the maximum output signal will occur when the matched filter and the azimuth signal pulse are coincident, i.e: both pulses are perfectly overlapped.

Going further with the matched filter output expression (2.7), the following equation needs to be studied:

$$|U_{az}(\eta_0)| = \left| \int_{-T_{obs}/2}^{T_{obs}/2} e^{j\pi k'_a \eta^2} e^{-j\pi k_a \eta^2} d\eta \right| = \left| \int_{-T_{obs}/2}^{T_{obs}/2} e^{j\pi k_\epsilon \eta^2} d\eta \right|. \quad (2.31)$$

But even using the Fresnel integrals the previous equation is difficult to resolve. Instead of solving the integral it has been decided to find experimentally the phase error ϕ_ϵ at the edges of the signal that produces a certain loss/broadening, thus the measurement is independent of the frequency error rate and the observation time. Relative measures, as done in [13], are not meaningful when the orbital conditions changes. Figure 2.17 shows the losses in decibels and the broadening (measured at -6dB from the maximum) as a function of the edge phase error. Note that the frequency error rate can be obtained as $k_\epsilon = -4\phi_\epsilon/(\pi T_{obs}^2)$.

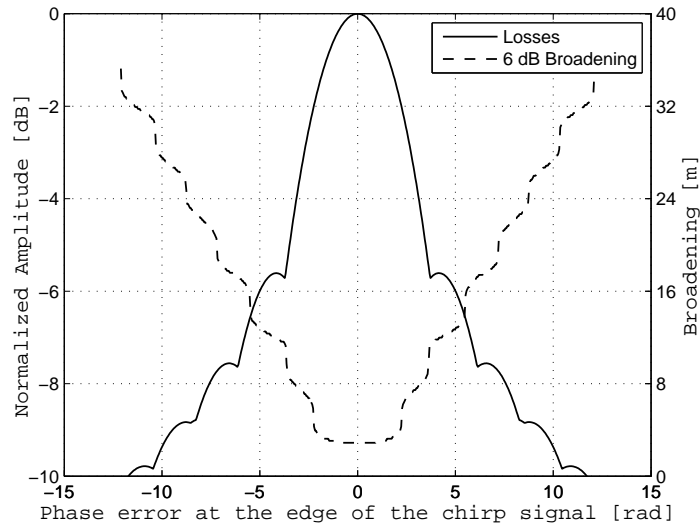


FIGURE 2.17: Losses in amplitude (solid line) and azimuthal broadening (dashed line) as a function of phase error at the edge of chirp signal for an observation window of 0.56 s.

The values of interest are $\phi_{\epsilon-3dB} = 2.72$ rad and $\phi_{\epsilon-6dB} = 5$ rad, where losses of 3 dB and 6 dB are obtained respectively. Looking carefully at Figure 2.17 it is possible to observe that the amplitude do not decay linearly with the phase error and local

minimums can be found, which means that the filter fits better in other points than the center. This fact rejects the hypothesis raised before, where we considered that the maximum always occurred when both signals were perfectly overlapped, and Figure 2.15(a) supports it. The point where the sidelobes reaches the same amplitude as the central peak is $\phi_{\epsilon_{ripple}} = 3.71$ rad. For edge phase errors greater than $\phi_{\epsilon_{ripple}}$ it is not possible to ensure that the maximum will be located at the pulse center.

Chapter 3

Radar analysis of marine scene

3.1 Introduction

In this section the methods and models used in the SIMTISYS simulator to carry out the generation of realistic sea radar images are discussed. The sea backscattering is the most important source of *clutter* in maritime scenes, and is one of the two main undesired data components captured by the radar that limits the technical capability of moving targets detection techniques.

Seasat was the first remote sensing satellite carrying on board a synthetic aperture radar and the main goal was to image ocean waves and sea ice [14]. Before its launch in 1978 there was a discussion between scientific community about the capability of SAR to imaging ocean waves owing to the fact that water waves are moving and the SAR transfer function for sea spectrum can not be considered linear. The following satellites ERS-1 and Envisat helped to improve the knowledge about oceans and to validate/enhance the proposed models. However ocean wave spectrum depends on a large set of parameters (Figure 3.1) and physical interpretation of data imagery is not simple. Despite of oceans and seas have been observed by radars during decades (and will continue being observed) there is still a lack of information and models to help us to understand sea dynamics. Moreover the sea floor plays a important role in sea waves as can be seen in Figure 3.2, where gravity waves period changes as they approach the coast. However our analysis will not mimics these coastal phenomenons.

An electromagnetic simulator of the sea based on dividing the ocean surface in small facets (as discussed in [15, 16]) has been discarded for the high impact in the computational burden of SIMTISYS. Instead, it has been decided to simulate the clutter layer at image domain using low complexity empirical models. Finally some discussion points that should be reviewed in future works are presented.

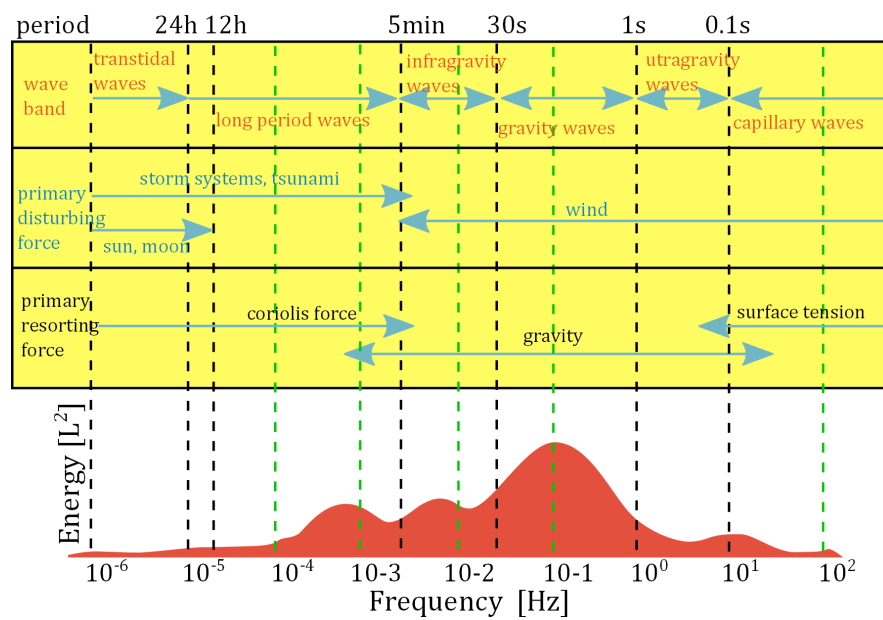


FIGURE 3.1: Qualitative ocean surface wave energy distribution, classification bands and physical phenomena that governs the dynamics [17].

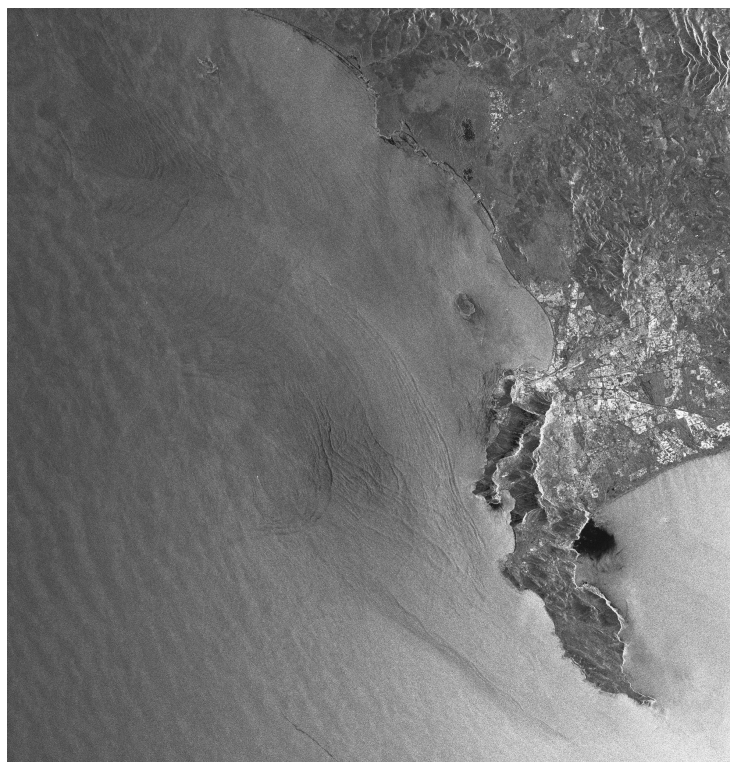


FIGURE 3.2: Radar image of Cape Town acquired by Envisat's Advanced Synthetic Aperture Radar (ASAR). The image shows internal waves transit from deep waters to shallow waters.

3.2 Sea clutter reflectivity

The interaction between electromagnetic waves and the sea surface is an important aspect to predict the mean sea clutter reflectivity in terms of normalized radar cross section σ_0 . The scattering mechanisms can be divided in two groups [18]: The Bragg scattering mechanisms, which are dependent of the polarization, and the non-Bragg scattering mechanisms, modelled by the specular reflection and the scattering from breaking waves,

$$\sigma_0^p = \sigma_{br}^p + \sigma_{sp} + \sigma_{bw}. \quad (3.1)$$

However there are semi-empirical models with many simplification assumptions which provides the mean clutter reflectivity for a limited number of situations and depends on a few physical parameters:

- SIT: Model approach created by H. Sittrop [19] to calculate the ocean reflectivity and its spectral width at X- and Ku-bands. It assumes that the sea clutter is entirely caused by wind generated capillary waves and it only depends on the wind speed and grazing angle.
- GIT: Developed by the Georgia Institute of Technology [20], it combines empirical factors with mathematical models. The sea backscattering is modelled as a function of the grazing angle, the wind speed and/or average wave height, wind angle of direction, the radar wavelength and the polarization. It divides the reflectivity in three main factors: an interference (multipath) factor, a wind speed factor and a wind direction factor. It can be used for a wide frequency range (1-100 GHz) and provide a full wind direction dependence.
- TSC: This model was developed by the Technology Service Corporation [21], founded by Peter Swerling in 1966. The model is based to fit the data collected by Nathanson [22] and it fits well for crosswind situations. The TSC model is similar to GIT model in functional form and it depends on the grazing angle, Douglas sea state, wind direction, radar wavelength and polarization. The detailed description of the TSC model can be found in Appendix C.
- HYB: This model mixes the work done by D.K. Barton, the data collected by Nathanson and the features of the GIT model [23]. It is function of the radar wavelength, the grazing angle, wind direction, Douglas sea state and polarization. It computes the mean clutter reflectivity using the sea state 5 as a reference.
- NRL: Model developed by the Naval Research Laboratory [24] because any empirical (or semi-empirical) sea reflectivity model is in close agreement with the

available data. For this reason the NRL has developed a new parametrized expression with the Nathanson tables as a point of reference. This model is described in Appendix D and it depends on the grazing angle, radar wavelength, the sea state and the polarization. However the wind direction is not taken into account in this model. To solve this problem it has been decided to include a modified version of the wind direction aspect factor of the TSC model, weighting the mean reflectivity provided by the NRL model. The modified aspect factor is then:

$$G'_u = G_u [1 - 0.6 \sin^2 \phi] . \quad (3.2)$$

where ϕ is the wind direction angle relative to the radar look direction and G_u is the aspect factor of the TSC model (Equation C.3). An improved TSC wind aspect factor term has been included [68]. Finally the modified NRL equation results in:

$$\sigma'_{H,V}(dB) = \sigma_{H,V}(dB) + G'_u, \quad (3.3)$$

where the wind direction is now a input factor in the model.

Parameter	SIT	GIT	TSC	HYB
Frequency (GHz)	9.3, 17	1-100	0.5-35	0.5-35
Environment:				
Average wave height (m)	No	0 to 4	Douglas sea state	Douglas sea state
Wind (knots)	< 40	3-30	(0-5)	(0-5)
Geometry:				
Grazing angle (degrees):	0.2-10	0.1-10	0.1-90	0.1-30
Look angle (degrees):	0,90	0-180	0-180	0-180
Polarisation:	HH,VV	HH,VV	HH,VV	HH,VV
Input model parameters:				
Radar wavelength:	Yes	Yes	Yes	Yes
Polarisation:	Yes	Yes	Yes	Yes
Sea state:	No	No	Yes	Yes
Wind speed:	Yes	Yes	No	No
Average wave height:	No	Yes	No	No
Grazing angle:	Yes	Yes	Yes	Yes
Wind aspect angle:	Yes	Yes	Yes	Yes

TABLE 3.1: Comparison of different reflectivity models capabilities (extracted from reference [25]).

Looking at Table 3.1 we can say that the only model valid for SAR is the TSC due to its valid range of frequency and grazing angles. The drawback was that the reflectivity provided by TSC model was so low even for high sea states. This unexpected result dismissed the TSC model from the candidates. Instead, the NRL model has been used for the SIMTISYS simulator, which has as starting point the same Nathanson's experimental data, as the TSC model. All models follow the same behaviour when the input

parameters are varied. A comparison between models and real acquired data can be found in [26]. In conclusion we can state that all the reflectivity models must exhibit the following characteristics:

- Sea clutter reflectivity increases with the frequency and wind speed. But there exist a relationship between them, i.e: depending on the frequency band the increasing ratio of the reflectivity with the wind speed will be higher or lower.
- The grazing angle is one of the most sensitive parameters of the sea clutter reflectivity. The backscattering σ_0 increases with the grazing angle. We can distinguish three regions depending on the value of the grazing angle (see Equation 3.1). For high grazing angles (near 90°) the main backscattering mechanism is the specular reflection, governed by gravitational waves. Between 25° and 75° (typical range of SAR observation angles) there is the Bragg region. For low grazing angles region the reflectivity is affected by multipath, breaking waves and other mechanisms like sea surface conduction features.
- The wind direction plays also an important role in the sea reflectivity. The maximum reflectivity is obtained for upwind conditions (wind direction opposite to the radar look direction). For downwind conditions (wind direction equal to radar look direction) intermediated values are obtained whereas for crosswinds (wind direction parallel to radar look direction) the sea reflectivity reaches the minimum values.
- The reflectivity for VV polarizations is usually higher than HH polarizations, specially for low sea states. For high sea states and low grazing angles the σ_0^{HH} can be higher than σ_0^{VV} . After a search of sea backscattering models it has been found that there is a lack of semi-empirical models for cross-polarizations. Therefore cross-polars situations have not been taken into account.

3.3 Statistic model for sea clutter

The *probability density function* (PDF) of the clutter characterizes the probability of detection of targets and the number of false alarms. Traditionally the Rayleigh distribution (Gaussian in real and imaginary parts) has been used to model the sea reflectivity. This PDF fits well the clutter received in low resolution SAR systems due to the central limit theorem. But as the radar is able to distinguish the sea structure at lower wavelengths the PDF follows another distribution with longer tails, which means higher probability for higher values (commonly known as *spiky*). Other popular distributions

have been used to model the sea clutter amplitude distribution (Weibull, Log-Normal, ...) but the K-distribution has been often proposed to model sea clutter [27].

The reason is because it is based on a physical model that discerns two components with different contributions in amplitude and correlation [25, 27, 28]. The slow varying component can be associated with gravity waves and has a correlation time in the order of seconds. It has also an important spatial correlation, coupled with the temporal, which gives the *periodic* effect on SAR images. The fast varying component, caused by capillary waves, has a correlation time in the order of milliseconds and do not have a spatial structure (is the speckle component).

The overall sea amplitude return for the physically argued model can be formulated as:

$$a = yu, \quad (3.4)$$

where y is the long correlation time component, modelled with the Chi-distribution:

$$f(y) = \frac{2d^{2\nu}y^{2\nu-1}}{\Gamma(\nu)} \exp(-d^2y^2), \quad (3.5)$$

being $\Gamma(\nu)$ the Gamma function, ν the shape parameter and d the scale parameter so that $d^2 = 1/E(y^2)$. The speckle component has a Rayleigh distribution, whose mean value is determined by the Gamma component:

$$f(a|y) = \frac{a\pi}{2y^2} \exp\left(-\frac{a^2\pi}{4y^2}\right). \quad (3.6)$$

The total signal amplitude follows the K-distribution, expressed as:

$$f_K(a) = \int_0^\infty f(a|y)f(y)dy = \frac{2c}{\Gamma(\nu)} \left(\frac{ca}{2}\right)^\nu K_{\nu-1}(ca), \quad (3.7)$$

where $K_{\nu-1}(x)$ is the modified Bessel function of second kind and order ν and $c = \sqrt{\pi}d$ is the scale factor.

The compound model with K-distribution PDF allows to model the spatial and temporal correlations independently. The main problem is to correlate the Gamma process. To avoid it there exist the so-called *memoryless non-linear transform* method (MNLT) [27], which consist in use a pre-correlated Gaussian process with zero mean and unit variance to generate the Gamma process. Before using this method it is important to check that incomplete inverse gamma function is available in our mathematical library. To verify that the generated numbers follows the desired distribution a non-parametric statistic test, like the *Kolmogorov-Smirnov* test (K-S test). The K-S test compares the distances

between the theoretical and sampled cumulative distribution functions to determine if they have the same PDF.

As can be seen in Equation 3.7, the K-distribution only depends on two parameters that can be estimated via Maximum Likelihood estimator [28, 29] or using the moment-based method [30]. The shape parameter ν is the most difficult to predict because it depends on the polarization, grazing angle, azimuth angle, sea conditions and radar parameters. In [31] are presented the results obtained with the DSTO airplane Ingara, flying in a circular orbit around a static point, analysing the shape parameter for a range of grazing angles, azimuth angles and sea conditions using the estimator encountered in [27]. They observed a sinusoidal-like variation of the shape parameter aligned with the wind direction rather than the swell direction. However there is no simple model to predict the shape parameter. In [28] is given a valid range for the shape parameter from 0.1 to 20, being the last one tantamount to the Rayleigh distribution. For these reasons it has been decided to give a Gaussian distribution in real and imaginary parts for the sea backscattering signal.

3.4 Correlation of sea clutter

3.4.1 Temporal correlation

The temporal correlation component takes into account the correlation factor between channels i -th and k -th with a baseline $d_{i,k}$ and the RMS component of the radial velocity of the sea surface. We consider a Gaussian shape correlation function [32] such that the correlation coefficient $\rho_{i,k}$ is:

$$\rho_{i,k} = \exp \left\{ - \left(\frac{\tau_{i,k}}{\tau_c} \right)^2 \right\}, \quad (3.8)$$

where $\tau_{i,k}$ is the delay time between channels i and k , and τ_c is the clutter coherence time, which has the expression [33]:

$$\tau_c = 3 \frac{\lambda}{v_w} \text{erf}^{-1/2} \left(2.7 \frac{\delta_x}{v_w} \right), \quad (3.9)$$

being v_w the wind velocity and δ_x the spatial resolution. Equation 3.9 has been obtained using a real aperture radar with a constant spatial resolution. In SAR, as seen in Chapter 2, the resolution is deteriorated by sea kinematics, causing an increment of δ_x . For this reason the spatial resolution factor δ_x is obtained by means of iteration in Equation 3.9 using as starting point a resolution factor equal to the swath width. In

general no more than five iterations are needed.

Once obtained the temporal correlation matrix $\underline{\underline{R}}$ with $N \times N$ elements, where N is the number of channels, the following step is to correlate the generated random numbers. There are several methods to do it (filtering, eigendecomposition, ...), but the chosen method has been the Cholesky transform [34] for its simplicity and computation efficiency. The method consist in decomposing the covariance matrix into the product of two upper (or lower) triangular matrices $\underline{\underline{U}}$ (or $\underline{\underline{L}}$). Therefore

$$\underline{\underline{R}} = \begin{pmatrix} \sigma_{c1}^2 & \cdots & \rho_{c1,N} \sqrt{\sigma_{c1}^2 \sigma_{cN}^2} \\ \vdots & \ddots & \vdots \\ \rho_{cN,1} \sqrt{\sigma_{cN}^2 \sigma_{c1}^2} & \cdots & \sigma_{cN}^2 \end{pmatrix} = \underline{\underline{U}}^T \underline{\underline{U}} = \underline{\underline{L}} \underline{\underline{L}}^T, \quad (3.10)$$

where the superscript T denotes matrix transposition and the interferometric phase has been neglected. Finally the uncorrelated random numbers $\underline{\underline{\Sigma}}$ are transformed into correlated random numbers $\underline{\underline{\Sigma}}_c$ by means of:

$$\underline{\underline{\Sigma}}_c = \underline{\underline{\Sigma}} \underline{\underline{U}} = \underline{\underline{L}} \underline{\underline{\Sigma}}. \quad (3.11)$$

3.4.2 Sea spectra

The information of ocean waves spectral distribution has been a requirement for ships structural design engineer, forecast navigation hazards, prediction of coastal processes, dissipation of marine pollution, planning the location of tidal power plants, and more applications. During years it has been done by means of moored buoys measuring the vertical and horizontal displacement during a time, with the limitations that it was only a measure of a single point with no directional information. Remote sensing has provided the opportunity to measure sea spectra from SAR images with enough resolution. Sea spectra are the manifestation of the spatial correlation of oceans, and therefore are discussed hereinafter.

In 1964 Willard J. Pierson and Lionel Moskowitz [35] presented an empirical relationship that defines the wave energy distribution in frequency domain. The spectral model was developed from measures done on British weather ships in the North Atlantic sea. It assumes fully developed seas, i.e: wind has been blowing steadily during a long time for a wide area (fetch) until the waves reach the equilibrium with the wind. They found the following expression for the sea spectral shape:

$$S_{PM}(\omega) = \frac{\alpha g^2}{\omega^5} \exp \left[-\beta \left(\frac{\omega_0}{\omega} \right) \right], \quad (3.12)$$

where $\omega = 2\pi f$ is the wave frequency, $\alpha = 8.1 \cdot 10^{-3}$ is the so-called Philip constant, $g = 9.8 \text{ m/s}^2$ is the standard gravity, $\beta = 0.74$, $\omega_0 = g/U_{19.5}$ and $U_{19.5}$ is the wind speed at height of 19.5 meters above the sea surface (height where the anemometers were located). But the wind speed at that height has approximately the same value at 10 meters height ($U_{19.5} \approx 1.026 \times U_{10}$ assuming a drag coefficient of $1.3 \cdot 10^{-3}$). For other heights the following equation can be used:

$$U_Z = U_W \left(\frac{Z}{W} \right)^{\frac{1}{7}}, \quad (3.13)$$

The peak of the spectrum can be found solving $dS(\omega)/d\omega = 0$, obtaining $\omega_p = 0.877g/U_{19.5}$. As can be seen in Figure 3.3, increasing the wind speed results in shift the peak position to lower frequencies.

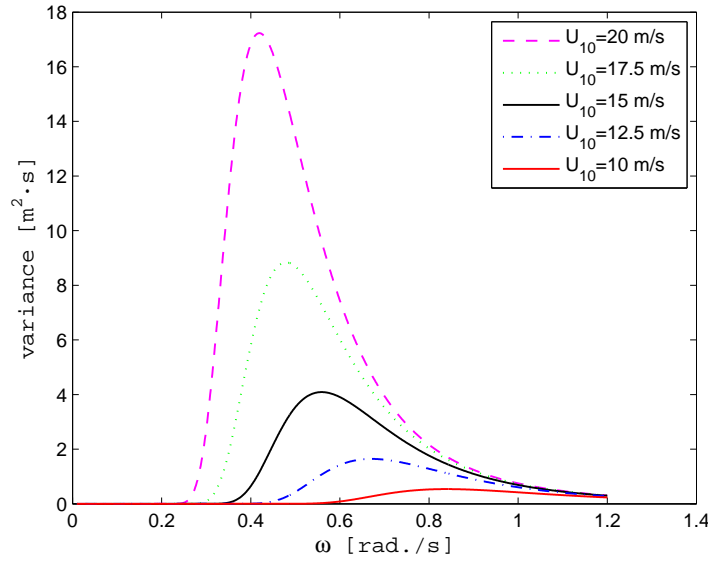


FIGURE 3.3: Wave spectra according to Pierson-Moskowitz model for different wind speeds.

Other parametric spectrum models can be found in oceanographic literature (Elfouhaily [36], Neumann, Bretschneider, ISSC, Sverdrup and Munk [37],...), including the double peaked spectrum for swell coming from a distant storm [38]. The basis of Pierson-Moskowitz are simple and widely accepted. The proof is that it is used in other spectrum model: the JONSWAP spectrum (JOint North Sea WAVE Project) [39], a fetch-limited version of Pierson-Moskowitz spectrum. For this reason it is considered as the starting point for future works and analysis.

Wave spectra $S(\omega)$ are the representation of wave energy distribution in the swell propagation direction. To use them in a 2D image it is necessary to implement the *directional*

wave spectrum taking into account the directional information:

$$E(\omega, \theta) = S(\omega) D(\omega, \theta), \quad (3.14)$$

where θ is the observed direction and $D(\omega, \theta)$ is the directional spreading function such that:

$$\int_{-\pi}^{+\pi} E(\omega, \theta) d\theta = S(\omega). \quad (3.15)$$

Directional distribution models have been proposed by Longuet-Higgins et al. [40], Mitsuyasu et al. [41], Hasselmann et al. [42], Holthuijsen [43], and Donelan et al. [44]. Mitsuyasu et al. developed a parametric equation for directional distribution which depends on the frequency. For the directional spreading function they proposed the following expression:

$$D(\omega, \theta) = N(\psi(\omega)) \cdot \cos\left(\frac{\theta_\omega - \theta}{2}\right)^{2\psi(\omega)}, \quad (3.16)$$

where θ_ω is the main direction of the spectrum (usually the direction of the wind), $N(x)$ is the normalization function and $\psi(\omega)$ is the sharpness control factor, such that:

$$\begin{aligned} N(\psi(\omega)) &= \frac{1}{2\sqrt{\pi}} \frac{\Gamma(\psi(\omega) + 1)}{\Gamma(\psi(\omega) + 1/2)} \\ \psi(\omega) &= 11.5 \left(\frac{g}{\omega_p U_{10}} \right)^{2.5} \left(\frac{\omega}{\omega_p} \right)^\mu \\ \mu &= \begin{cases} 5, & \text{if } \omega \leq \omega_p \\ -2.5, & \text{if } \omega > \omega_p. \end{cases} \end{aligned} \quad (3.17)$$

Hasselmann et al. and Holthuijsen et al. supported the Mitsuyasu model. Specifically the Hasselmann distribution, reported from the analysis of data recorded during the JONSWAP experiment, is also based on the $\cos^{2\psi(\omega)}$ form but with the following parametrization of $\psi(\omega)$:

$$\psi(\omega) = \begin{cases} 6.97 \left(\frac{\omega}{\omega_p} \right)^{4.06}, & \text{if } \omega < 1.05 \cdot \omega_p \\ 9.77 \left(\frac{\omega}{\omega_p} \right)^\mu, & \text{if } \omega \geq 1.05 \cdot \omega_p. \end{cases} \quad (3.18)$$

In this model $\mu = -2.33 - 1.45(U_{10}/C_p - 1.77)$, and $C_p = g/\omega$. Donelan et al. suggested a new parametrical form significantly narrower than the Mitsuyasu and Hasselmann equations. This is because the Donelan model was obtained with a higher resolution, using a array of 14 wave staffs in Lake Ontario. The directional spreading function

presented by Donelan is:

$$D(\omega, \theta) = \frac{1}{2} \text{sech}^2 [\beta(\theta - \theta_\omega)]$$

$$\beta = \begin{cases} 2.61 \left(\frac{\omega}{\omega_p} \right)^{1.3}, & \text{if } 0.56 < \omega/\omega_p \leq 0.95 \\ 2.28 \left(\frac{\omega}{\omega_p} \right)^{-1.3}, & \text{if } 0.95 < \omega/\omega_p \leq 1.6 \\ 1.24, & \text{if } \omega/\omega_p > 1.6 \end{cases} \quad (3.19)$$

and satisfy $\int_{-\pi}^{\pi} D(\omega, \theta) d\theta = 1$.

Until now it has been considered the wave spectra in temporal domain, i.e: the frequency measurement of the vertical displacement of a single point (buoy). In order to map the frequency domain to wavenumber domain it is necessary to apply the water waves linear dispersion relationship:

$$S(k) = S(\omega) \frac{d\omega}{dk}. \quad (3.20)$$

Knowing that the following relation holds in deep waters

$$\omega = \sqrt{g \cdot k}, \quad (3.21)$$

we can find

$$\frac{d\omega}{dk} = \frac{g}{2\omega}. \quad (3.22)$$

Substituting Equation 3.22 in Equation 3.20 we can convert the frequency-domain spectrum to the wavenumber-domain.

The next step consist in transform the sea energy distribution spectrum to the SAR image intensity-variance distribution spectrum. The three main transform models are summarized below:

- **Linear Transform:** The first effort focusses on model the SAR transfer function as a linear system and neglect the non linear effects. Under certain conjuncture this assumption can be accepted. As seen in Chapter 3.2 the RCS gets increased for higher surface roughness. But longer waves modify also the RCS in two ways: 1) long waves modify the local surface incident angle and 2) they also interact hydrodynamically with short waves in such a way that alters the roughness. The first effect is known as *tilt modulation* and the second as *hydrodynamic modulation*. This two effects are most sensitive with waves moving in range direction and are also applicable to RAR. The third modulation mechanism is intrinsic of SAR

systems. As seen in Chapter 2.7.1 the azimuth position of a moving target gets modified by its radial velocity. Considering the surface waves as distributed scatterers in motion, at image level the scattering density is increased and decreased, rendering fictitious spatial frequencies components. This effect is known as *velocity bunching*. The transfer function can be expressed as:

$$S_{sar}(k) = T(k) \cdot S(k), \quad (3.23)$$

where $S_{sar}(k)$ is the SAR intensity variance spectrum, $S(k)$ is the wave-height variance spectrum and $T(k)$ is the SAR linear transfer function that takes into account the tilt, hydrodynamic and velocity bunching mechanisms.

- **Quasi-Linear Transform:** Moreover the shifts caused by radial velocities not only affects to long surface waves. The short scale waves are randomly shifted, degrading the azimuthal resolution. This effect introduces an azimuth cut-off in terms of minimum observed wavelengths. That is, SAR cannot see ocean waves shorter than the cut-off wavelength. As seen in Equation 2.22, it is proportional to the range-to-velocity ratio. The higher the (R/V) and the sea state, the higher the minimum wavelength that can be imaged. Considering this effect, the sea spectrum mapping function can be written in a more complete form:

$$S_{sar}(k) = H_D(k) \cdot T(k) \cdot S(k) + S_N(k), \quad (3.24)$$

with $H_D(k)$ modelling the azimuth cut-off and $S_N(k)$ representing the effect of speckle noise on the image spectrum. Note that it can be reduce by multilooking at expense of lose waves of interest.

- **Non-Linear Transform:** The applicability of *Quasi-Linear transform* is limited to low sea states for polar orbits. This motivated the non-linear investigations in more difficult models to retrieve the sea spectrum from SAR images [45] using a inversion process that usually consist in minimizing a cost function.

However these studies requires further background in oceanography and for this reason they have not been included in the simulator.

Chapter 4

MTI techniques and detectors

4.1 Introduction

Moving Target Indication techniques (MTI) are radar signal processing methods to separate moving targets from clutter. The role for MTI processing is the detection instead of the dynamic parameters estimation. In this Chapter are presented the different SBR configurations with MTI capabilities implemented in the simulator. The available MTI techniques are theoretically explained, jointly with their corresponding CFAR detectors. The accomplished method to obtain the probability of detection for a specific target is described. Finally the simulated results carried out with different combinations of SBR configurations and MTI techniques are presented.

4.2 Mission Analysis

With a single channel instrument is not possible to know which targets are in motion (unless its azimuth displaced position from its sea wakes and/or their defocussing effect show otherwise) and much less to detect those targets with a RCS under the clutter-plus-noise level. This problem is solved using multiple receiving channels, which provides another degree of freedom to the signal model.

Current SAR missions TerraSAR-X, TanDEM-X, RADARSAT-2 or COSMO-SkyMed, with more than one receiving channel, highlight the actual state-of-the-art for satellites with MTI capabilities. TerraSAR-X [46] uses the whole antenna for transmitting and synthesize two receiving channels splitting the same antenna in two halves in along-track direction. As shown in Figure 4.1, the azimuth beamwidth of the receiving antennas is doubled compared with the transmitting pattern. The gain for the receiving antenna is

also reduced 3dB as a consequence of reducing the antenna effective area. The TanDEM-X satellite, flying in a close formation with its twin satellite TerraSAR-X (with a baseline of hundred of meters), constitutes an add-on in the mission to form four physical receiving channels. However the main objective of this configuration has been the formation of the Digital Elevation Model (DEM) of the entire world with high accuracy.

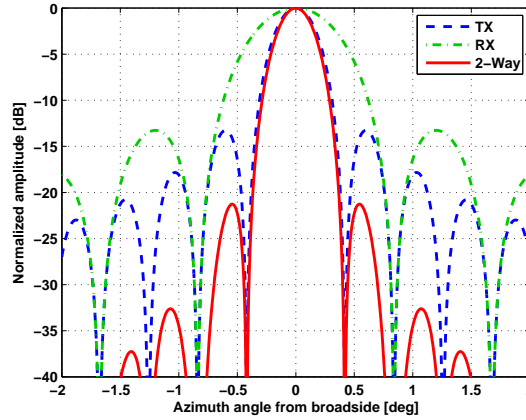


FIGURE 4.1: Azimuth antenna pattern for the complete and halved antenna with a physical length of 4.8 meters and working in X-band.

The RADARSAT-2 was the first satellite including a MTI operation mode: the Moving Object Detection EXperiment (MODEX). This operation mode essentially synthesizes multiple channels by splitting the receiving and transmitting antenna and switching/-toggling the antenna halves during the acquisition time. Figure 4.2 shows the implementation of different MODEX operating modes. It is worth to mention that when the antenna is divided for transmit/receive, the valid PRF interval is considerably reduced owing to the overlapping of pulses. The limitation of PRF's makes this system not suitable for future missions with high performance in MTI capabilities.

The proposed instruments (available in SIMTISYS simulator) are sketched in Figure 4.3. The DRA instrument mimics the TerraSAR-X satellite, with an antenna of 4.8 meters length and 0.7 meters high. The two-way phase centres separation between both channels is 1.2 meters, which allows the detection of targets moving with a high velocity. The TANDEM instrument, tantamount to TerraSAR-X and TanDEM-X satellites, consists in two synchronized SAR satellites operating in a close formation, separated hundred of meters. Both satellites operate in DRA mode, forming four available channels. This configuration guarantees the detection of very slow targets but has a reduced range of unambiguous velocities (i.e. at medium/high velocities the target signal phase between channels rotates an integer number of turns). The BOOM instrument, presented

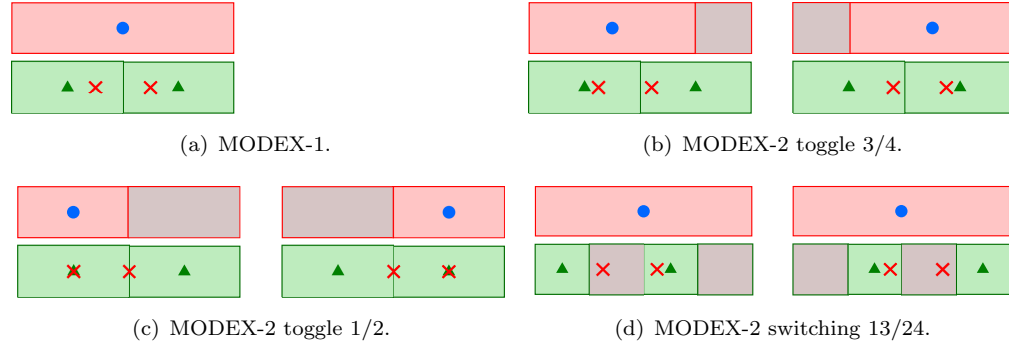


FIGURE 4.2: Implementation of MODEX operational model in RADARSAT-2. The parts in red represents the transmitting antenna and the parts in green the receiving antennae. The parts in gray are not activated. The blue dots are the transmitting phase center, the green triangles are the receiving phase center and the red crosses stands for the equivalent two-way phase center.

in [47], has been designed specifically for MTI purposes. Its configuration assumes a DRA instrument where two external antennas have been added, one using a boom mast structure and the other antenna is unfolded from the satellite body. With this configuration the system operates with four channels with different baselines to increase the detection capabilities of slow moving targets and increase the range of unambiguous velocities.

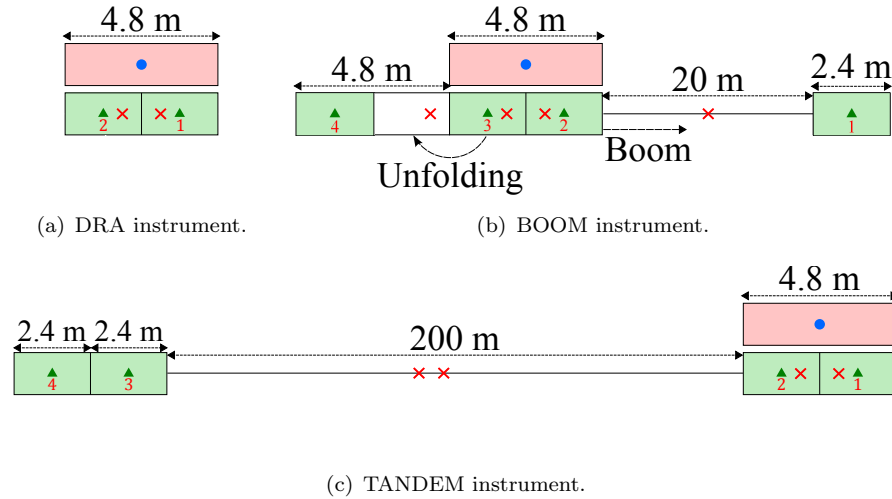


FIGURE 4.3: Definition of SBR configurations used in SYMTISYS simulator. The numbers in red over each receiving antenna represents the channel id number. The spacecraft flight direction is from left to right in all cases.

4.3 MTI Techniques

MTI processing techniques focuses on cancel the stationary clutter and/or concentrate the energy of moving target signal. Owing to the long distance between the satellite and the point of interest and the presence of clutter sampled with a finite PRF, the target signal will have a low SCNR.

The number of existing MTI techniques are limited. There are three main techniques: *Displaced-Phase Center Antenna* technique (DPCA), *Along-Track Interferometry* (ATI) and the *Space-Time Adaptive Processing* (STAP). DPCA and ATI are techniques involving only two channels and are considered suboptimal when more channels are available, in such a case STAP is the most suitable processing method. In the following subsections the three techniques are described.

4.3.1 Displaced Phase Center Antenna Technique (DPCA)

DPCA [48, 49] is a effortless MTI processing involving only two channels which began to be used at 1950s in Early Warning Radars (EWR) of defence. It performs the clutter cancellation by subtracting two coregistrated Single Look Complex (SLC) images. The coregistration (or DPCA condition) consist in shifting the equivalent two-way phase center of the fore and/or the aft antenna, compensating the platform motion, such that over a single pulse repetition interval the antenna appears stationary in time.

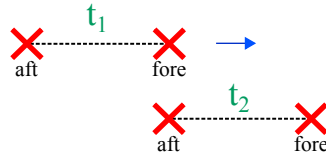


FIGURE 4.4: In DPCA condition the phase center of the aft antenna occupies the position of the phase center of the fore antenna at different instants of time.

The DPCA image results in a high amplitude in those pixels susceptible to contain moving targets. Nevertheless not all the velocities can be detected. The baseline distance between channels will determine the range of unambiguous velocities (induced frequency lower than $PRF/2$), existing always blind velocities (induced phase equal to 0). For an instrument with two channels p and q with a baseline between equivalent phase centres $b_{p,q}$, the blind velocities can be formulated equating the phase difference between channels to a multiple of 2π :

$$\begin{aligned}
\Delta\phi &= 2\pi N \\
2k\Delta R &= 2\pi N \\
v_b &= \frac{2}{\lambda} \frac{V_{sat}}{b_{p,q}} N,
\end{aligned} \tag{4.1}$$

where N is a integer number. The reader must take into account the interferometric phase introduced by bi-static configurations with long baselines (like TANDEM), which produces shifts in blind velocities. In order to avoid unexpected results, it is recommended to remove this phase before performing any MTI processing. Ideally the DPCA technique suppresses the clutter but the presence of *Internal Clutter Motion* (ICM), channel unbalances and coregistration errors deteriorate the clutter cancellation. If the clutter is modelled as a Rayleigh process, in the DPCA image its PDF will remain being Rayleigh.

4.3.2 Along-Track Interferometry (ATI)

ATI exploits the high sensitivity of the interferometric phase to slant range distances variations. It allows both the detection of the target and the estimation of its slant range velocity but without cancelling the clutter. The assumption is that stationary clutter will have a interferometric phase close to zero (the so-called *stationary world*) while moving target will appear in the interferogram with a phase different of zero. The interferogram is formed multiplying one channel image by the complex conjugate image of a second channel aligned in the flight direction

$$\underline{ATI}_{p,q} = \frac{1}{N} \sum_{k=1}^n \underline{x}(k,p) \underline{x}^*(k,q), \tag{4.2}$$

where n is the number of looks, i.e: number of samples averaged in order to reduce the speckle noise. Again both channels must be previously coregistrated, otherwise the interferogram will represent the phase difference due to the distance differences of the bi-static situation.

To demonstrate the capability of ATI for detecting slant range velocities it has been launched a simulation with the scenario represented in Figure 4.5, consisting in nine targets with a RCS of $1m^2$. The radar parameters are shown in Table 4.1 and the target parameters in Table 4.2.

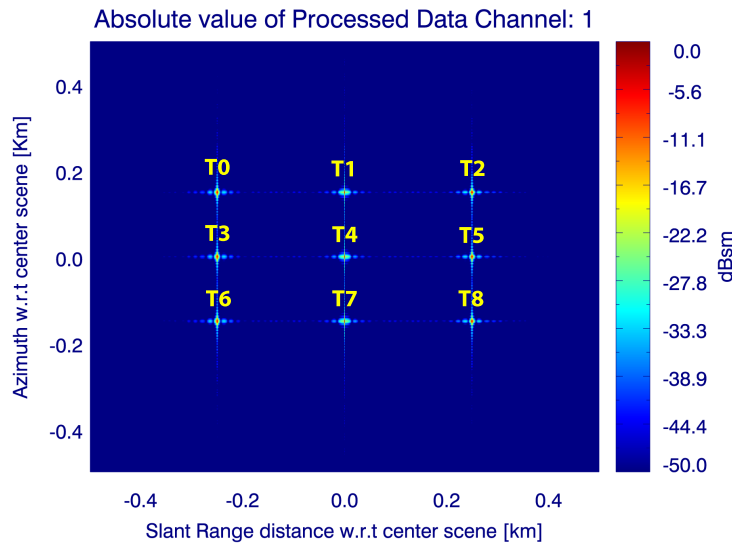


FIGURE 4.5: Representation of the position of targets without dynamic parameters. The image resolution is 2.7 meters in both domains. All targets have a RCS=0 dBsm.

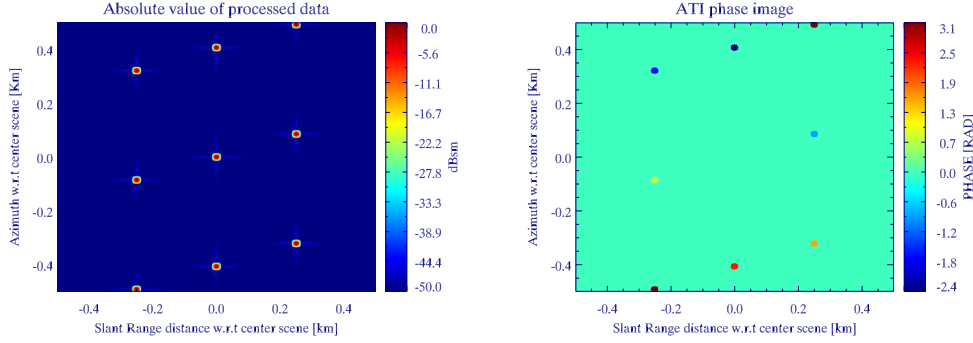
Wavelength	31.08 mm
Radar effective velocity	7344.3128 m/s
Instrument	BOOM
Channels	1 & 4
Baseline	14.8 m
Azimuth & Slant range resolution	10 m

TABLE 4.1: Radar parameters for the analysis of ATI phase variation in moving targets.

Target	Slant range position w.r.t. the center of the scene [m]	Azimuth position w.r.t. the center of the scene [m]	Across-track velocity [m/s]
T0	-250	-150	-1.93
T1	0	-150	-2.89
T2	250	-150	-3.86
T3	-250	0	0.96
T4	0	0	0
T5	250	0	-0.96
T6	-250	150	3.86
T7	0	150	2.89
T8	250	150	1.93

TABLE 4.2: Target parameters for the proposed simulation scenario.

The simulation has been launched with a 10 meters resolution window in order to make more visible the results. The resulting SAR image and the interferometric product are shown in Figure 4.6.



(a) Single channel SAR image modulus result for the aforementioned scenario with the kinematic parameters appearing in Table 4.2. (b) ATI phase for BOOM channels 1 and 4. A threshold has been applied in order to hide the annoying effect of the sidelobes.

FIGURE 4.6: Resulting images after executing the simulation for ATI phase validation purpose.

The well-known ATI phase for moving targets with radial speed v_r can be written as:

$$\Psi = \phi_p - \phi_q = 2 \frac{2\pi}{\lambda} \frac{v_r}{V_{sat}} b_{p,q}. \quad (4.3)$$

The measured phase for each target and the expected phase values can be seen in Table 4.3. The results are in close agreement with Equation 4.3, however a small error in the measured values has been found, which never exceeds the 3 degrees. The variations can be explained by the presence of other targets sidelobes and the fact that only the target in the center of the scene (T_4) matches its maximum value with a sample.

Target	Expected phase difference [rad]	Measured phase difference [rad]
T0	-1.570	-1.611
T1	-2.356	-2.397
T2	-3.142	-3.099
T3	0.785	0.744
T4	0	0.00
T5	-0.785	-0.827
T6	3.142	3.103
T7	2.356	2.317
T8	1.570	1.531

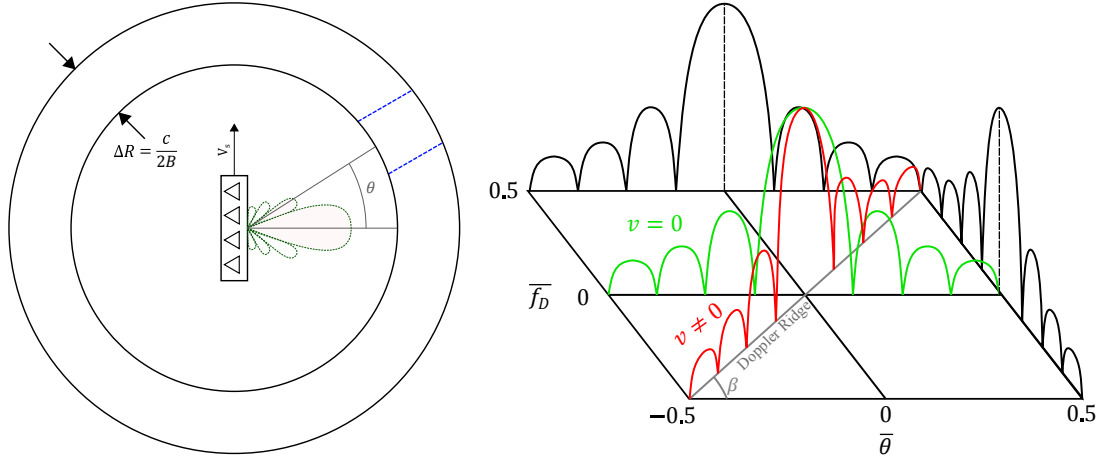
TABLE 4.3: Measured target phase shifts compared with the expected values.

4.3.3 Space-Time Adaptive Processing (STAP)

STAP is a technique used in space-borne/airborne multichannel radars consisting in a joint space and time processing. This technique was originally designed for *Real Aperture Radars* (RAR). In Figure 4.7 is illustrated the distribution of ground clutter power spectral density as a function of the angle of arrival (AoA) and Doppler frequency. As can be seen, when the radar is not moving the static clutter can be cancelled by notching the zero-Doppler frequency. But when the radar is moving, the static clutter echoes experiences a near-linear variation of its Doppler frequency as a function of the angle θ given by:

$$\overline{f_D} = \frac{2vT}{\lambda} \sin \theta = \frac{2vT}{d} \frac{d}{\lambda} \sin \theta = \beta \bar{\theta}, \quad (4.4)$$

where $\beta = 2vT/d$ is defined as the *Doppler ridge* or slope. The received echoes intensity in Doppler Domain mimics the antenna pattern shape, as in the angular domain. Moving targets will appear outside the clutter ridge, providing the possibility to separate them from clutter. However the antenna sidelobes introduces clutter signal that will compete with the target signal.



(a) Picture showing the isorange clutter ring location and the antenna beam pattern for a radar on-board a moving platform. (b) Joint space-time (normalized angle-Doppler) coupled structure weighted by the antenna pattern and showing the clutter ridge signature. The graph in green represents the case for a static radar.

FIGURE 4.7: Ground clutter distribution for RAR airborne case. Adapted from [50].

The well-known solution for STAP is formulated as [50]:

$$\underline{w}_{opt} = k \underline{\underline{R}}^{-1} \underline{s}. \quad (4.5)$$

where $\underline{\underline{R}}^{-1}$ is the clutter-plus-noise covariance matrix, \underline{s} is the steering vector (i.e: the phase progression between the antenna elements for the AoA of the target), and k is an arbitrary constant that does not affect to the SCNR.

The received data arranged by dimensions forms the so-called *Data Cube*, as illustrated in Figure 4.8. Conventional STAP processing takes places over i^{th} slice with N -by- M size, using as optimal filter the solution shown in Equation 4.5. But since now it has not been considered the STAP performance for SAR, where the Doppler domain is used to compress the signal in azimuth in order to form the 2D image. Then in the SBR-SAR case the data cube is composed by several SAR images¹ acquired at slightly different instants. The clutter can be cancelled either in the time/frequency domain after the range compression (raw-data-based GMTI) or in the image domain after SAR compression (SAR-based GMTI). In the first group there are the *Post-Doppler STAP* [51, 52] and the *Imaging STAP* [53, 54] techniques. In the second one is the *Extended-DPCA* algorithm, also known as *Spatial STAP*.

¹In the case of Imaging-STAP the Data cube is not composed by SAR images. The raw data is only range compressed.

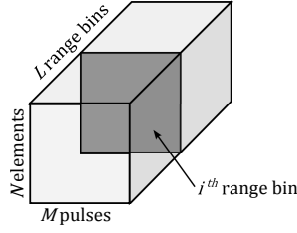


FIGURE 4.8: STAP data cube representation.

4.3.3.1 Post-Doppler STAP

Operates in the range-Doppler domain due to the dependence of the main beam clutter Doppler frequency on the cone angle which causes the clutter echoes to occupy only a few Doppler bins while being present in all pulses. However the dimension of the filter problem must be reduced owing to the large size of the covariance matrix, which means a large computation effort. For this reason these techniques are known as sub-optimum processors and are less sensitive to errors. The taxonomy of post-Doppler STAP algorithms can be found in [55].

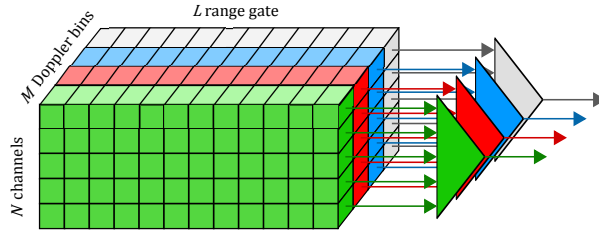


FIGURE 4.9: Post-Doppler STAP adaptive beamformer.

4.3.3.2 Imaging STAP

Imaging STAP is a coherent integration of the post-Doppler STAP outputs to increase the target SCNR, providing a SAR-MTI image as a result. First the data is range compressed and calibrated and then transformed into the Doppler domain without correcting the baseline delay. At this point the data is strongly corrupted by the clutter (high CNR) and its covariance matrix can be well estimated and used to suppress the clutter signal. Then the data is range cell migration corrected and azimuth compressed to be presented in a image format. The target detection is performed at image domain since there is a gain of the SCNR thanks to the azimuth compression.

4.3.3.3 Spatial STAP

Also known in the literature as Extended DPCA, is a generalization of the DPCA technique for any number of receiver channels. The covariance matrix only takes into account the N -channels dimension thereby reducing significantly the computational burden. This sub-optimum technique has been implemented in the simulator where the normalization constant of Equation 4.5 has been set to [56]

$$k = \frac{1}{\sqrt{\underline{s}^H \underline{\underline{R}}^{-1} \underline{s}}}, \quad (4.6)$$

in order to provide a unitary residual interference power.

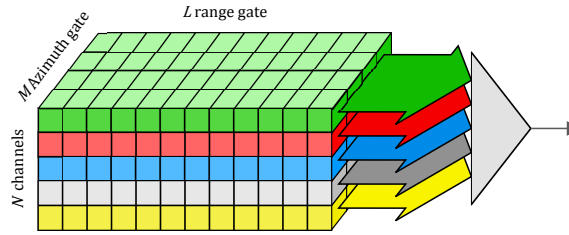


FIGURE 4.10: Spatial STAP adaptive beamformer.

4.4 CFAR Detectors

Constant False Alarm Rate detectors (CFAR) are adaptive algorithms used after the MTI processing, at the end of the simulator chain. Its output provides a binary image separating the vessels from the clutter background. The role of the CFAR is to determine the threshold above which any echo is considered to be target signal. The only input parameter, in addition to the MTI images, is the probability of false alarm.

Usually the CFAR detectors only consider the magnitude of the input signal to detect targets. This is the case of the DPCA and Spatial STAP products, where the phase is neglected owing to the nature of the processing. For those techniques the OS-CFAR (Order Statistics CFAR) has been implemented. In the case of ATI it has been implemented a 2D-CFAR (Two-Dimensional CFAR), where the joint phase and magnitude distribution is taken into account to establish the detection threshold.

4.4.1 OS-CFAR

In the SIMTISYS simulator, to reduce computational cost, the SAR and MTI images are obtained in a small tile area. To simplify the detector implementation the whole SAR

tile is used to estimate the Clutter level. To reduce the impact of possible targets and Clutter edges in the interference level estimation, an Ordered Statistics (OS-CFAR)² has been used [58]. The block diagram of a conventional OS-CFAR detector is shown in Figure 4.11. This technique can be easily extended to 2D data which is the case of SAR image products, or to the output of MTI techniques, as DPCA or STAP. The false alarm rate is constant assuming that the interference (noise + clutter) has a Gaussian distribution. In fact, for properly designed MTI processing, thanks to the clutter cancellation, the underlying interference will be usually dominated by the noise, which is Gaussian distributed. Thus, this algorithm can be used even in the case of non-gaussian clutter distributions if it is highly correlated between the receiving channels.

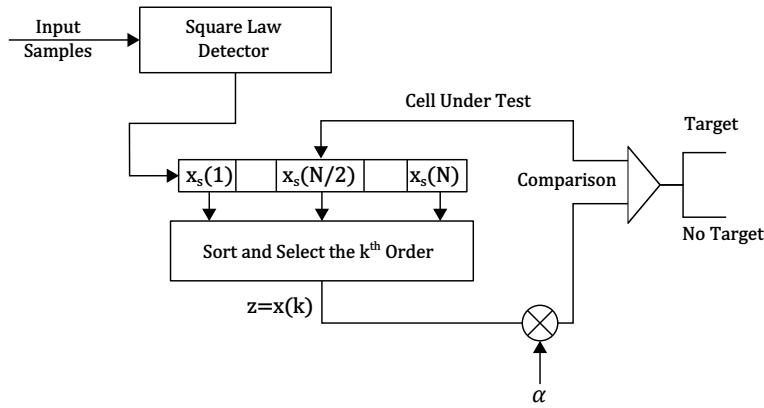


FIGURE 4.11: Scheme of the OS-CFAR.

First of all, the squared absolute value of the image under study is calculated. Therefore, let $x_s(n)$ be the vector that contains all the elements of the processed image, N in total. If the underlying interference is Gaussian distributed, and no target is present, $x_s(n)$ will contain N realizations of an exponential random variable. Then, $x_s(n)$ is sorted in the ascending way, resulting in $x(n)$. The k^{th} element of the sorted list, called k^{th} order statistic is taken, and the threshold to discard the interference is set as:

$$\hat{T} = \alpha \cdot x(k), \quad (4.7)$$

where the α parameter is pre-computed with a desired P_{fa} . The number k is usually chosen between $N/2$ and N . In this analysis k is taken as:

$$k = \frac{3N}{4}. \quad (4.8)$$

²The implementation of the OS-CFAR in the simulator has been carried out by Yu Zhan [57].

Notice that the interference is estimated from a single data sample. Nonetheless, the threshold depends on the whole data, since all the samples are required in order to determine the k^{th} largest element. In [59] it is proven that the algorithm is a CFAR approach, where if the interference signal is Gaussian distributed, x_i will show an exponential distribution with certain interference power σ^2 . The average P_{fa} results in:

$$\bar{P}_{fa} = k \binom{N}{k} \frac{\Gamma(\alpha + N - k + 1)\Gamma(k)}{\Gamma(\alpha + N + 1)}. \quad (4.9)$$

As can be seen, the average P_{fa} remains independent of the interference power σ^2 , thus being a CFAR. If N results in a large number the gamma function is computationally incalculable, and therefore an approximation of gamma function to integer arguments is taken: $\Gamma(n) = (n - 1)!$. The average P_{fa} with factorial expressions is given by:

$$\bar{P}_{fa} = \frac{N!(\alpha + N - k)!}{(N - k)!(\alpha + N)!}. \quad (4.10)$$

Further simplification in the numerator and denominator yields to the final expression, shown in Equation 4.11.

$$\bar{P}_{fa} = \frac{\prod_{i=1}^{\alpha} N - k + i}{\prod_{i=1}^{\alpha} N + i}. \quad (4.11)$$

However, the function is not invertible, because α cannot be expressed in terms of P_{fa} . Therefore, the P_{fa} has been calculated for a range of α values providing a P_{fa} ranged between 10^{-2} to 10^{-8} . Hence, a linear approximation (shown in Figure 4.12) can be used to relate α and $\log(P_{fa})$ and to obtain the required threshold scale factor for the desired P_{fa} .

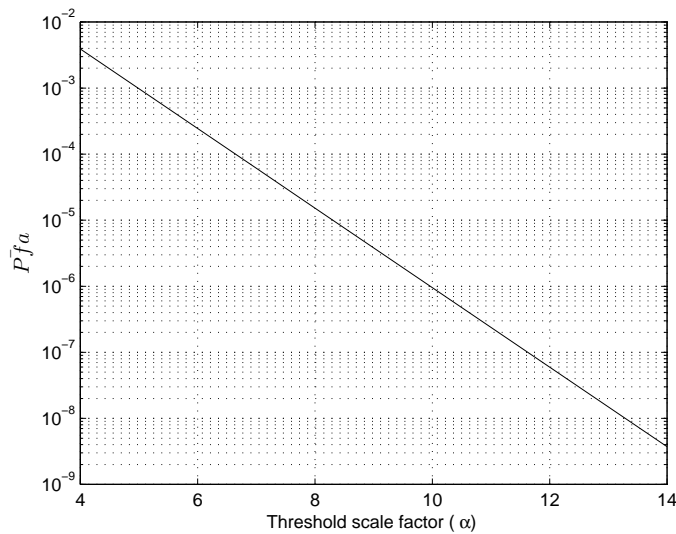


FIGURE 4.12: Average P_{fa} vs. threshold scale factor α .

4.4.2 2D-CFAR

As explained in 4.3.2, ATI exploits the phase differences between echoes of two channels aligned in the flight direction and observing the same scene at different times. However, in order to develop a constant false-alarm rate detector that could separate moving targets from clutter, it is necessary a precise knowledge of the probability distribution of the phase and magnitude. The n -look sample covariance matrix, as the average of several independent samples is given by [60]:

$$\hat{\underline{\underline{R}}} = \frac{1}{n} \sum_{k=1}^n \underline{z}(k) \underline{z}(k)^H = \frac{1}{n} \sum_{k=1}^n \begin{bmatrix} |z_1(k)|^2 & z_1(k) z_2(k)^* \\ z_1(k) z_2(k)^* & |z_2(k)|^2 \end{bmatrix}. \quad (4.12)$$

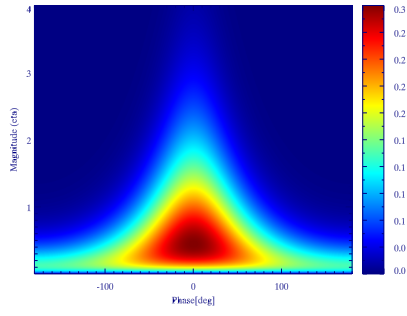
Where n is the number of looks and $\underline{z}(k) = [z_1(k), z_2(k)]^T$ is the k^{th} single-look snapshot. The random matrix $n\hat{\underline{\underline{R}}}$ is well known to be complex Wishart-distributed if the quadrature components of clutter are modeled as a homogeneous zero-mean Gaussian processes. The off-diagonal elements $\eta e^{j\Psi}$ describe the complex multilook interferogram I_n and the underlying covariance matrix is given by [60]

$$\hat{\underline{\underline{R}}} = E [\underline{Z} \underline{Z}^H] = \begin{bmatrix} \sigma_1^2 & \sigma_1 \sigma_2 \rho e^{j\theta} \\ \sigma_1 \sigma_2 \rho e^{-j\theta} & \sigma_2^2 \end{bmatrix}, \quad (4.13)$$

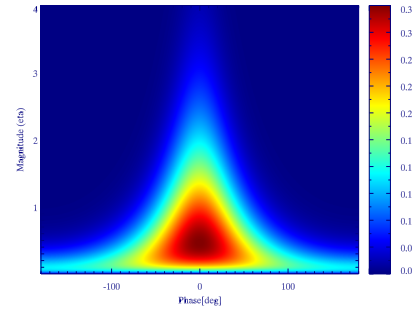
where $\rho e^{-j\theta}$ is the complex correlation coefficient and the magnitude ρ refers to the coherence. Integrating the Complex Wishart distribution with respect to the diagonal elements leads to the joint density function of the multilook interferogram phase Ψ and the normalized magnitude $\epsilon = \eta/(\sigma_1 \sigma_2)$ [60]:

$$f_{\epsilon, \Psi}(\eta, \Psi) = \frac{2n^{n+1} \eta^n}{\pi \Gamma(n) (1 - \rho^2)} \exp \left\{ \frac{2n\eta\rho \cos \Psi}{1 - \rho^2} \right\} K_{n-1} \left(\frac{2n\eta}{1 - \rho^2} \right), \quad (4.14)$$

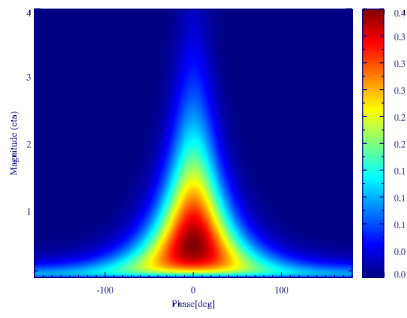
being $K_\alpha(x)$ the modified Bessel function of second kind and order α . Note that the joint PDF only depends on the number of looks and the coherence between channels.



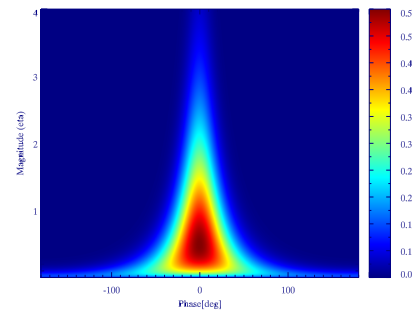
(a) Coherence = 0.6



(b) Coherence = 0.7



(c) Coherence = 0.8



(d) Coherence = 0.9

FIGURE 4.13: One look theoretical joint PDF of interferogram's phase and magnitude for different coherence values.

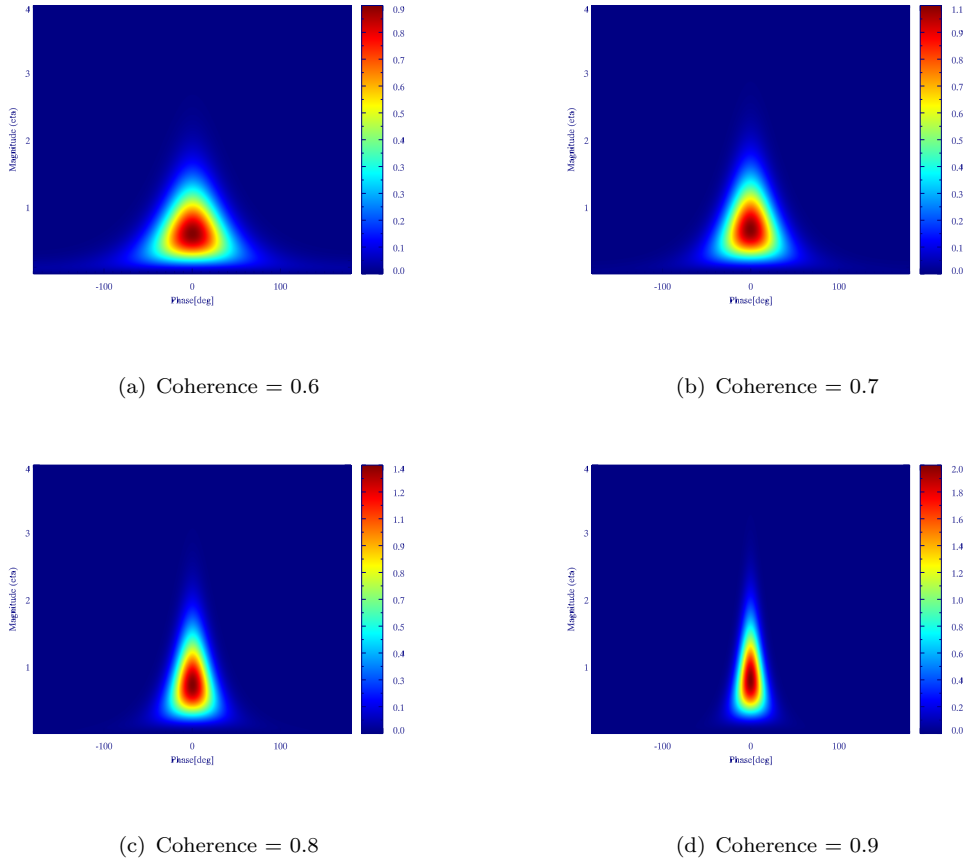


FIGURE 4.14: Four looks theoretical joint PDF of interferogram's phase and magnitude for different coherence values.

The plots depicted in Figures 4.13-4.14 shows the typical behavior of the phase fluctuation: large for small clutter amplitude values and smaller for high clutter amplitude values. Increasing the number of independent looks entails a reduction of speckle, decreasing the phase fluctuation (variance). The same behaviour is observed when increasing the clutter correlation coefficient between channels, which leads to a reduction in the phase variance. In order to determine the combined phase-magnitude threshold, first is necessary to estimate the coherence and the effective number of looks of the interferogram

- **Coherence**

As seen above in the correlation matrix, the complex coherence $\rho \exp\{j\theta\}$ characterizes one of the degrees of freedom of the theoretical interferometric PDF. We can estimate ρ with [61]:

$$\hat{d} = \frac{\sum_{k=1}^n z_1(k) z_2^*(k)}{\sqrt{\sum_{k=1}^n |z_1(k)|^2 \sum_{k=1}^n |z_2(k)|^2}} = \frac{\sum_{k=1}^n z_1(k) z_2^*(k)}{\sqrt{(\sum_{k=1}^n z_1(k) z_1^*(k)) (\sum_{k=1}^n z_2(k) z_2^*(k))}}. \quad (4.15)$$

And taking $\hat{\rho} = |\hat{d}|$ we have the value for the interferogram coherence between channels.

- **Effective number of looks**

The other parameter that we need to estimate is the number of independent samples in the interferogram. Adjacent pixels in real SAR interferograms are statistically dependent due to the SAR processor and filtering, and in consequence the number of looks is usually smaller than the number of averaged samples in the interferogram. The proposed estimator has been presented in [61] and is based on the *method of moments* (MoM), which is fast and robust and reduces the computational load.

MoM is not directly applicable in the interferometric phase because the moments $E\{\Psi^m\}$ for $m = 1, 2, \dots$ cannot be computed analytically for an arbitrary number of looks. Then, the random variable Ψ is transformed into the complex random variable $\Phi = \exp\{j\Psi\}$ and then the moments of Φ are calculated. For a given number of looks n , a realization ϕ of Φ is calculated as a quotient of multilook interferogram and its magnitude:

$$\phi = \frac{\sum_{k=1}^n z_1(k) z_2^*(k)}{|\sum_{k=1}^n z_1(k) z_2^*(k)|} = \frac{\sum_{k=1}^n z_1(k) z_2^*(k)}{\sqrt{(\sum_{k=1}^n z_1(k) z_1^*(k)) (\sum_{k=1}^n z_2(k) z_2^*(k))}}. \quad (4.16)$$

Then, the m^{th} moment of Φ is obtained by:

$$E\{\phi^m\} = I_m(n, \rho) = \frac{\Gamma(n + m/2) \Gamma(1 + m/2)}{\Gamma(1 + m) \Gamma(n)} \rho^m (1 - \rho^2)^n \cdot {}_2F_1\left(n + \frac{m}{2}, 1 + \frac{m}{2}; 1 + m; \rho^2\right) e^{-jm\theta}, \quad (4.17)$$

Where ${}_2F_1(a, b; c; y)$ is the Gauss hypergeometric function, whose calculation can be avoided for some special cases of m , i.e, all even moments have a closed form. Particularizing for the case of $m=2$:

$$I_2(n, \rho) = \begin{cases} 1 + \frac{1-\rho^2}{\rho^2} \ln(1 - \rho^2), & \text{if } n = 1, \\ \frac{(1-\rho^2)^n + (n\rho^2-1)}{(n-1)\rho^2}, & \text{elsewhere} \end{cases} \quad (4.18)$$

And the estimation of the m^{th} moment of the interferometric data can be calculated by:

$$\widehat{I}_m = \frac{1}{k} \sum_{k=1}^k \phi_k^m. \quad (4.19)$$

Thus, finding the roots of the Equation 4.20, we can find \hat{n} , assuming that $\hat{\rho}$ has been estimated via Equation 4.15.

$$I_2(n, \rho) - \widehat{I}_2 = 0. \quad (4.20)$$

Figure 4.15 shows the comparison between the joint phase-magnitude histogram binning of a interferogram composed by clutter+noise, and the theoretical result with the estimated parameters $\hat{\rho}$ and \hat{n} .

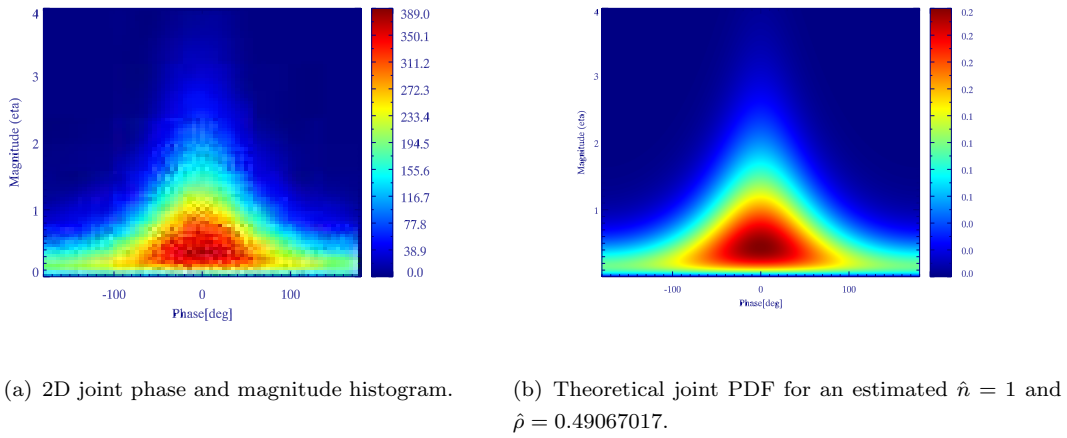


FIGURE 4.15: Comparison between the histogram of joint phase and magnitude and the theoretical PDF estimating its parameters.

Once calculated the theoretical joint PDF, the last step is to find the phase/magnitude threshold for a given probability of false alarm that determines the detection and no-detection zones. The integrated area below the contour line is related with a given P_{fa} . Integrating numerically Equation 4.14, the contour line can be found. Figure 4.16 shows the contours for four different P_{fa} . However it is worth to mention that if the clutter appearing in the tile is not homogeneous (because there is an oil spill, land clutter or another kind of surfaces in the SAR image), both PDF parameters n and ρ will be wrongly estimated.

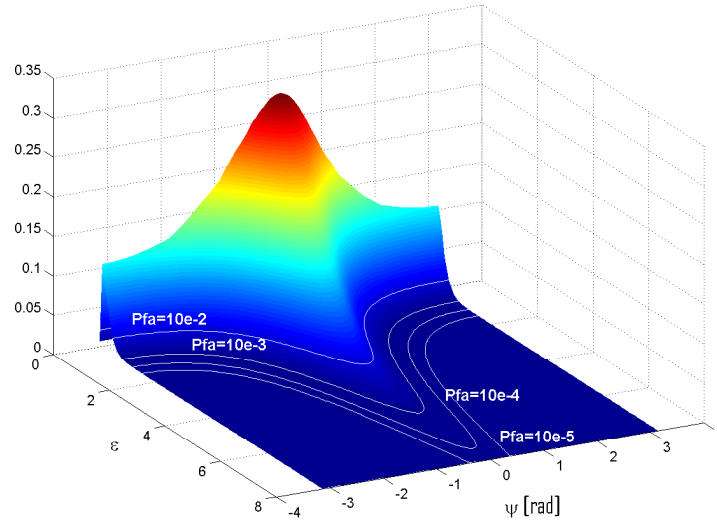


FIGURE 4.16: Theoretical joint PDF interferogram's phase and magnitude for $n = 1$ and $\rho = 0.7$ with the thresholds contours represented for different P_{fa} values.

4.5 Off-line evaluation of the probability of detection

The probability of detection P_d characterizes the performance evaluation for each MTI technique (DPCA, ATI, Spatial STAP). However the single realization of a stochastic process do not provide significant information about its probabilistic entity. On the other hand results not feasible to launch thousands³ of independent simulation trials (generating the raw-data and the MTI images) in order to obtain the probability of detection for a given target. In this situation, *Monte Carlo* (MC) method is a useful procedure to obtain the PDF of the P_d when is difficult to obtain a closed-form expression.

In [47] a SAR-MTI off-line performance simulation tool has been proposed, providing a database containing the P_d for different mission configuration and MTI techniques. Thereby it is possible to know the detectability for a specific target avoiding the generation and processing of thousands of SAR images of the same scenario. The database has been simulated at resolution cell level⁴, as a function of the target radial speed, target radar cross section, probability of false alarm, clutter sigma-zero, clutter coherence time

³For a given P_{fa} , the number of simulated trials needs to be at least two order of magnitudes above $1/P_{fa}$.

⁴Simulating a single pixel instead of a entire tile scenario.

(Equation 3.9), Noise Equivalent Beta Naught [6], Number of looks⁵ and correlation time of the target⁶:

$$P_d = f(Vr, RCS, P_{fa}, \sigma_c^0, \tau_c, NE\beta N, N_{looks}, N_{looks_target_present}, \rho_t). \quad (4.21)$$

Then, jointly with CFAR images, the MTI processing block provides a report of P_d -maps searching the results in the aforementioned database, generated with the radar parameters shown in Table 4.4. The list of available databases for each combination of SBR configuration and MTI processing technique is displayed in Table 4.5. The dimensions of the MTI Database can be found in Appendix E.

Parameter	Value
Platform velocity	7689.0 m/s
Spot ground velocity	71140.0 m/s
Carrier frequency	9.65 GHz
Bandwidth	75 MHz
TX antenna length	4.8 m
PRF	6 KHz
Slant Range resolution	$c_0/(2 \cdot BW)$ m
Azimuth resolution	$L_{TX_ant}/2$ m/s

TABLE 4.4: Definition of off-line performance database simulation parameters.

	DRA	BOOM	TANDEM
DPCA	✓	✗	✗
ATI	✓	✗	✗
Spatial STAP	✓	✓	✓

TABLE 4.5: Chart of available databases for each technique/instrument combination.

⁵In the case of ATI Multilooking is applied.

⁶Neglected in this model approach.

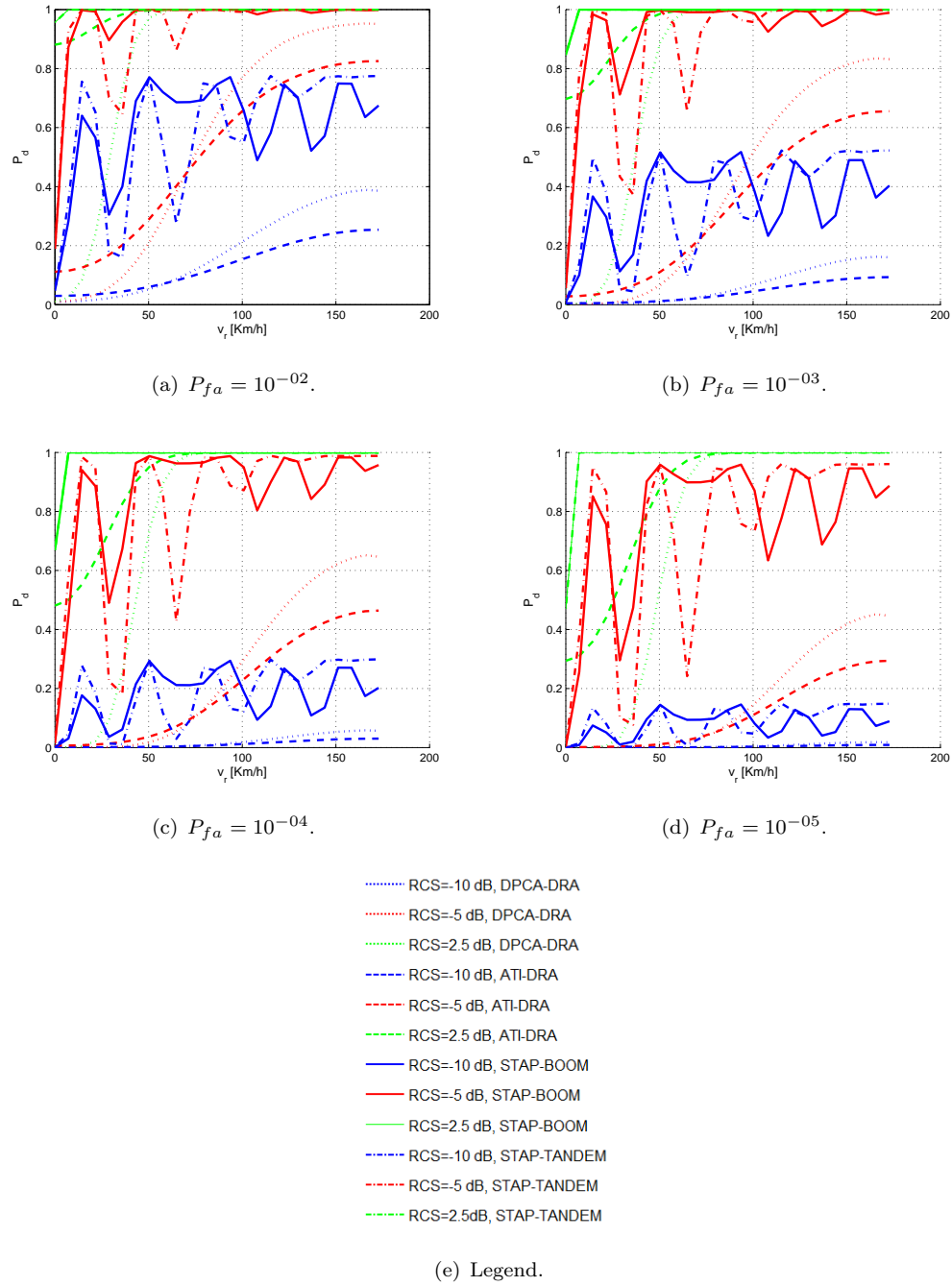


FIGURE 4.17: Database multi-plot of P_d as a function of the radial velocity for $\sigma_c^0 = -15$ dB, $\tau_c = 1$ s and $NE\beta N = -19$ dB for different values of P_{fa} , target RCS , instruments and techniques.

Figure 4.17 shows several "slices" of the database, representing the probability of detection as a function of the target radial velocity. As can be seen, for *BOOM* and *TANDEM* instruments appears a modulation pattern which can be interpreted using the array theory: short baselines produces the low frequency modulation whereas the long baseline introduces the high frequency components that are caused by the grating

lobes introduced in the increased visible range. As expected, the higher the RCS the higher the P_d and the lower the P_{fa} the smoother the the transition from 0 to 1 in the P_d . When a target occupies several pixels over the image it is suitable to calculate the cumulative probability of detection using:

$$P_{d_{cum}} = 1 - \prod_{n=1}^N (1 - P_{d_n}), \quad (4.22)$$

being P_{d_n} the P_d for each target scatterer and N the number of occupied pixels. When in a single resolution cell there exist several scattering points, the RCS is read in the image (as usual) and the kinematics parameters are selected for the scattering point with higher RCS.

The different axis (or DoF) of the database have been sampled with a low number of samples for a low time generation purpose⁷. Owing to the sub-sampling problem there are some axis that experiments a fast transition between 0 to 1 in the P_d for two consecutive values, which cannot be accepted. The solution adopted has been the interpolation of those dimensions in which appears this phenomenon. In the DPCA and Spatial STAP database the v_r , RCS and τ_c have been interpolated and in the case of ATI database the dimensions interpolated have been the v_r , σ_c^0 and τ_c .

Suppose that we want to obtain the performance P_d characterization for a different SBR configuration (different baseline, platform velocity and range resolution). The question is: can we reuse the performance database with the parameters shown in Table 4.4 applying an appropriate scaling of the input parameters? The answer is affirmative under certain conditions, being then the off-line MTI characterization database a flexible tool to analyse any type of configuration/MTI technique. For this reason the techniques involving two channels have been calculated for the DRA instrument and are scaled for other instruments with different baselines. Below are presented the scaling equations applied to reuse the generated MTI database.

4.5.1 Scaling the target radial velocity

In section 4.3.2 was demonstrated that the interferometric phase between channels depends on the channels baseline, satellite velocity, radar wavelength and target radial speed. The first three are determined by the instrument parameters but the last one can be rescaled in order to adjust the SBR configuration.

Using Equation 4.3 it can be formulated the target phase difference for any instrument. Equating for instance the expressions for DRA and TANDEM, and isolating the radial

⁷In the case of ATI with multilooking, the elapsed time for the generation of the database has been in the order of weeks in a server with 16 Intel Xenon CPUs @ 2.40 GHz and 70 GB of RAM memory.

velocity for the DRA case gives:

$$v_{r_{DRA}} = v_{r_{TAN}} \frac{k_{TAN}}{k_{DRA}} \frac{b_{p,q_{TAN}}}{b_{p,q_{DRA}}} \frac{V_{sat_{DRA}}}{V_{sat_{TAN}}}, \quad (4.23)$$

where the subscripts *DRA* and *TAN* refers to DRA and TANDEM instruments respectively, k represents the radar wavenumber and V_{sat} is the satellite velocity. Finally the value of $v_{r_{DRA}}$ is the one used to search the P_d in the database. The values regarding to the *DRA* instrument should be replaced by those appearing in Table 4.4. Even in the *DRA* case, if one of these parameters is different the velocity should be rescaled⁸. It should be pointed out that the phase ambiguities must be considered if $|\Delta\phi| > \pi$, using the phase principal value

$$\Delta\phi_0 = \Delta\phi - 2\pi \cdot \text{Round}[\Delta\phi/(2\pi)]. \quad (4.24)$$

4.5.2 Scaling the clutter correlation time

Different instruments considered (or different orbits) will introduce different inter-channel time lags. Although the coherence time of the clutter will be the same if the sea conditions does not change, the correlation factor will change. The model presented by [33] and discussed in section 3.4.1 assumes that the correlation depends on the $\Delta t_{az}/\tau_c$, and this factor must be preserved. The input parameter in the performance database is τ_c but it is known that $\Delta t_{az} = b_{p,q}/V_{sat}$. Equating the preserved factors for the DRA and TANDEM case for example, and isolating the DRA correlation time, the following expression is obtained:

$$\tau_{c_{DRA}} = \tau_{c_{TAN}} \cdot \frac{b_{p,q_{DRA}}}{b_{p,q_{TAN}}} \frac{V_{sat_{TAN}}}{V_{sat_{DRA}}}, \quad (4.25)$$

which is the equivalent value to be searched in the database.

4.5.3 Scaling the range resolution

It has been seen that the range resolution depends only on the transmitted signal bandwidth. The impact of the range resolution will be different for distributed targets and point targets. For the point targets, the increase of the range resolution does not change the SNR. For distributed targets the higher the range resolution (higher bandwidth) the lower the CNR, and finally it implies that the $NE\beta N$ should be scaled applying:

$$NE\beta N_{DRA} = NE\beta N_{TAN} \frac{BW_{eff_{TAN}}}{BW_{eff_{DRA}}}. \quad (4.26)$$

⁸This statement is applied when scaled the target radial velocity and/or the clutter correlation time.

In the case of applying windows for sidelobes reduction, the effective bandwidth should be used in the formula. The value regarding to the *DRA* instrument should be replaced by the one appearing in Table 4.4.

4.6 Case study

The objective of this section is to analyse the combination of the different configurations/techniques mentioned at the beginning of this Chapter, and show the results and capabilities of the simulator. The radar parameters used for the simulation case study are outlined in Table 4.6. The clutter has been assumed as zero-mean complex Gaussian process, whose mean reflectivity has been obtained with the NRL model (Section 3.2). Clutter parameters are summarized in Table 4.7, where a high sea state (near gale) has been simulated as the worst scenario case.

Parameter	Value	Units
Carrier frequency	9.65	GHz
Pulse duration	50	μ s
PRF	3841	Hz
NESZ	-23	dBsm
Range and azimuth resolutions	2.7	m
Tx/Rx Polarizations	HH	

TABLE 4.6: Radar system parameters.

Parameter	Value	Units
Incidence angle	39.49	deg
Scene extension	1×1	Km ²
Sea state (Beaufort scale)	7	
Wind velocity	16.43	m/s
Wind direction (w.r.t look direction)	0	deg
Sea coherence time	5.67	ms
Clutter sigma-zero	-15.9	dB

TABLE 4.7: Clutter parameters for high sea state.

Three kind of vessels⁹ have been placed in the simulation test scenario: a big cargo ship easy to detect, a medium boat ramshackle suffering high accelerations and a small *rigid-hulled inflatable boat* (RHIB) which is hardly detectable even applying MTI techniques. The scene layout is depicted in Figure 4.19.

To show the capability to generate non-uniform clutters an oil slick has been added with a sigma-zero attenuated 10 dB with respect to the sea level¹⁰.

⁹The EM modelling of the vessels has been carried out by Telespazio Vega.

¹⁰Actually the oil spill reflectivity depends on the sea state conditions. Slightly rough sea surface are good conditions to detect the oil spills, while in smooth surfaces and very rough surfaces the oil spill is not observed in radar images owing to the low reflectivity of the sea or because it is mixed in the water.

Target	Max. RCS [dBsm]	SR vel. [m/s]	AZ vel. [m/s]	SR acc. [m/s ²]	AZ acc. [m/s ²]
RHIB	6	4.50	7.07	3.6	0.01
Ramshackle	17	3.30 to 6.32	-2.10 to -0.45	-2.09 to 0.29	-2.47 to -1.13
Civil cargo	40	3.62 to 4.01	5.63 to 6.28	-1.06 to -0.65	-0.96 to -0.28

TABLE 4.8: Target Parameters for the high sea state.



(a) Civil cargo ship.



(b) Ramshackle vessel.



(c) Rigid-hulled inflatable boat.

FIGURE 4.18: Image of the vessels included in the test scenario.

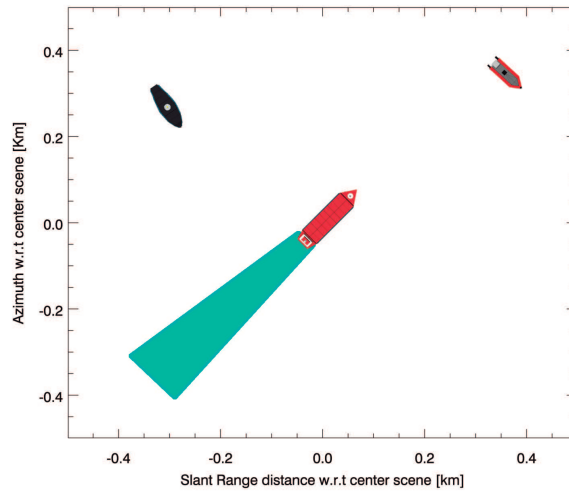


FIGURE 4.19: Test scenario layout composed by a cargo ship, a ramshackle vessel and a RHIB.

The single channel amplitude conventional SAR image is shown in Figure 4.20, where the vessels targets are seen with an azimuth offset owing to the well-known Doppler shift phenomenon. The image level background is caused by the sea surface backscattering

and the radar received noise level. The along track velocities and across-track accelerations produce a moderate/high defocussing recognizable in the ramshackle vessel. Note that the RHIB is hardly detectable owing to its small RCS and high defocussing.

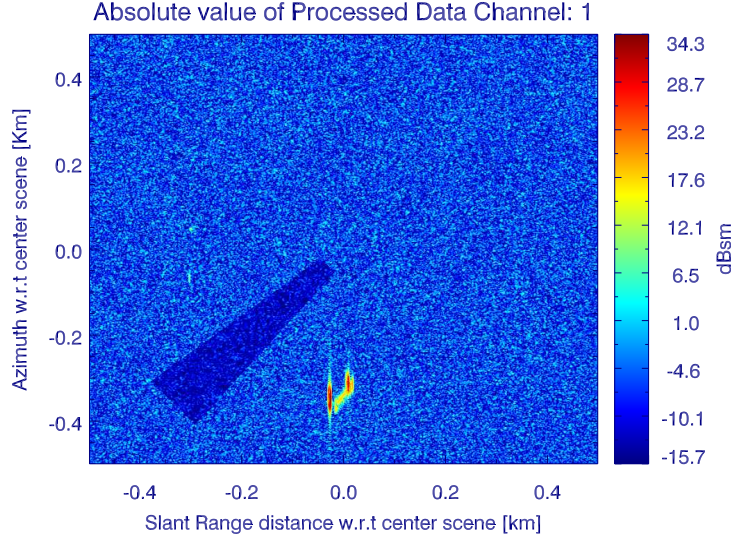
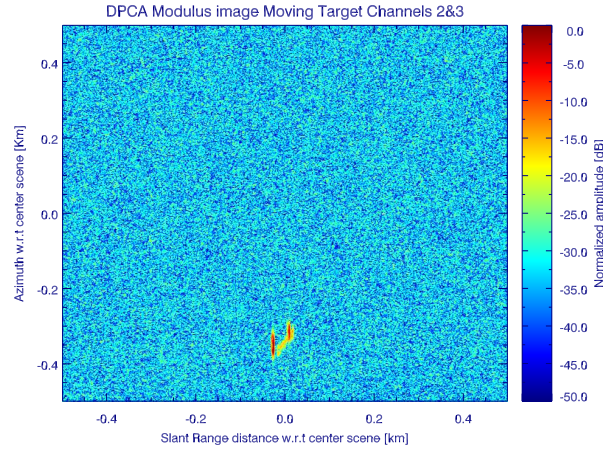


FIGURE 4.20: Modulus of the radar image obtained for the test scenario.

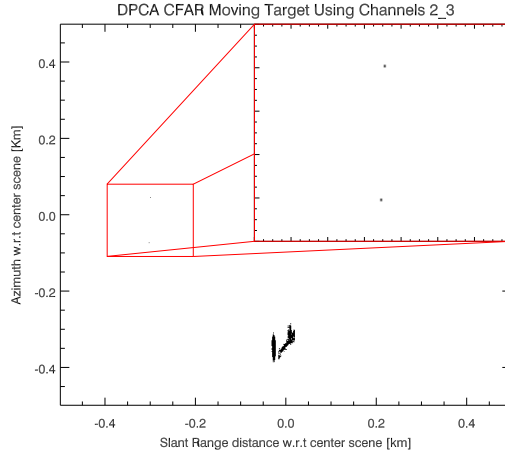
4.6.1 DRA instrument

The first instrument to be analysed is the DRA (Figure 4.3(a)), equivalent to the BOOM mission when considering the channels 2 and 3. The results of applying the DPCA technique are shown in Figure 4.21.

The short baseline between channels makes both corregistered images to have a high similarity in their clutter statistics. The sea clutter is cancelled almost perfectly, making the background image to be the noise level. Realize how the oil slick is not visible. The SCR has been improved but the SNR has been degraded due to the partial cancellation of the targets, which are too slow for the short baseline (1.2 m). A quick validation of CFAR image *vs.* P_D map can be done comparing Figures 4.21(b)-4.21(c). The reason why the ramshackle appears with a high P_D is because it contains some bright pixels that produce the high P_d report. However it may be confused with false alarms.



(a) DRA-DPCA image.



(b) DRA-DPCA CFAR image.

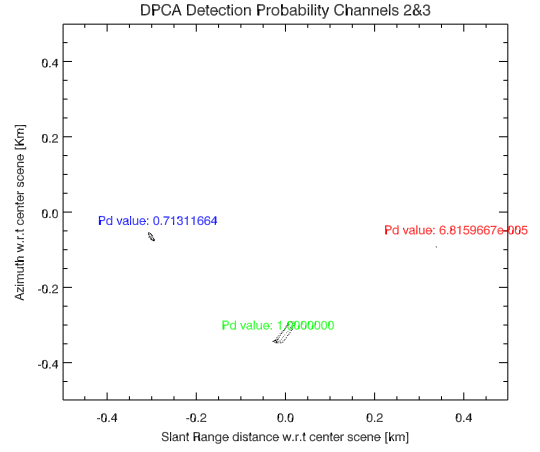
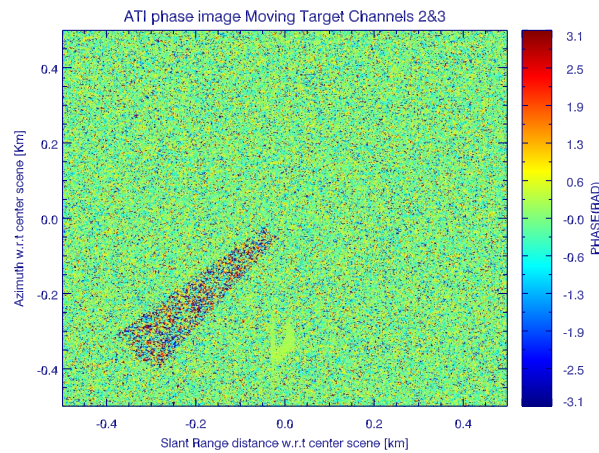
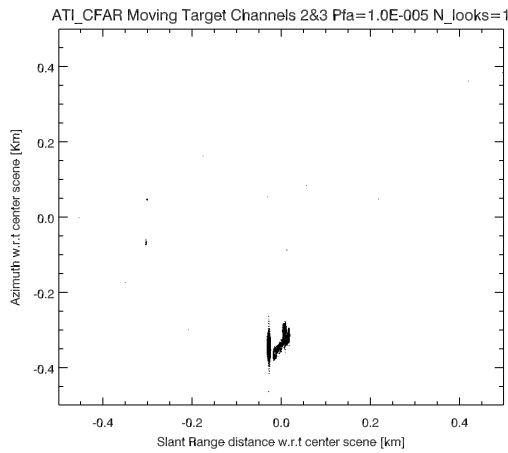
(c) DRA-DPCA P_D map.

FIGURE 4.21: DPCA results with DRA instrument.

The other technique achievable with two channels is the ATI. The results are depicted in Figure 4.22. The interferogram reveals the phase difference for each pixel. In this case, both the cargo ship and the ramshackle are detected by their high echoes amplitude rather than the phase difference between images (see Figure 4.13). As can be seen in the interferogram, targets with a high SCNR exhibit a low noisy phase, which can be used to estimate their radial speeds. But in this situation the shift is very small and the values of the phase are near zero. In this example no multilooking has been applied. The ramshackle P_D has been improved but the RHIB still remains undetectable. Both results shows that DRA instrument is only appropriate for high target velocities.



(a) DRA-ATI phase image.



(b) DRA-ATI CFAR image.

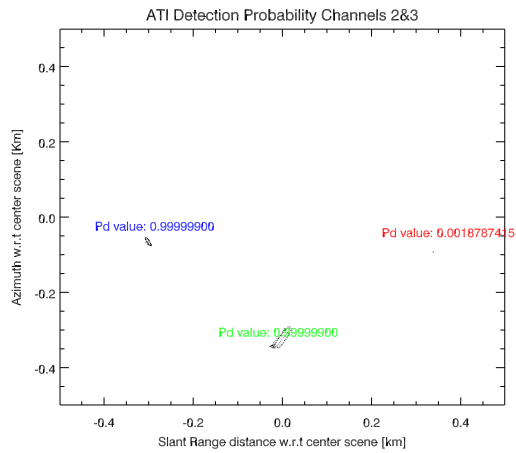
(c) DRA-ATI P_D map.

FIGURE 4.22: ATI results with DRA instrument.

4.6.2 TANDEM instrument

TANDEM (Figure 4.3(c)) is the second instrument which is part of the actual state-of-the-art of multichannel SBR configurations. Its large baseline is the most interesting point for the analysis. The ATI performance results of channels 1 and 4 are shown in Figure 4.24. The phase image exhibit an attitude change in the cargo inertial frame. The larboard and starboard exhibit different radial speeds, as can be checked in Figure 4.23.

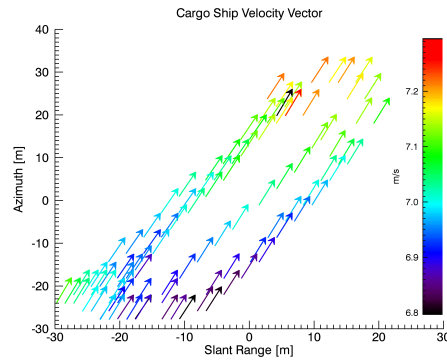
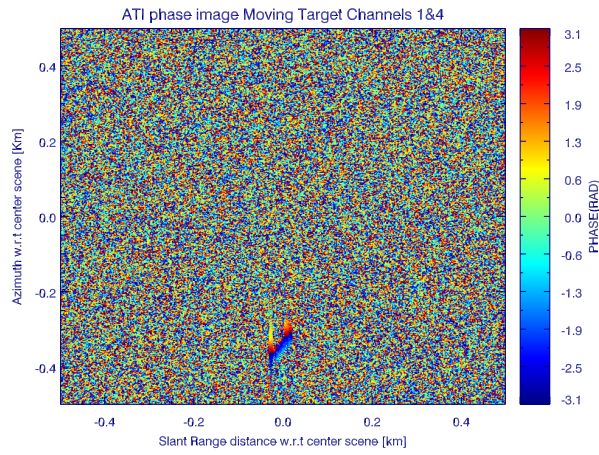
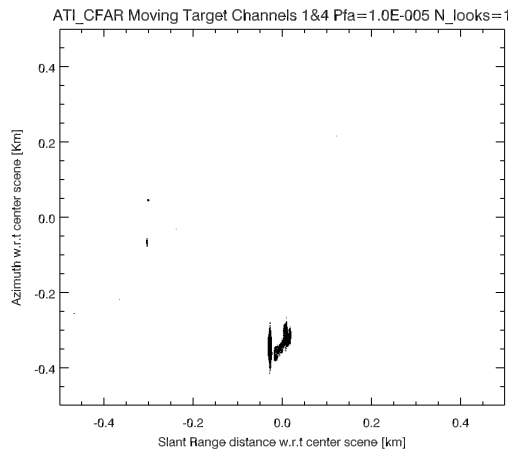


FIGURE 4.23: Velocity vector for each scattering point composing the cargo ship model.



(a) TANDEM-ATI phase image.



(b) TANDEM-ATI CFAR image.

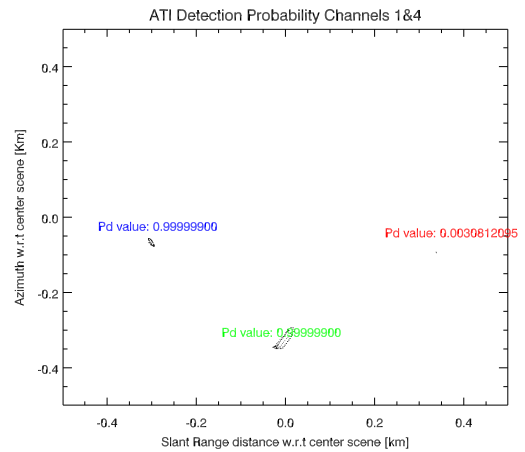
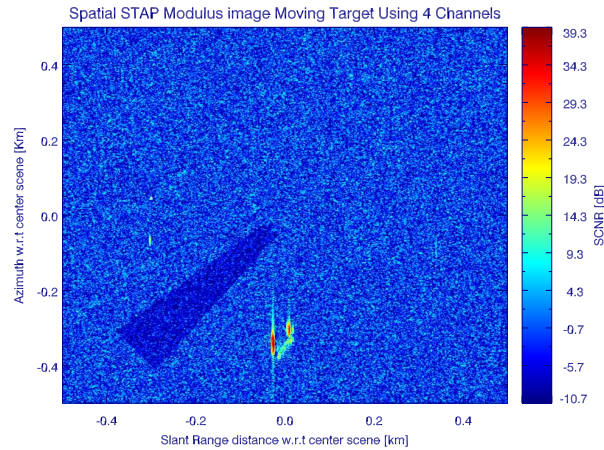
(c) TANDEM-ATI P_D map.

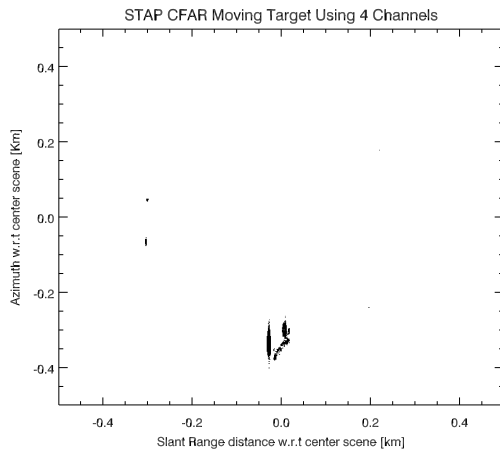
FIGURE 4.24: ATI results with channels 1 and 4 of TANDEM instrument.

However when there are more than two available channels the optimal processing technique is the EDPCA. The steering vector has been set to focus the target with lower RCS but the P_D map results are considering an ideal steering vector for each target. The clutter decorrelation induced by the long baseline limits the clutter signal cancellation and the RHIB for this situation is still undetectable.

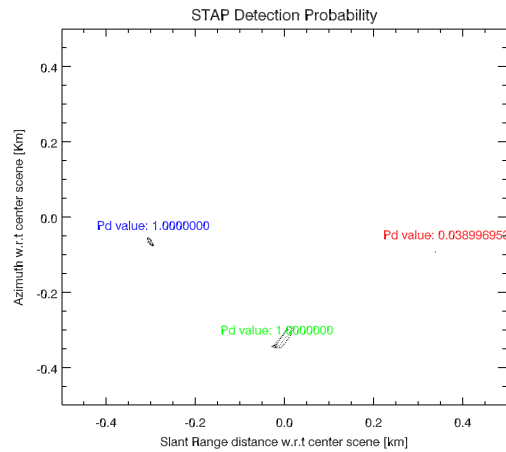
These results void the TANDEM mission for MTI processing. The main purpose of this configuration is to obtain *Digital Elevation Models* (DEM) of the Earth surface.



(a) TANDEM-EDPCA SCNR.



(b) TANDEM-EDPCA CFAR image.

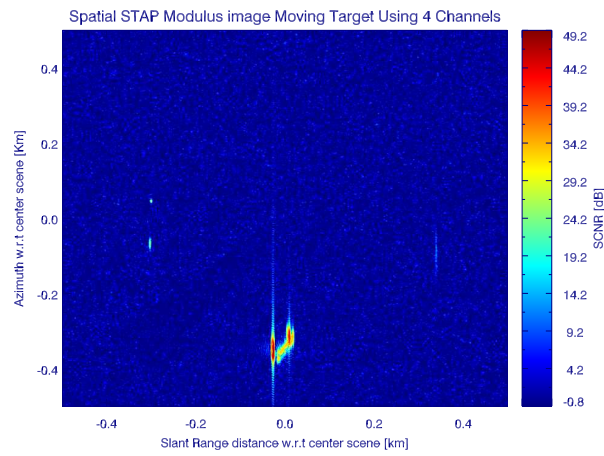


(c) TANDEM-EDPCA P_D map.

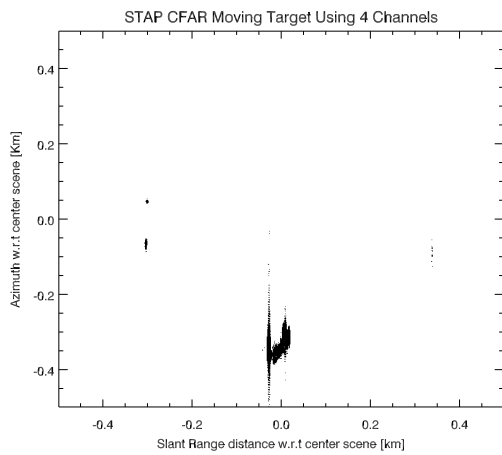
FIGURE 4.25: EDPCA results with TANDEM instrument.

4.6.3 BOOM instrument

The same scenario has been tested with the data acquired with a BOOM instrument. The availability of different baseline lengths makes it an appropriate configuration to detect a wide range of radial velocities. Figure 4.26 shows that despite of the low P_D for the RHIB it is easy to detect in the CFAR image. The disagreement between the P_D map is because the target experiences a severe defocussing and the signal power is smeared over several azimuthal cells. The RCS is measured directly in the radar image where the amplitude losses due to the target kinematics are implicit, and this is done using the target mask. However the mask does not contemplates those adjacent pixels containing part of the defocussed target signal. In this case the RHIB is composed by only two scattering points located at two different pixels. Therefore the cumulative P_D only takes into account two P_D values.



(a) BOOM-EDPCA SCNR.



(b) BOOM-EPDCA CFAR image.

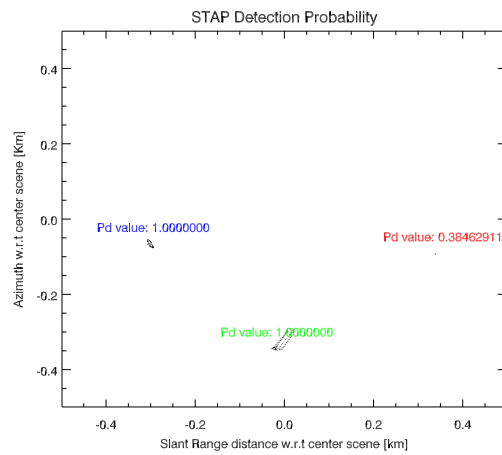
(c) BOOM-EDPCA P_D map.

FIGURE 4.26: EDPCA results with BOOM instrument.

Chapter 5

Simulator structure

5.1 Introduction

This simulator is the result of a teamwork, developed in conjunction with other partners from other universities and companies. For the sake of job sharing it has been divided into different blocks, where each partner has been responsible for the implementation of some of them. The objective of this Chapter is to present the general structure of the simulator and the interconnection between each block, entering in detail into the two modules developed by UPC. The information contained by each generated/inserted file is briefly explained to show how data flows between the different stages. Finally the procedure to execute both UPC modules is explained, independently from the other modules of the simulator implemented by the other partners.

5.2 Block diagram and files format

The overview structure of the simulator and the data exchange between the different blocks is shown in Figure 5.1. The first stage is the *Space Scenario* module developed by Elecnor Deimos. It calculates the propagated satellite orbits and the QoS in terms of space and time coverage for a given constellation of satellites. Next comes the *Earth Scenario* module implemented by Telespazio Vega. It models the scene containing ships (and other marine targets) and provide the information projected in radar coordinates. Finally there are the two blocks developed by UPC. The first one is the *Space Borne Radar* module which calculates the raw data for the delivered scene and generates the SAR images with a SAR processor. The second block is the *MTI* module which is responsible of the generation of the SAR MTI images, CFAR images and the P_d maps.

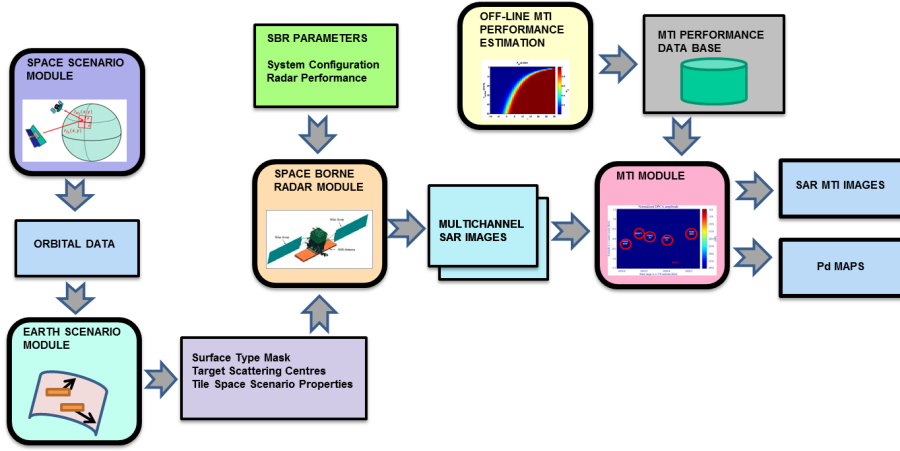


FIGURE 5.1: SIMTISYS simulator block diagram overview.

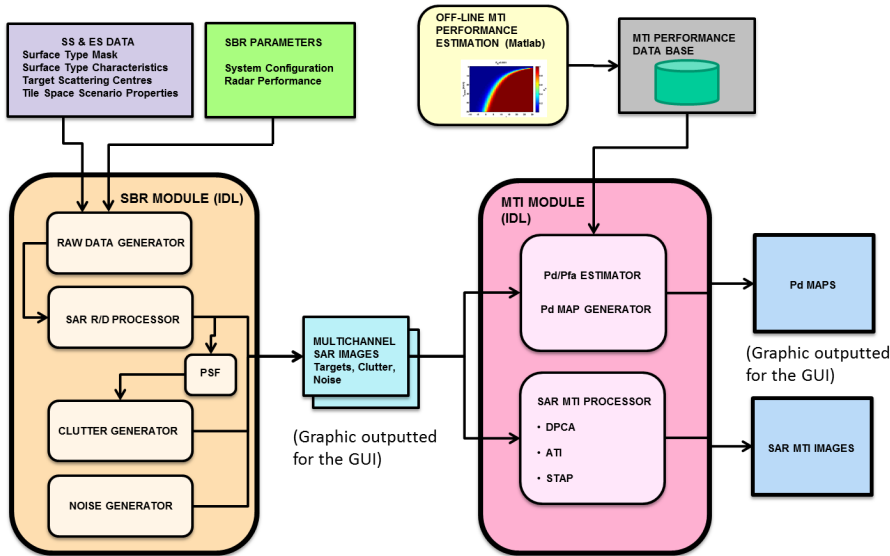


FIGURE 5.2: SBR and MTI intra-block diagram.

A more detailed structure for the UPC blocks is shown in Figure 5.2. For the SBR module there are two NetCDF files delivered by the *Earth Scenario* block: the *Snapshot.nc* and the *Snapshot_scatterers.nc*. The *Snapshot.nc* contains the satellite and ground spot velocities, the surface and target mask in slant range-azimuth coordinates and the tile center properties (slant range to the scene, wind velocity, wind direction and incidence angle). The *Snapshot_scatterers.nc* file gives the target/s information. It consists on a grid where each row entry is a different scattering center and each column contains the vessel id, azimuth position, slant range position, azimuth velocity, slant range velocity, azimuth acceleration, slant range acceleration and the radar cross section (in terms of amplitude and phase) for each polarization combination.

The other input files (*SBR_params.xml*, *RadarModePerformance.nc*, *RadarSysCfg.xml*, *SurfaceTypeCharacteristics.xml*) are supplementary and constants. They contain information as the tapering windows applied, the antenna polarizations, NESZ, pulse lengths, bandwidth and PRF for each subswath. The variation of these parameters should always be to realistic values. It will therefore be the responsibility of the user if their values are changed without considering the consequences. Once loaded the input files, the SBR launches in a first stage the raw data generator and the SAR processor for a static target to calculate the PSF. It is used to calibrate the images and represent them in *dBsm* and for correlate the noise and the clutter. Then, are generated the SAR images containing separately for each channel the target-only layer, the clutter-only layer and the noise-only layer.

Once generated the multichannel images, these are delivered to the MTI module as the main input file. It invokes the processing for each MTI techniques, generating the processed images, the CFAR images and the P_d map reports for each target. Further information about the files structure and format can be found in [62].

5.3 SBR & MTI Stand-Alone applications

Both SBR and MTI modules are ready to work simultaneously under SIMTISYS BUS architecture (implemented by Grupo Sistematica) or in a self-contained manner as a stand-alone application. The first one is selected when the modules are executed from the command line with a input string, which contains the path pointing to the PRF.xml file. The second one is selected when no input PRF.xml file path is specified. This section explains how to execute the UPC modules in stand-alone manner.

5.3.1 Requirements

5.3.1.1 IDL Virtual Machine

In order to execute '.sav' files, the IDL Virtual Machine (IDL VM) needs to be installed in the computer. IDL VM is free to use and does not require a IDL license. However, it is required to register on Exelis website (<http://www.exelisvis.com/Support/HelpArticlesDetail/TabId/219/ArtMID/900/ArticleID/12395/The-IDL-Virtual-Machine.aspx>).

5.3.1.2 Folder Structure

Both modules reduces the number of needed input files in order to simplify the Graphic User Interface (GUI). In consequence, the unalterable files are always sought from a root directory with a determined structure specified in Figure 5.3.

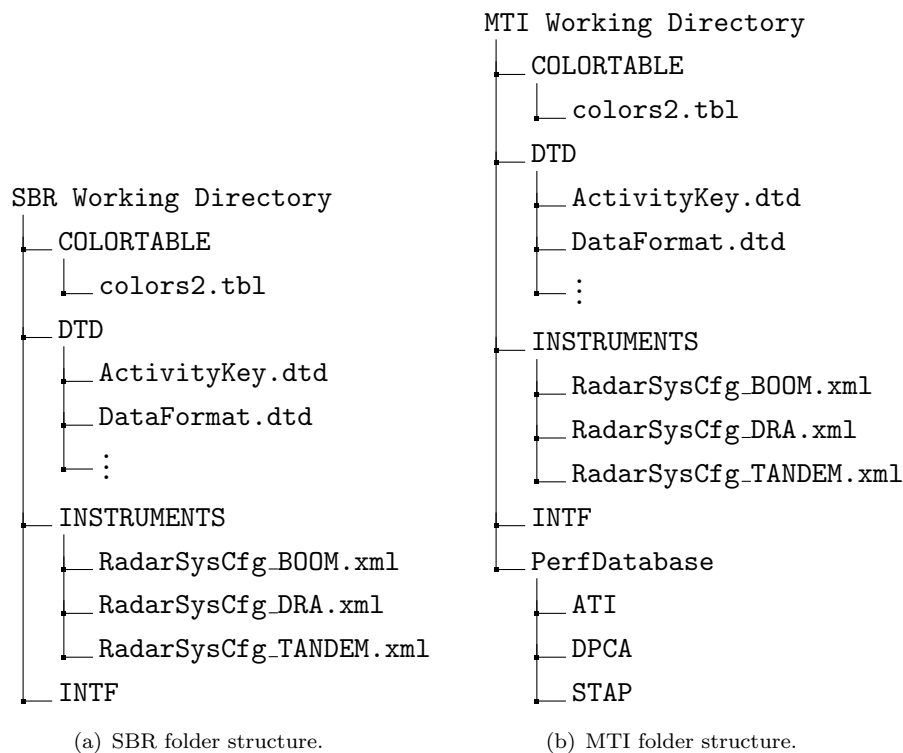


FIGURE 5.3: Mandatory folder structures for Stand-Alone operation modes.

Notice that the only difference between 5.3(a) and 5.3(b) is the PerfDatabase folder containing the off-line performance database.

The output products (EPS images and NetCDF files) are always stored in the root directory (i.e: SBR and MTI Working Directory). In addition to the natural SBR output products, the *snapshot.nc*, *snapshot_scatterers.nc* and the *radarModePerformance.nc* files are generated by the SBR module from the data introduced by the user in the GUI. The *.sav* executables can be allocated in any directory.

5.3.2 SBR Module GUI

To run the SBR module by double-clicking in the *SBR.sav* icon or by the Windows command line typing the following instructions:

```
>cd C:\Program Files\Exelis\IDL82\bin\bin.x86_64
>idlrt -novm -rt=C:\...\SBR.sav
```

The paths can vary depending where the files are located. Once executed the *SBR.sav*, the pop-up window showed in Figure 5.4 will appear.

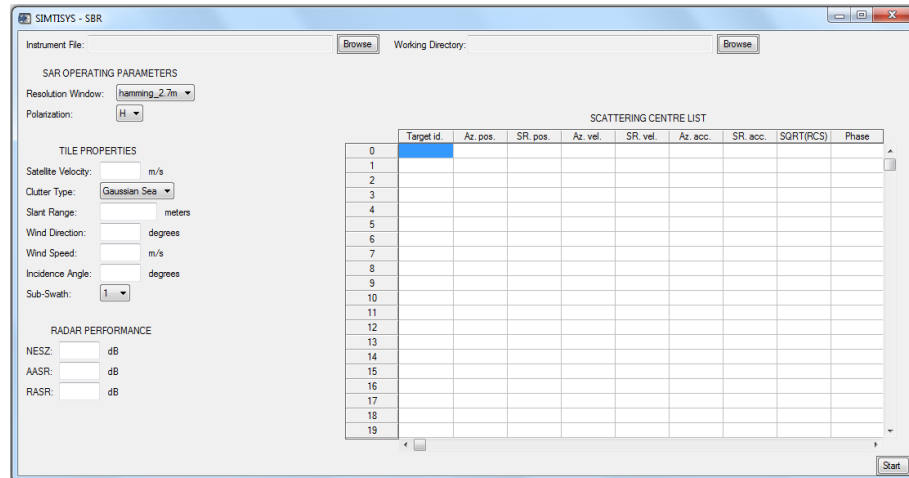


FIGURE 5.4: SBR GUI.

- **Instrument File:** Select one of the available *.xml* instruments files [DRA, BOOM, TANDEM] located in the SBR\INSTRUMENTS folder.
- **Working Directory:** Select the folder containing the same files and structure than are shown in Figure 5.3(a).
- **SAR Operating Parameters:** The polarization of the instrument and the resolution window can be selected by the drop down list. The resolution windows have been named by their resolution provided. This interface do not allows the user to select the azimuthal and slant range resolution windows independently.
- **Tile Properties:** In this section the user defines the scenario view properties of the satellite and the sea clutter features. **Realistic values are expected** and the user is responsible to avoid geometrical errors such as divisions per zero, memory overflow, ... The units are specified on the right side of the text boxes. If no number is introduced (blank space) the module will assign for those variables the zero value by default. The clutter can be only Gaussian, therefore **do not select K-distributed clutter in the Clutter Type list**.
- **Radar Performance:** The user can select the noise level in terms of Noise Equivalent Sigma Zero (NESZ). The ambiguities are not considered in this version, therefore the AASR and RASR are dummy variables.

- **Scattering Centre List:** In this chart the user can introduce the azimuth and slant range positions, velocities¹ and accelerations in MKS system of units. The two last columns refers to the Radar Cross Section (RCS) for the point target for the selected polarization. The magnitude is introduced considering the \sqrt{RCS} and the phase is introduced in radians. The first column represents the Target Identification Number, and is used by the MTI module to report the probability of detection for each target. Note that the number of scattering centres is necessarily equal or higher than the number of targets in the scene. The Target ID flag is also used to know the number of scattering centres in the list, thereupon it is necessary to: (1) **Introduce the target ID for each scattering centre**, and (2) **The Target ID must be an integer number greater than 0**. Once again, blank spaces are read as zero valued.

After setting all the parameters push the *Start* button.

5.3.3 MTI Module GUI

Run the MTI module as explained in Section 5.3.2, substituting the *SBR.sav* by *MTI.sav*. The window showed in Figure 5.5 will appear.

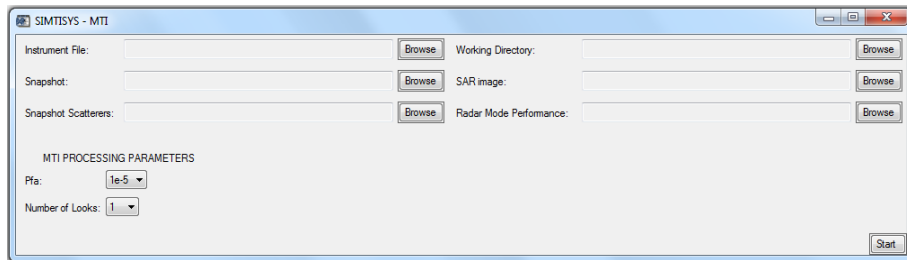
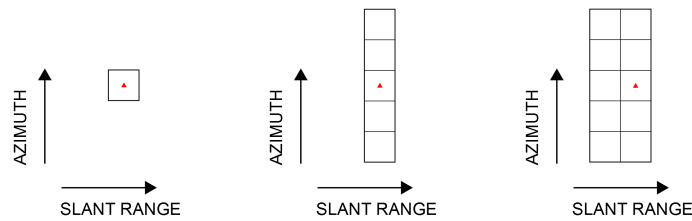


FIGURE 5.5: MTI GUI.

- **Instrument File:** Select the same instrument used in the SBR module.
- **Snapshot:** Select the *Snapshot.nc* file generated by the SBR module and located in the SBR Working directory.
- **Snapshot Scatterers:** Select the *Snapshot_Scatterers.nc* file generated by the SBR module and located in the SBR Working directory.
- **Working Directory:** Select the folder containing the same files and structure than are shown in Figure 5.3(b).

¹The simulated scenario is 1 km x 1 km, hence consider the azimuth Doppler shift phenomenon ($\Delta_{az} = -R_0 \frac{V_{sr}}{V_{sat}}$) when introducing the slant range velocity values. Otherwise the target could appear outside of the tile.

- **SAR image:** Select the *synthetic_SAR_images.nc* file generated by the SBR module and located in the SBR Working directory.
- **Radar Mode Performance:** Select the *radar_mode_performance.nc* file generated by the SBR module and located in the SBR Working directory.
- **MTI processing parameters:** Select the probability of false alarm for the CFAR Detectors (10^{-2} , 10^{-3} , 10^{-4} , 10^{-5}) and the Multilooking window used in the ATI technique (1,5,10). The available Multilooking windows are shown in Figure 5.6.



(a) One look window. (b) Five looks window. (c) Ten looks window.

FIGURE 5.6: Multilooking windows.

Chapter 6

Conclusions and future work

In this Final Thesis a simulator that generates multichannel SAR images and process them with three MTI techniques has been implemented. The first issue founded was that the noise is a critical aspect in SAR MTI systems. The TerraSAR Next Generation outlook previews to solve this problem improving the NESZ ($\ll -23$ dB). Moreover adding a secondary payload for detecting AIS signals to give surveillance maritime capabilities to the future TerraSAR mission has been considered [63]. In this project the improvement of the noise level increasing the antennae lengths has been examined. This result plus the fact that antenna arrays are very expensive has led to design a new BOOM instrument consisting in three receiving channels instead of four, and with an azimuthal length of 4.8 m for both transmitting and receiving situations. Other techniques not analysed in this thesis which are noteworthy are based on *Multiple-Input Multiple-Output* (MIMO) radar. They synthesize more virtual channels by transmitting simultaneously multiple waveforms and provide the opportunity to map wider swaths with better spatial resolution. What is certain is that future SBR missions will be multi-static, full-polarimetric and will implement *Digital Beamforming* to ameliorate the imaging performance. The availability of a constellation of satellites, as planned in the *Copernicus Programme*, will be able to monitor our oceans with a lower interval of revisit times.

Sea models needs to be improved in order to give a more realistic aspect. Although being discussed in Chapter 4, the spectral models and the K-distribution have not been included and cross-polar cases have not been considered owing to the lack of reflectivity models. Further investigations needs to be carried out in this area and future missions observing the sea at mesoscale will help to perform them. The other not considered aspect in the simulator has been the wakes. In addition to the direct radar return from ships, the track left in the water by a moving target provides a clue that can be used for detect them. However this opportunity only appear under certain conditions.

For MTI techniques, it has been found that ATI is more powerful than what was initially suspected. The main drawback is the development of analytical joint-PDF in order to obtain the appropriate CFAR thresholds. The STAP technique has provide the better results, as expected, but it is worth to mention that the ideal covariance matrix has been used and the steering vector is adapted always to the target motion when generating the P_d maps. For the case of images they are always generated with the steering vector pointing to the target with lower RCS. It would be interesting to evaluate the performance of STAP over realistic scenarios, exploiting also the spatial correlation of the seas. Accelerations have been demonstrated to be an important aspects usually ignored in MTI analysis. The bouncing motion of fast boats, for example, causes a severe losses in target amplitude and detection probability. For this reason, without previous knowledge of kinematics, the best STAP performance is the cancellation of the clutter in the range/Doppler domain (as Post-Doppler STAP), previously using the well-known technique of *Matched-Filter Bank* (MFB) to refocus the targets in the azimuth domain. For example, in Section 2.7.2 was found a criterion that can be used to tune the filters. It would be appropriate, for a more precise evaluation in the probability of detection, recalculate the MTI off-line database with a better decision in the sampling of parameters. Besides the three parameters RCS , $NE\beta N$, and σ_c^0 it is more convenient the usage of relative measures as the SNR and CNR, in order to erase one dimension. The ambiguities have not been taken into account in this Final Thesis. Their consideration will introduce clutter signals from antenna sidelobes not correlated with the mainbeam clutter signal, and will impact over the MTI processing decreasing its performance.

The developed simulator gives the guidelines for MTI analysis, SBR design and characterizes the system detection limits for a investigation area that is currently exploited by civil radar missions.

Appendix A

Pulse compression signal approach

The derivation of the spectrum of chirp signals is useful for validation purposes when developing a SAR system. However the precise formulation is difficult, and the widely used method to extract the expression is the *Principle Of Stationary Phase* (POSP). For a FM signal like 2.5, the expression can be written as

$$s(t) = w(t) \exp\{j\phi(t)\}, \quad (\text{A.1})$$

being $w(t)$ the real-valued envelope and $\phi(t)$ the phase modulation. Making the Fourier transform of A.1:

$$\begin{aligned} S(f) &= \int_{-\infty}^{\infty} s(t) \exp\{-j2\pi ft\} dt \\ &= \int_{-\infty}^{\infty} w(t) \exp\{j\phi(t) - j2\pi ft\} dt \\ &= \int_{-\infty}^{\infty} w(t) \exp\{j\theta(t)\} dt, \end{aligned} \quad (\text{A.2})$$

where $\theta(t) = \phi(t) - 2\pi ft$ represents now the unified phase terms. Solving the above integral can be quite difficult but the POSP exploits the fact that the important interval that contributes to the integral lies in the neighbourhood of the point t_s where the derivative is equal to zero ($d\phi(t)/dt = 0$). Intervals where the phase varies fast are self-cancelled and the result can be approximated by zero. Without going any farther, the chirp spectrum can be expressed as

$$G(f) \approx C_1 W(f) \exp\{j(\Theta(f) \pm \pi/4)\}, \quad (\text{A.3})$$

with the variables representing the following:

- C_1 is a constant normally ignored, and equal to

$$C_1 = \sqrt{\frac{2\pi}{|\frac{d^2}{dt^2}\theta(t_s)|}}. \quad (\text{A.4})$$

- $W(f)$ is a scaled version of the time domain envelope $w(t)$

$$W(f) = w[t(f)]. \quad (\text{A.5})$$

- $\Theta(f)$ is a scaled version of the time domain phase $\theta(t)$

$$\Theta(f) = \theta[(f)]. \quad (\text{A.6})$$

The POSP is an accurate approximation when the time-bandwidth product is higher than 100. An example of spectrum is depicted in Figure A.1 with a rectangular window envelope. The plot exhibits the Gibbs phenomenon at the edges of the spectrum.

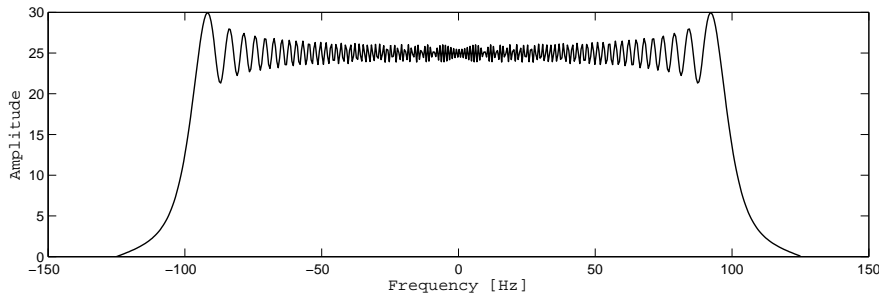


FIGURE A.1: Spectrum of the chirp signal of Figure 2.3, with a bandwidth of 200 Hz.

The other point of interest is the derivation of the output signal of the matched filter in time domain. Solving 2.7:

$$\begin{aligned} s_{out}(t) &= s_r(t) \otimes h(t) \\ &= \int_{-\infty}^{+\infty} \Pi\left(\frac{u}{T}\right) \Pi\left(\frac{t-u}{T}\right) \exp\{j\pi k_r u^2\} \exp\{-j\pi k_r (t-u)^2\} du \\ &= \exp\{-j\pi k_r t^2\} \int_{-\infty}^{+\infty} \Pi\left(\frac{u}{T}\right) \Pi\left(\frac{t-u}{T}\right) \exp\{j2\pi k_r tu\} du. \end{aligned} \quad (\text{A.7})$$

Changing the integration limits regarding to when rectangular pulses overlaps gives:

$$\begin{aligned}
s_{out}(t) &= \exp\{j\pi k_r t^2\} \left(\prod \left(\frac{t+T/2}{T} \right) \int_{-T/2}^{t+T/2} \exp(j2\pi k_r tu) du \right. \\
&\quad \left. + \prod \left(\frac{t-T/2}{T} \right) \int_{t-T/2}^{T/2} \exp(j2\pi k_r tu) du \right) \\
&= \frac{(t+T)}{2} \prod \left(\frac{t+T/2}{T} \right) \text{sinc}[k_r t(t+T)] + \frac{(t-T)}{2} \prod \left(\frac{t-T/2}{T} \right) \text{sinc}[k_r t(t-T)] \\
&= \frac{T-|t|}{2} \prod \left(\frac{t}{2T} \right) \text{sinc}[k_r t(T-|t|)].
\end{aligned} \tag{A.8}$$

The last term of Equation A.8 can be separated in two parts: one with slow varying envelope $((T-|t|)/2) \text{rect}\{t/(2T)\}$, and other with rapidly varying envelope arising from the $\text{sinc}[k_r t(T-|t|)]$. But with a high time-bandwidth product value and around the point $t = 0$, the matched filter output signal can be approximated by:

$$s_{out}(t) \approx \frac{T}{2} \text{sinc}(k_r T t). \tag{A.9}$$

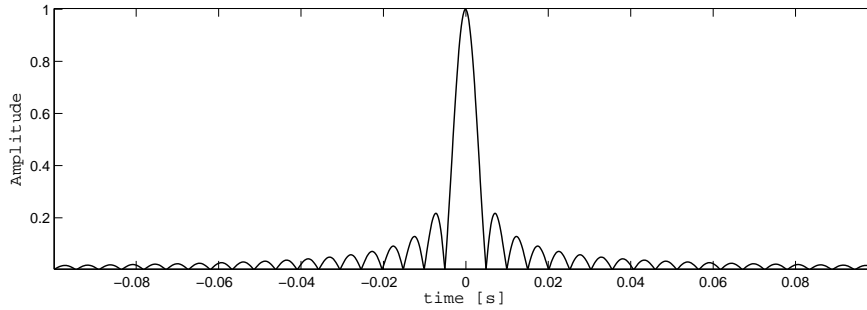


FIGURE A.2: Representation of compressed chirp of Figure 2.3.

Appendix B

RDA processing steps

The first step of RDA consist in compressing the raw data in range for each azimuthal time domain. The range compression is readily computed as a convolution of the received echo with the matched filter, as seen in section 2.3.1. Recalling to Equation 2.13, and using the parabolic expression of 2.14, the range compressed signal can be represented by:

$$S_{rc}(\tau, \eta) = A_0 \rho_r \left(\tau - \frac{2R(\eta)}{c} \right) w_a(\eta - \eta_c) e^{-j\frac{4\pi f_0 R_0}{c}} e^{-j\pi \frac{2V_{eff}^2}{\lambda R_0} \eta^2}, \quad (\text{B.1})$$

with ρ_r representing the range compressed pulse envelope, i.e. the sinc-like function. The last phase term shows a FM linear modulation in azimuth domain with a chirp rate $k_a = 2V_{eff}^2/(\lambda R_0)$ and instantaneous azimuthal frequency $f_\eta = -k_a \cdot \eta$. Rewriting Equation 2.14 gives:

$$R(f_\eta) \approx R_0 + \frac{V_{eff}^2}{2R_0} \left(\frac{f_\eta}{k_a} \right)^2 = R_0 + \frac{\lambda^2 R_0 f_\eta^2}{8V_{eff}^2} = R_0 + \Delta R(f_\eta), \quad (\text{B.2})$$

with the range cell migration expressed in frequency domain. The *range cell migration correction* (RCMC) can be then implemented multiplying the spectrum by the following linear phase:

$$G_{rcmc}(f_\tau) = e^{j\frac{4\pi f_\tau \Delta R(f_\eta)}{c}}. \quad (\text{B.3})$$

Then, taking the azimuthal Fourier transform of the compressed signal, we obtain:

$$S_{rc}(\tau, f_\eta) = \mathcal{F}_\eta\{S_{rc}(\tau, \eta)\} = A_0 \rho_r \left(\tau - \frac{2R(\eta)}{c} \right) \beta_a(f_\eta - f_{\eta c}) e^{-j \frac{4\pi f_0 R_0}{c}} e^{j\pi \frac{f_\eta^2}{\kappa_a}}, \quad (\text{B.4})$$

where the azimuth antenna pattern $w_a(\eta)$ is now transformed to $\beta_a(f_\eta)$ and the second exponential term is the azimuthal modulation. Multiplying by Equation B.3 to correct the migration, the received range-compressed migration-corrected signal is:

$$S_{rcmc}(\tau, f_\eta) = A_0 \rho_r \left(\tau - \frac{2R_0}{c} \right) \beta_a(f_\eta - f_{\eta c}) e^{-j \frac{4\pi f_0 R_0}{c}} e^{j\pi \frac{f_\eta^2}{\kappa_a}}, \quad (\text{B.5})$$

with the only change that the range equation has been substituted by the range of closest approach.

Finally the azimuth compression of the straightened data can be obtained in a similar way as the range compression, but some differences exist since the phase modulation caused by range migration is hyperbolic (although it has been approximated as quadratic) and it is strongly affected by the target dynamics. In addition the amplitude of the echoes returned from the target is affected by the transmitting and receiving antennas patterns.

The azimuthal matched filter is the complex conjugate of the second exponential term in Equation B.5:

$$H_a(f_\eta) \triangleq e^{-j\pi \frac{f_\eta^2}{\kappa_a}}. \quad (\text{B.6})$$

The convolution with the matched filter, as in range, is also performed in frequency domain for computational efficiency, becoming a product in the range-Doppler domain. Taking the expressions B.5 and B.6, the final response for a static target can be expressed as:

$$S_{ac}(\tau, f_\eta) = S_{rcmc}(\tau, f_\eta) \cdot H_a(f_\eta) = A_0 \rho_r \left(\tau - \frac{2R_0}{c} \right) \beta_a(f_\eta - f_{\eta c}) e^{-j \frac{4\pi f_0 R_0}{c}}. \quad (\text{B.7})$$

An inverse azimuthal Fourier transform completes the compression, forming the image in slant range/azimuth dimensions:

$$S_{ac}(\tau, \eta) = \mathcal{F}_\eta^{-1}\{S_{ac}(\tau, f_\eta)\} = A_0 \rho_r \left(\tau - \frac{2R_0}{c} \right) \rho_a(\eta) e^{-j \frac{4\pi f_0 R_0}{c}} e^{j2\pi f_{\eta c} \tau}, \quad (\text{B.8})$$

where $\rho_a(\eta)$ is the amplitude response in the azimuth domain, with the shape of a sinc-like function, similar to $\rho_r(\tau)$. These envelopes shows a target positioned at $\tau = 2R_0/c$ and $\eta = 0$. Notice that η has been defined w.r.t the time of closest approach.

In the final equation appears two exponential terms, the first refers to the range position at R_0 and the second is a linear phase caused by a nonzero Doppler centroid, i.e: the case of squinted antenna.

Figure B.1 shows the representation for a single static blank, also called *Point-spread function* (PSF).

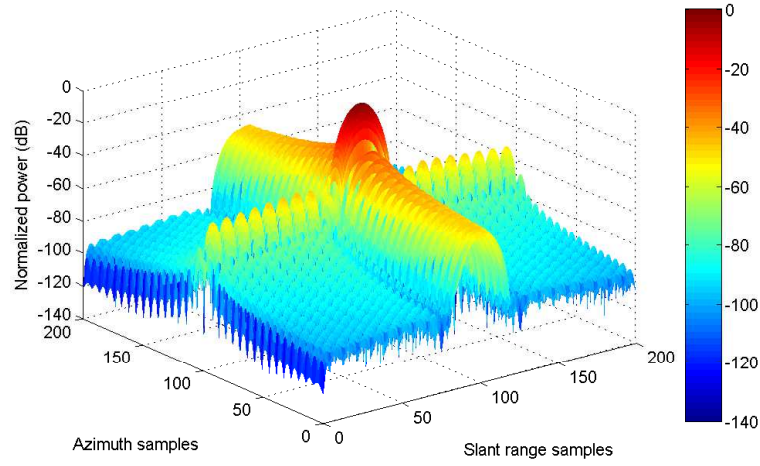


FIGURE B.1: PSF amplitude representation in decibels. Note that azimuth and range sidelobe levels are not the same because different windows have been applied in each dimension.

Appendix C

TSC Sea Clutter Model

This model divides the sea reflectivity in three main factors.

1. Low grazing angle factor:

$$\begin{aligned}\sigma_z &= 0.115S^{1.95}, \\ \sigma_\alpha &= 14.9\varphi(\sigma_z + 0.25)/\lambda, \\ G_a &= \sigma_\alpha^{1.5}/(1 + \sigma_\alpha^{1.5}),\end{aligned}\tag{C.1}$$

Where λ is the radar wavelength (feet), φ is the grazing angle (radians) and S is the sea state in Douglas scale.

2. Wind speed factor:

$$\begin{aligned}V_w &= 6.2S^{0.8}, \\ Q &= \varphi^{0.6}, \\ A_1 &= \left(1 + (\lambda/0.03)^3\right)^{0.1}, \\ A_2 &= \left(1 + (\lambda/0.1)^3\right)^{0.1}, \\ A_3 &= \left(1 + (\lambda/0.3)^3\right)^{Q/3}, \\ A_4 &= 1 + 0.35Q, \\ A &= 2.63A_1/(A_2A_3A_4), \\ G_w &= [(V_w + 4)/15]^A.\end{aligned}\tag{C.2}$$

3. Aspect factor:

$$G_u = \begin{cases} 1, & \text{if } \varphi = \pi/2, \\ \exp \left(0.3 \cos \phi \cdot \exp(-\varphi/0.17) / (\lambda^2 + 0.005)^{0.2} \right), & \text{otherwise} \end{cases} \quad (\text{C.3})$$

Where V_w is the wind velocity (knots) and ϕ is the wind direction angle relative to the radar look direction (radians).

Finally the reflectivity (in m^2/m^2) is obtained by:

1. Horizontal polarization:

$$\sigma_0(H) = 1.7 \cdot 10^{-5} \varphi^{0.5} G_u G_w G_a / (\lambda + 0.05)^{1.8}, \quad (\text{C.4})$$

2. Vertical polarisation

$$10 \log(\sigma_0(V)) = \begin{cases} 10 \log(\sigma_0(H)) - 1.73 \ln(2.507\sigma_z + 0.05) \\ + 3.76 \ln \lambda + 2.46 \ln(\sin \varphi + 0.0001) + 19.8, & \text{if } f < 2GHz \\ 10 \log(\sigma_0(H)) - 1.05 \ln(2.507\sigma_z + 0.05) \\ + 1.09 \ln \lambda + 1.27 \ln(\sin \varphi + 0.0001) + 9.65, & \text{if } f \geq 2GHz \end{cases} \quad (\text{C.5})$$

Appendix D

NRL Sea Clutter Model

The expression proposed by the Naval Research Laboratory for the sea reflectivity is:

$$\begin{aligned} \sigma_{H,V}(dB) = & c_1 + c_2 \cdot \log(\sin \varphi) + \frac{(27.5 + c_3 \cdot \varphi) \cdot \log f}{1 + 0.95 \cdot \varphi} \\ & + c_4 (1 + SS)^{\frac{1}{2+0.085\varphi+0.033SS}} + c_5 \varphi^2, \end{aligned} \quad (D.1)$$

where φ is the grazing angle (radians), f is the radar frequency (GHz) and SS is the sea state in the *World Meteorological Organization* (WMO) universal sea state code, which can be obtained from the wind speed value using the following expressions for the average peak-to-trough height of the 1/3 highest waves:

$$\begin{aligned} h_{1/3} &= 0.04 + 0.1 \cdot SS^{2.1} \\ V_w &= 7.18 \cdot h_{1/3}^{0.4}. \end{aligned} \quad (D.2)$$

The parameters c_1, c_2, \dots, c_5 are constants fixed to minimize the error between the equation and the set of experimental data. Their values are shown in Table D.1.

CONSTANTS	POLARIZATION	
	HORIZONTAL	VERTICAL
c_1	-73.00	-50.79
c_2	20.78	25.93
c_3	7.351	0.7093
c_4	25.65	21.58
c_5	0.00540	0.00211

TABLE D.1: Constants values for the NRL sea clutter model.

Appendix E

Off-line MTI Database Dimensions

The generated off-line database, which provides the P_d as a function of several parameters (Equation 4.21), is a 9-dimensional matrix with the following values for each axis:

$velocity(m/s) :$

$$\begin{aligned} & [0.00, 2.00, 4.00, 6.00, 8.00, 10.0, 12.0, 14.0, 16.0, 18.0, \\ & 20.0, 22.0, 24.0, 26.0, 28.0, 30.0, 32.0, 34.0, 36.0, 38.0, \\ & 40.0, 42.0, 44.0, 46.0, 48.0] \end{aligned} \quad (E.1)$$

$RCS(dB) :$

$$\begin{aligned} & [-10.0, -7.50, -5.00, -2.50, 0.00, 2.50, 5.00, 7.50, 10.0, 12.5, \\ & 15.0, 17.5, 20.0, 22.5, 25.0, 27.5, 30.0] \end{aligned} \quad (E.2)$$

$P_{fa} :$

$$[1.0e-02, 1.0e-03, 1.0e-04, 1.0e-05] \quad (E.3)$$

$\sigma_c^0(dB) :$

$$[-25.0, -23.0, -21.0, -19.0, -17.0, -15.0] \quad (E.4)$$

$\tau_c(s) :$

$$\begin{aligned} & [1.0000, 0.1000, 0.0300, 0.0100, 0.0060, 0.0030, \\ & 0.0010, 0.0006, 0.0003] \end{aligned} \quad (E.5)$$

$NE\beta_0(dB) :$

$$[-25.0, -23.0, -21.0, -19.0, -17.0, -15.0] \quad (E.6)$$

$$N_{looks} : \quad (E.7)$$

$$[1, \ 5, \ 10]$$

$$N_{looks_target_present} : \quad (E.8)$$

$$[1, \ 1, \ 1]$$

$$[1, \ 3, \ 5]$$

$$[1, \ 5, \ 10]$$

Where the row index on $N_{looks_target_present}$ depends on the N_{looks} index value.

$$\rho_t : \quad (E.9)$$

$$[1]$$

In this case the decorrelation of the target is not considered.

References

- [1] C. Elachi, *Spaceborne Radar Remote Sensing: Applications and Techniques*. IEEE Press, 1987.
- [2] J. C. Curlander and R. N. McDonough, *Synthetic Aperture Radar: Systems and Signal Processing*. Wiley, 1991.
- [3] I. G. Cummings and F. H. Wong, *Digital Processing of Synthetic Aperture Radar Data: Algorithms and Implementation*. Artech House, 2005.
- [4] A. Cardama Aznar, L. Jofre Roca, J. M. Rius Casals, J. Romeu Robert, S. Blanch Boris, and M. Ferrando Bataller, *Antenas*. Edicions UPC, 1998.
- [5] P. López-Dekker, “Introduction to SAR II: Acquisition modes, Applications and future trends.” Radar Remote Sensing Course, September 2010.
- [6] M. Eineder, T. Fritz, J. Mittermayer, A. Roth, E. Boerner, and H. Breit, “TerraSAR-X Ground Segment, Basic Product Specification Document,” tech. rep., DTIC Document, 2008.
- [7] W. Carrara, R. Goodman, and R. Majewski, *Spotlight Synthetic Aperture Radar: Signal Processing Algorithms*. Artech House signal processing library, Artech House, Incorporated, 1995.
- [8] J. T. González Partida, “SAR Aerotransportado. Desarrollo de algoritmos de corrección de movimiento en tiempo real,” Master’s thesis, Universidad Politécnica de Madrid, 2004.
- [9] R. K. Raney, “Synthetic aperture imaging radar and moving targets,” *Aerospace and Electronic Systems, IEEE Transactions on*, vol. AES-7, no. 3, pp. 499–505, 1971.
- [10] K. Tomiyasu, “Tutorial review of synthetic-aperture radar (SAR) with applications to imaging of the ocean surface,” *Proceedings of the IEEE*, vol. 66, no. 5, pp. 563–583, 1978.

- [11] J. J. Sharma, C. H. Gierull, and M. J. Collins, "Compensating the effects of target acceleration in dual-channel SAR-GMTI," *IEE Proceedings-Radar, Sonar and Navigation*, vol. 153, no. 1, pp. 53–62, 2006.
- [12] S. V. Baumgartner and G. Krieger, "Fast GMTI algorithm for traffic monitoring based on a priori knowledge," *Geoscience and Remote Sensing, IEEE Transactions on*, vol. 50, no. 11, pp. 4626–4641, 2012.
- [13] C. E. Livingstone and A. A. Thompson, "The moving object detection experiment on RADARSAT-2," *Canadian journal of remote sensing*, vol. 30, no. 3, pp. 355–368, 2004.
- [14] W. Alpers, "Ocean surface wave imaging from Seasat to Envisat," in *International Geoscience and Remote Sensing Symposium*, vol. 1, pp. I–35, 2003.
- [15] M. P. Clarizia, C. Gommenginger, M. Di Bisceglie, C. Galdi, and M. A. Srokosz, "Simulation of L-band bistatic returns from the ocean surface: a facet approach with application to ocean GNSS reflectometry," *Geoscience and Remote Sensing, IEEE Transactions on*, vol. 50, no. 3, pp. 960–971, 2012.
- [16] G. Marull-Paretas, "Development of a multi-channel sar simulator for open-oceans: OASIS," master thesis, UPC, 2013.
- [17] B. Kinsman, *Wind Waves: Their Generation and Propagation on the Ocean Surface*. Dover Publications, 2002.
- [18] V. Kudryavtsev, D. Hauser, G. Caudal, and B. Chapron, "A semiempirical model of the normalized radar cross-section of the sea surface 1. Background model," *Journal of Geophysical Research: Oceans (1978–2012)*, vol. 108, no. C3, pp. FET–2, 2003.
- [19] H. Sittrop, "Sea-clutter dependency on windspeed," *In its On Microwave Meas., Transmission and Reception 4 p (SEE N80-26551 17-31)*, vol. 1, 1978.
- [20] M. Horst, F. Dyer, and M. Tuley, "Radar sea clutter model," in *Antennas and Propagation*, vol. 1, pp. 6–10, 1978.
- [21] "Section 5.6.1. backscatter from sea," radar workstation, Technology Service Corporation, 2, 1990. 177–186.
- [22] F. E. Nathanson, J. P. Reilly, and M. N. Cohen, *Radar design principles-Signal processing and the Environment*. SciTech Publishing, 2nd ed. ed., 1991.
- [23] J. Reilly and G. Dockery, "Influence of evaporation ducts on radar sea return," in *IEE Proceedings F (Radar and Signal Processing)*, vol. 137(2), pp. 80–88, 1990.

- [24] V. Gregers-Hansen and R. Mital, "An improved empirical model for radar sea clutter reflectivity," *Aerospace and Electronic Systems, IEEE Transactions on*, vol. 48, no. 4, pp. 3512–3524, 2012.
- [25] I. Antipov, "Simulation of sea clutter returns," tech. rep., DSTO Electronic and Surveillance Research Laboratory, 1998.
- [26] D. J. Crisp, R. Kyprianou, L. Rosenberg, and N. J. Stacy, "Modelling X-band sea clutter at moderate grazing angles.," in *Radar, 2008 International Conference on*, pp. 569–574, IEEE, 2008.
- [27] K. D. Ward, S. Watts, and R. J. Tough, *Sea clutter: scattering, the K distribution and radar performance*, vol. 20. IET, 2006.
- [28] I. Antipov, "Analysis of sea clutter data," tech. rep., DSTO Electronic and Surveillance Research Laboratory, 1998.
- [29] I. R. Joughin, D. B. Percival, and D. P. Winebrenner, "Maximum likelihood estimation of K distribution parameters for SAR data," *Geoscience and Remote Sensing, IEEE Transactions on*, vol. 31, no. 5, pp. 989–999, 1993.
- [30] D. R. Iskander and A. M. Zoubir, "Estimating the parameters of K-distribution using higher-order and fractional moments," *IEEE Transactions on Aerospace and electronic systems*, vol. 35, no. 4, pp. 1453–1457, 1999.
- [31] D. J. Crisp, L. Rosenberg, N. J. Stacy, and Y. Dong, "Modelling X-band sea clutter with the k-distribution: Shape parameter variation," in *Radar Conference-Surveillance for a Safer World, 2009. RADAR. International*, pp. 1–6, IEEE, 2009.
- [32] F. Lombardini, F. Bordon, and F. Gini, "Feasibility study of along-track sar interferometry with the cosmo-skymed satellite system," in *Geoscience and Remote Sensing Symposium, 2004. IGARSS'04. Proceedings. 2004 IEEE International*, vol. 5, pp. 3337–3340, IEEE, 2004.
- [33] S. J. Frasier and A. J. Camps, "Dual-beam interferometry for ocean surface current vector mapping," *Geoscience and Remote Sensing, IEEE Transactions on*, vol. 39, no. 2, pp. 401–414, 2001.
- [34] G. H. Golub and C. F. Van Loan, *Matrix computations*, vol. 3. JHU Press, 2012.
- [35] W. J. Pierson and L. Moskowitz, "A proposed spectral form for fully developed wind seas based on the similarity theory of S.A. Kitaigorodskii," *Journal of geophysical research*, vol. 69, no. 24, pp. 5181–5190, 1964.

- [36] T. Elfouhaily, B. Chapron, K. Katsaros, and D. Vandemark, "A unified directional spectrum for long and short wind-driven waves," *Journal of Geophysical Research: Oceans (1978–2012)*, vol. 102, no. C7, pp. 15781–15796, 1997.
- [37] W. H. Michel, "Sea spectra simplified," *Marine Technology*, vol. 5, no. 1, pp. 17–30, 1968.
- [38] K. Torsethaugen, S. Haver, *et al.*, "Simplified double peak spectral model for ocean waves," in *Proceedings of ISOPE conference*, vol. 3, pp. 76–84, 2004.
- [39] K. Hasselmann, T. Barnett, E. Bouws, H. Carlson, D. Cartwright, K. Enke, J. Ewing, H. Gienapp, D. Hasselmann, P. Kruseman, *et al.*, "Measurements of wind-wave growth and swell decay during the Joint North Sea Wave Project (JONSWAP)," 1973.
- [40] M. S. Longuet-Higgins, D. Cartwright, and N. Smith, "Observations of the directional spectrum of sea waves using the motions of a floating buoy," 1963.
- [41] H. Mitsuyasu, F. Tasai, T. Suhara, S. Mizuno, M. Ohkusu, T. Honda, and K. Rikishi, "Observations of the directional spectrum of ocean waves using a cloverleaf buoy," *Journal of Physical Oceanography*, vol. 5, no. 4, pp. 750–760, 1975.
- [42] D. Hasselmann, M. Dunkel, and J. Ewing, "Directional wave spectra observed during JONSWAP 1973," *Journal of physical oceanography*, vol. 10, no. 8, pp. 1264–1280, 1980.
- [43] L. Holthuijsen, "Observations of the directional distribution of ocean-wave energy in fetch-limited conditions," *Journal of Physical Oceanography*, vol. 13, no. 2, pp. 191–207, 1983.
- [44] M. A. Donelan, J. Hamilton, and W. Hui, "Directional spectra of wind-generated waves," *Philosophical Transactions of the Royal Society of London. Series A, Mathematical and Physical Sciences*, vol. 315, no. 1534, pp. 509–562, 1985.
- [45] K. Hasselmann and S. Hasselmann, "On the nonlinear mapping of an ocean wave spectrum into a synthetic aperture radar image spectrum and its inversion," *Journal of Geophysical Research: Oceans (1978–2012)*, vol. 96, no. C6, pp. 10713–10729, 1991.
- [46] J. Mittermayer and H. Runge, "Conceptual studies for exploiting the terraSAR-X dual receive antenna," in *INTERNATIONAL GEOSCIENCE AND REMOTE SENSING SYMPOSIUM*, vol. 3, pp. III–2140, 2003.

- [47] E. Makhoul, A. Broquetas, J. Ruiz, Y. Zhan, and F. Ceba, "A performance evaluation of SAR-GMTI missions for maritime applications," *Geoscience and Remote Sensing, IEEE Transaction, to be published*, 2014.
- [48] C. E. Muehe and M. Labitt, "Displaced-phase-center antenna technique," *Lincoln Laboratory Journal*, vol. 12, no. 2, pp. 281–296, 2000.
- [49] S. Chiu and C. Livingstone, "A comparison of displaced phase centre antenna and along-track interferometry techniques for RADARSAT-2 ground moving target indication," *Canadian Journal of Remote Sensing*, vol. 31, no. 1, pp. 37–51, 2005.
- [50] J. R. Guerri, *Space-time adaptive processing for radar*. Artech House, 2003.
- [51] C. M. Teixeira, "Performance analysis of post-doppler STAP," in *Signals, Systems and Computers, 2008 42nd Asilomar Conference on*, pp. 551–555, IEEE, 2008.
- [52] S. V. Baumgartner and G. Krieger, "A priori knowledge-based Post-Doppler STAP for traffic monitoring applications," in *Geoscience and Remote Sensing Symposium (IGARSS), 2012 IEEE International*, pp. 6087–6090, IEEE, 2012.
- [53] D. Cerutti-Maori, I. Sikaneta, and C. H. Gierull, "Optimum SAR/GMTI processing and its application to the radar satellite RADARSAT-2 for traffic monitoring," *Geoscience and Remote Sensing, IEEE Transactions on*, vol. 50, no. 10, pp. 3868–3881, 2012.
- [54] D. Cerutti-Maori and I. Sikaneta, "Optimum GMTI processing for Space-based SAR/GMTI Systems-Theoretical Derivation," in *Synthetic Aperture Radar (EU-SAR), 2010 8th European Conference on*, pp. 1–4, VDE, 2010.
- [55] W. Bürger, "Space-Time Adaptive Processing: Algorithms," tech. rep., DTIC Document, 2006.
- [56] W. L. Melvin, "A STAP overview," *Aerospace and Electronic Systems Magazine, IEEE*, vol. 19, no. 1, pp. 19–35, 2004.
- [57] S. Barbarossa, A. Beaton, A. Broquetas, F. Ceba, P. Di Lorenzo, F. Letterio, M. Maffei, E. Makhoul, P. Nini, S. Tonetti, and P. Vecchiarelli, "SIMTISYS D42.1 final report," tech. rep., Thales Alenia Space Italia, 2013.
- [58] S. Blake, "OS-CFAR theory for multiple targets and nonuniform clutter," *Aerospace and Electronic Systems, IEEE Transactions on*, vol. 24, no. 6, pp. 785–790, 1988.
- [59] N. Levanon, *Radar principles*. A Wiley Interscience publication, Wiley, 1988.

- [60] C. H. Gierull, "Statistical analysis of multilook SAR interferograms for CFAR detection of ground moving targets," *Geoscience and Remote Sensing, IEEE Transactions on*, vol. 42, no. 4, pp. 691–701, 2004.
- [61] C. H. Gierull and I. C. Sikaneta, "Estimating the effective number of looks in interferometric sar data," *Geoscience and Remote Sensing, IEEE Transactions on*, vol. 40, no. 8, pp. 1733–1742, 2002.
- [62] P. Nini, F. Letterio, S. Tonetti, R. Alacevich, A. Beaton, E. Makhoul, A. Broquetas, S. Barbarossa, P. Vecchiarelli, P. Di Lorenzo, M. Maffei, and F. Ceba, "SIMTISYS D31.2 modules interface design," tech. rep., Thales Alenia Space Italia, 2013.
- [63] S. Gantert, A. Kern, R. During, J. Janoth, L. Petersen, and J. Herrmann, "The future of X-band SAR: TerraSAR-X next generation and WorldSAR constellation," in *Synthetic Aperture Radar (AP SAR), 2013 Asia-Pacific Conference on*, pp. 20–23, IEEE, 2013.
- [64] D. Cristallini, D. Pastina, F. Colone, and P. Lombardo, "Efficient detection and imaging of moving targets in sar images based on chirp scaling," *Geoscience and Remote Sensing, IEEE Transactions on*, vol. 51, no. 4, pp. 2403–2416, 2013.
- [65] R. Khairi, A. Coatanhay, and A. Khenchaf, "Modeling of electromagnetic waves scattering from sea surface using Higher-Order Moment Method (ho-mom) and NURBS patch," in *Electromagnetics in Advanced Applications (ICEAA), 2011 International Conference on*, pp. 694–697, IEEE, 2011.
- [66] M. B. Kanevsky, *Radar imaging of the ocean waves*. Elsevier, 2008.
- [67] P. L. Choong, "Modelling airborne L-band radar sea and coastal land clutter," tech. rep., DTIC Document, 2000.
- [68] B. Spaulding, D. Horton, and H. Pham, "Wind aspect factor in sea clutter modeling," in *Radar Conference, 2005 IEEE International*, pp. 89–92, IEEE, 2005.
- [69] C. R. Jackson, J. R. Apel, *et al.*, *Synthetic aperture radar marine user's manual*. US Department of Commerce, 2004.
- [70] F. T. Ulaby, R. K. Moore, A. K. Fung, and A. House, *Microwave remote sensing: active and passive*, vol. 2. Addison-Wesley Reading, Massachusetts, 1981.
- [71] R. Raghavan, "A method for estimating parameters of K-distributed clutter," *Aerospace and Electronic Systems, IEEE Transactions on*, vol. 27, no. 2, pp. 238–246, 1991.

- [72] A. R. DiDonato and A. H. Morris Jr, "Computation of the incomplete gamma function ratios and their inverse," *ACM Transactions on Mathematical Software (TOMS)*, vol. 12, no. 4, pp. 377–393, 1986.
- [73] M. Ikeda, *Oceanographic applications of remote sensing*. CRC press, 1995.
- [74] W. H. Michel, "Sea spectra revisited," *MAR TECHNOL*, vol. 36, no. 4, pp. 211–227, 1999.
- [75] S. Barbarossa and A. Scaglione, "Autofocusing of SAR images based on the product high-order ambiguity function," in *Radar, Sonar and Navigation, IEE Proceedings-*, vol. 145, pp. 269–273, IET, 1998.
- [76] S. Barbarossa, "Detection and imaging of moving objects with synthetic aperture radar. Part 1: Optimal detection and parameter estimation theory," in *Radar and Signal Processing, IEE Proceedings F*, vol. 139, pp. 79–88, IET, 1992.
- [77] S. Barbarossa and A. Farina, "Detection and imaging of moving objects with synthetic aperture radar. part 2: Joint time-frequency analysis by Wigner-Ville distribution," in *IEE Proceedings F (Radar and Signal Processing)*, vol. 139, pp. 89–97, IET, 1992.
- [78] S. Barbarossa, A. Scaglione, and G. B. Giannakis, "Product high-order ambiguity function for multicomponent polynomial-phase signal modeling," *Signal Processing, IEEE Transactions on*, vol. 46, no. 3, pp. 691–708, 1998.
- [79] S. Barbarossa, P. Di Lorenzo, P. Vecchiarelli, A. Silvi, and A. Bruner, "Parameter estimation of 2D Polynomial Phase Signals: An application to moving target imaging with SAR," in *Acoustics, Speech and Signal Processing (ICASSP), 2013 IEEE International Conference on*, pp. 4554–4558, IEEE, 2013.
- [80] D. Cerutti-Maori and I. Sikaneta, "A generalization of DPCA processing for multi-channel SAR/GMTI radars," *Geoscience and Remote Sensing, IEEE Transactions on*, vol. 51, no. 1, pp. 560–572, 2013.
- [81] C. H. Gierull, I. Sikaneta, and D. Cerutti-Maori, "Two-step detector for RADARSAT-2's experimental GMTI mode," *Geoscience and Remote Sensing, IEEE Transactions on*, vol. 51, no. 1, pp. 436–454, 2013.
- [82] D. Zhen, C. Bin, and L. Diannong, "Detection of ground moving targets for two-channel spaceborne SAR-ATI," *EURASIP Journal on Advances in Signal Processing*, vol. 2010, 2010.

-
- [83] S. Chiu, “A constant false alarm rate (CFAR) detector for RADARSAT-2 along-track interferometry,” *Canadian Journal of Remote Sensing*, vol. 31, no. 1, pp. 73–84, 2005.
- [84] E. Makhoul, Y. Zhan, F. Ceba, A. Broquetas, A. Beaton, F. Letterio, S. Tonetti, S. Barbarossa, P. Di Lorenzo⁴, and M. Maffei, “Fast Simulation Performance Evaluation of Spaceborne SAR-GMTI Missions for Maritime Applications,” in *2014 10th European Conference on Synthetic Aperture Radar (EUSAR)*, to be published, 2014.